Universidade de Aveiro Departamento de Electrónica, Telecomunicações e Informática,
2017

Daniel Filipe Simões Malafaia

Deteção espetral de banda larga para rádio cógnitivo

Wideband spectrum sensing for cognitive radio

"The world society as a whole needs and will benefit from increasing communication capability. And to achieve that capability, careful planning, cooperation, and spectrum sharing on the part of all will be needed. "

— William F. Utlaut, 1978

Universidade de Aveiro Departamento de
Electrónica, Telecomunicações e Informática,
2017

Daniel Filipe
Simões Malafaia

Wideband spectrum sensing for cognitive radio

Deteção espetral de banda larga para rádio cógnitivo

Tese apresentada às Universidade do Minho, Aveiro e Porto para cumprimento dos requesitos necessários à obtenção do grau de Doutor em Telecomunicações no âmbito do programa MAP-Tele, realizada sob a orientação científica do Doutor José Manuel Neto Vieira e Doutora Ana Maria Tomé, Professores do Departamento de Eletrónica, Telecomunicações e Informática da Universidade de Aveiro.

o júri / the jury

presidente / president	**Doutor Aníbal Guimarães da Costa** Professor Catedrático da Universidade de Aveiro
vogais / examiners committee	**Doutor Nuno Miguel Gonçalves Borges de Carvalho** Professor Catedrático da Universidade de Aveiro
	Doutor Rui Miguel Henriques Dias Morgado Dinis Professor Auxiliar com Agregação da Universidade Nova de Lisboa
	Doutor Aníbal João de Sousa Ferreira Professor Associado da Universidade do Porto
	Doutor Vítor Manuel Mendes Silva Professor Auxiliar da Universidade de Coimbra
	Doutor José Manuel Neto Vieira Professor Auxiliar da Universidade de Aveiro

agradecimentos / acknowledgements

O autor deseja antes de mais agradecer aos colegas do Instituto de Telecomunicações. Todos eles excelentes profissionais e além disso amigos que me acompanharam, ajudaram e apoiaram durante a duração deste trabalho, são eles: André Prata, Daniel Belo, Daniel Dinis, Diogo Ribeiro, Filipe Barradas, Jorge Santos, João Gonçalves, João Santos, Luís Cótimos, Marina Jordão, Ricardo Correia, Ricardo Fernandes, Ricardo Gonçalves, Rui Fiel e Tiago Varum. Aos professores Nuno Borges, Arnaldo Oliveira e Nuno Matos por facultarem recursos essenciais para a conclusão deste trabalho. Ao Hugo Mostardinha pelo apoio prestado no laboratório de RF. Aos orientadores, professores José Vieira e Ana Tomé pela partilha de conhecimento e revisão do trabalho. A minha mais sincera gratidão à minha família por ter sempre acreditado em mim, os meus pais, irmão, primos, tias, tio e avós que me criaram e fizeram de mim quem sou hoje. A todos os outros que não couberam neste agradecimento, mas que de alguma forma ajudaram o desenrolar deste trabalho, o meu obrigado.

Palavras-chave Rádio Cognitivo, Deteção Espetral, Partilha de Espetro, Deteção de Sinal, 5G

Resumo

Esta tese tem como objetivo o desenvolvimento de uma unidade autónoma de deteção espetral em tempo real. Para tal são analisadas várias implementações para a estimação do nível de ruído de fundo de forma a se poder criar um limiar adaptativo para um detetor com uma taxa constante de falso alarme. Além da identificação binária da utilização do espetro, pretende-se também obter a classificação individual de cada transmissor e a sua ocupação ao longo do tempo. Para tal são exploradas duas soluções baseadas no algoritmo, de agrupamento de dados, conhecido como maximização de expectativas que permite identificar os sinais analisados pela potência recebida e relação de fase entre dois recetores. Um algoritmo de deteção de sinal baseado também na relação de fase de dois recetores e sem necessidade de estimação do ruído de fundo é também demonstrado. Este algoritmo foi otimizado para permitir uma implementação eficiente num arranjo de portas programáveis em campo a funcionar em tempo real para uma elevada largura de banda, permitindo também estimar a direção da transmissão detetada.

Keywords Cognitive Radio, Spectrum Sensing, Spectrum Sharing, Signal detection, 5G

Abstract

The purpose of this thesis is to develop an autonomous unit for real time spectrum sensing. For this purpose, several implementations for the estimation of the background noise level are analysed to create an adaptive threshold and ensure a constant false alarm rate detector. In addition to the binary identification of the spectrum usage, it is also intended to obtain an individual classification of each transmitter occupation and its spectrum usage over time. To do so, two solutions based on the expectation maximization data clustering, that allow to identify the analyzed signals by the received power and phase relation between two receivers, were explored. A signal detection algorithm, also based on the phase relationship between two receivers and with no need for noise estimation is also demonstrated. This algorithm has been optimized to allow an efficient implementation in a FPGA operating in real time for a high bandwidth and it also allows the estimation of the direction of arrival of the detected transmission.

Contents

List of Figures

List of Tables

List of Acronyms

2D	Two Dimensional
3GPP	Third Generation Partnership Project
ADC	Analog-to-Digital Converter
AUC	Area Under the Curve
BPSK	Binary Phase-Shift Keying
CORDIC	COordinate Rotation DIgital Computer
CSAT	Carrier-Sensing Adaptive Transmission
CR	Cognitive Radio
CFAR	Constant False Alarm Rate
CW	Continuous Wave
CDF	Cumulative Distribution Functions
DIFS	DCF Interframe Space
D2D	Device To Device
DSP	Digital Signal Processing
DAC	Digital-to-Analog Converter
DMA	Direct Memory Access
DOA	Direction of Arrival
DFT	Discrete Fourier Transform
DPSS	Discrete Prolate Spheroidal Sequences
DCF	Distributed Coordination Function
DSA	Dynamic Spectrum Access
DDR	Double Data Rate
ED	Energy Detection
EM	Expectation Maximization
FLOP	FLoating-point OPerations
FPGA	Field-Programmable Gate Array
FIR	Finite Impulse Response
FFT	Fast Fourier Transform
FDD	Frequency Division Duplex
GMM	Gaussian Mixture Model
I/Q	In-phase and Quadrature
IID	Independent and Identically Distributed
IP	Internet Protocol
LTE-U	LTE in unlicensed spectrum
LSA	Licensed Shared Access
LBT	Listen-Before-Talk

LTE	Long-Term Evolution
LUT	Look Up Table
LNA	Low Noise Amplifier
MSE	Mean Squared Error
MIMO	Multiple-Input and Multiple-Output
OFDM	Orthogonal Frequency-Division Multiplexing
PISO	Parallel Input Serial Output
PUCCH	Physical Uplink Control Channel
PUSCH	Physical Uplink Shared Channel
PSD	Power Spectrum Density
PDF	Probability Distribution Function
QAM	Quadrature Amplitude Modulation
QPSK	Quadrature Phase Shift Keying
RF	Radio Frequency
RFIC	Radio Frequency Integrated Circuit
ROC	Receiver Operating Characteristic
RB	Resource Blocks
SIPO	Serial Input Parallel Output
SIFS	Short Inter Frame Space
STFT	Short Time Fourier Transform
SNR	Signal-to-Noise-Ratio
SC-FDMA	Single-Carrier Frequency Division Multiple Access
SDR	Software Defined Radio
SMA	SubMiniature version A
TCP	Transmission Control Protocol
USRP	Universal Software Radio Peripheral
UE	User Equipment
VNI	Visual Network Index
WNS	Worst Negative Slack

Chapter 1

Introduction

1.1 Motivation

The expected explosion of the number of wireless devices for the years to come, will increase the demand for radio frequency spectrum to allocate new services. The current spectrum policy is based on a fixed channel allocation where a slice of the spectrum is assigned to one or more dedicated users. The proliferation of wireless services in the last decades that use a fixed spectrum access created an artificial spectrum scarcity problem, where certain spectrum bands are heavily used but the majority of the spectrum is sporadically occupied by the licensees. Recent studies on spectrum utilization measurements, reveal that a large portion of the licensed spectrum constantly experiences low utilization from the licensed users [1, 2]. The policy of allocating fixed channels prevents then the utilization of rarely used licensed spectrum channels by users other than the owners. The alternative is to use the available Radio-Frequency (RF) spectrum more wisely. The cognitive radio concept, based on Software Defined Radio (SDR) platform, was proposed to solve this problem and is based on an adequate capability of the radios to sense the spectrum usage by other transmitters. The knowledge of which frequency band is vacant at a specific time can then be used for opportunistic data transmission [3]. This method of spectrum usage allows for a higher spectral efficiency in comparison with fixed channel allocation [4].

1.1.1 Software Defined Radio

The SDR was first introduced by Joseph Mitola as a concept of the future of the radio [5]. It is a generic radio platform with the capability to operate at different bandwidths over numerous frequencies, as well as being flexible in using different modulation schemes and waveform formats. Therefore, the SDR has a very flexible analog front-end that, in combination with adjustable digital signal processing techniques, is flexible enough to modulate and demodulate any signal entirely in software regardless of the standard or its characteristics.

The transmitter has the ability to generate any baseband waveform and up-convert it to any central frequency. This signal is converted to analog domain with a Digital-to-Analog Converter (DAC) and is then amplified and transmitted. On the other hand, the receiver collects a certain bandwidth of the spectrum, amplifies it and converts it back to the digital domain using an Analog-to-Digital Converter (ADC). After that conversion, the process of detection and demodulation of the signal is carried out by software. The ideal SDR will then implement all the typical radio communication system components in software, leaving as less as possible to the hardware side as seen in Figure 1.1.

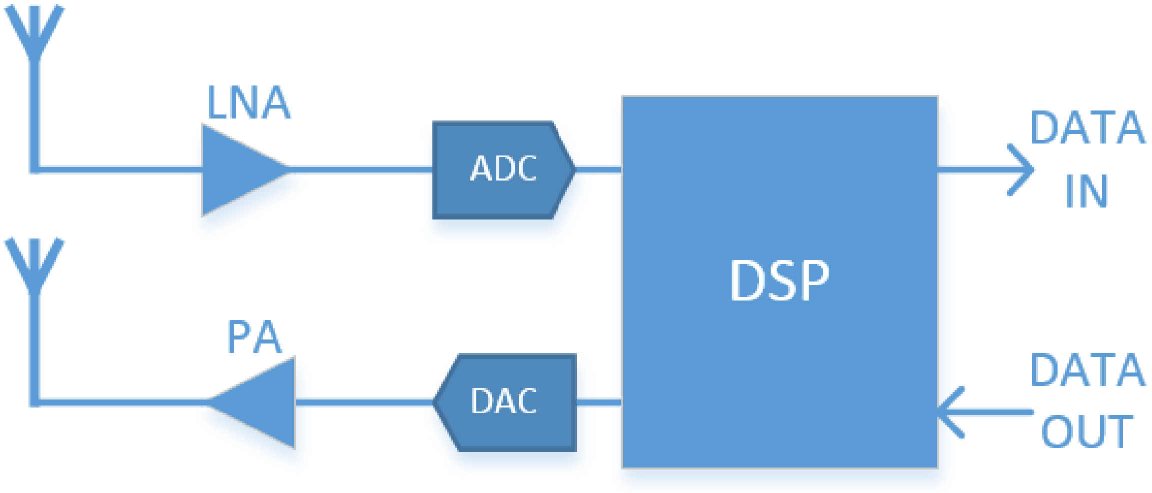

Figure 1.1: Functional diagram of an ideal SDR.

There has been a large and fast development in the area of SDR, portable and flexible hardware platforms are now commercially accessible and full–fledged [6][7]. This massive spread of the technology allows the development of new applications based on this architecture [8, 9]. For instance, the SDR architecture allowed the implementation of software defined radar [8] and Dynamic Spectrum Access (DSA) [9] platforms.

1.1.2 Cognitive Radio

Traditional wireless networks are based on the exclusive allocation of the spectrum, where telecommunication service providers buy in auction reserved frequency bands in order to ensure quality of service. For personal local wireless networks is normally used a license-free spectrum, called the ISM bands, where part of the radio spectrum is used for personal, industrial, scientific and medical utilization. As these bands are becoming crowded with unlicensed equipment, as for example Wi-Fi devices, the need for a new paradigm and radio implementation for this unlicensed spectrum is becoming increasingly important. The expected solution is the Cognitive Radio (CR) [10].

Cognitive radio, built on a software radio platform, is a context-aware intelligent radio that is able to autonomously reconfigure itself by learning from and adapting to the communication environment. One of the key features of SDR architecture is its flexibility to use a variety of frequency bands according to their availability. This flexibility could allow for cognitive radios to share parts of the spectrum while avoiding collision with any licensed user or other CRs. The spectrum sharing paradigm is currently being pushed by two leading challenges, the European Union Collaborative spectrum sharing [11] and the American Darpa's Spectrum Collaboration Challenge [12].

This flexible sharing of the spectrum, was initially discussed in the first IEEE DySPAN and named DSA [13]. The DSA, also commonly called spectrum sharing [14], is usually categorized in three models:

- **Dynamic Exclusive Use Model** : Is an exclusive shared use, where any user can dynamically license, for a given time and location, a number of available frequency bands. Also called Licensed Shared Access (LSA) [15] it allows a most effective use of spectrum resources by permitting temporary allocations of the shared spectrum according to the users needs. This exclusive shared model is faraway from completely eliminate quiet periods in spectrum, due to the bursty nature of wireless traffic, but it ensures a predictable quality of service for the reserved time.
- **Open Sharing Model**: Is a completely shared use, giving total freedom to the users to manage the sharing of specific slices of the spectrum without intervention of a central regulator entity [16]. This creates the need for the users to constantly sense the allowed spectrum bands and cooperate with the other cognitive radios in order to detect and use spectrum bands that are not currently being occupied. It is supported by the concept of a periodic Listen-Before-Talk (LBT) and limited channel occupancy time.
- **Hierarchical Access Model**: A model that adopts an access structure where licensed spectrum can be open to secondary users while limiting the interference perceived by primary users, the licensees [17]. The model allows opportunistically access to the licensed spectrum by allowing the secondary users to identify and exploit local and instantaneous spectrum availability in a non-intrusive manner.

The employment of these methods would be expected to alleviate the current spectrum usage, while still providing the exclusive spectrum allocation for the primary users. Some specific implementations have already been have been integrated into the IEEE 802.22 [18] standard for wireless regional networks and IEEE 802.11af [19] for wireless local networks. Both standards define a hierarchical access model to use licensed frequencies but limit the interference with the primary users such as analog TV, digital TV and low power licensed devices such as wireless microphones [20].

However, the practical implementation of such architecture is surrounded by several challenges both in software and hardware. In software, new and robust communication protocols for RF devices are needed in order to facilitate the use of the shared spectrum. In the hardware, there is the necessity to sense the entire viable shared spectrum, that can be very spread and detect which bands are being already used. If the band is not being currently used, the CR should be very flexible and able to change the frequency of the transmission to allocate it into the available band. It should also detect if any user, that has the right to a frequency band, will start transmitting and in the fastest possible way stop the usage of that section of the spectrum.

These specificities of a Dynamic Spectrum Access create the need for a spectrum sensing unit that can quickly and accurately identify white spaces trough a wideband of frequencies. As an example, the current unlicensed frequency bands for RF are incredibly spaced apart in frequency. The bands in the order of GHz are in 2.4GHz, 5.8GHz and 24GHz [21]. Taking advantage of all these spectrum resources would require an exceedingly wideband cognitive radio front-end.

1.1.3 Upcoming implementations based on spectrum sensing

1.1.3.1 LTE-U

The Long-Term Evolution (LTE) is the current standard for high-speed wireless communication systems and has reached its maturity. The new releases only consider incremental improvements to the standard without any new inclusions of licensed spectrum [22]. In a recent Visual Network Index (VNI) report [23] it is foreseen that an incremental approach will not be able to meet the future demands of the mobile data traffic by 2019, where is expected a 57% increase compared to the 2014 traffic.

The growing number of mobile data subscribers, forced the Third Generation Partnership Project (3GPP) partnership to find a solution before 5G deployment by 2020 [24] . Therefore, as part of 3GPP Release 13, a new feature was introduced that allowed the use of unlicensed spectrum by LTE alongside with the licensed channels, called LTE in unlicensed spectrum (LTE-U). The chosen frequency bands for deployment are in the 5 GHz spectrum region, that offers large amounts of unlicensed bandwidth that is available globally. For instance, in Europe there is 455 MHz of spectrum available in 5.15-5.35GHz and 5.47-5.725GHz [25]. The use of unlicensed spectrum usually carries some regulatory requirements, such as being able to detect if a radar system is using the band and also being able to co-exist with other users of the band, most importantly Wi-Fi. This is also referred as LBT and means that it is not always possible to transmit immediately if the intended channel is occupied. It was also proposed that a LTE-U unit could sense the spectrum while it transmits enabling a sensing while transmitting approach [26].

LTE-U small cells are able to sense the 5GHz frequency bands and identify the least used channels for supplemental downlinks. These measurements are performed periodically, allowing for a dynamic frequency selection according to the local spectrum usage. LTE in unlicensed spectrum also uses a Carrier-Sensing Adaptive Transmission (CSAT) mechanism that is in-line with the concept of coexistence based on medium sensing. In CSAT, the small cell senses the medium for a duration (between 10ms to 200ms) and according to the observed medium activities, the algorithm gates off the LTE transmission proportionally [27]. In particular, the small cell defines a time cycle where it transmits in a fraction of the cycle and gates off in the remaining duration.

1.1.3.2 5G

With a limited amount of available spectrum and the necessity of increasingly higher datarates, the research in 5G mobile communication systems has shown an important focus in spectrum sharing both for primary users [14] and for Device To Device (D2D) communication [16]. This approach allows the dynamic assignment of spectrum to an RF device in an opportunistic way, even for frequency bands assigned to primary users provided that it is possible to prevent collisions from secondary users. However, this strategy presents a huge challenge to spectrum regulators in order to control interference.

The future spectrum sharing implementations can be done on licensed spectrum [28], where the opportunist users should be capable of accessing a geolocation database and/or sense any incumbent signals, being constantly alert to avoid conflict with primary users that have priority access in that frequency band [29]. It can also accommodate unlicensed spectrum where the users need to sense the occupation of these bands in order to allocate their communication on channels without interfering with other transmitting devices, sharing the same vision used in LTE-U.

D2D networks will allow users to not only use the spectrum resources provided by a base station but also use the available unoccupied spectrum, discovered by distributed spectrum sensing units, for direct communication between devices [30]. This will enable low-power, high-data rate and low-latency communication services between end-users in future 5G networks [31]. A similar strategy is followed in ad-hoc networks as for example in Wi-Fi direct [32].

1.1.3.3 Cognitive Bio-Radar

Non-contact methods for measuring bio-signals, in particular cardiac and respiratory signals are a very active field of research. Wireless measuring of human physiological parameters, like heart rate variability and breathing pattern are of great interest in the medical field for monitoring hospitalized patients, home health care, rehabilitation and nursing of elderly. Also there are other commercially oriented applications, such as automotive industry for driver monitoring or for applications in psychology as for example measurement of stress response [33]. One of the most promising techniques for wireless measurement of bio-signals is commonly called bio-radar and is based on a Doppler effect radar. In particular, Continuous-Wave (CW) Doppler radar that is currently used in research [34][35].

In [36] the author proposed a new architecture called cognitive bio-radar where the radar device is implemented on a SDR. This allows the development of a flexible bio-radar that is also able to do spectrum sensing, have an opportunistic spectrum allocation, an adaptive dynamic range and a reconfigurable waveform. These cognitive features allow the creation of more capable and robust non-contact monitoring systems that are able to acquire both the respiratory rate and heartbeat while avoiding possible noise sources. The cognitive Bio-Radar is then an improvement of the common bio-radar, allowing it to sense the environment and intelligently choose the programmable RF parameters to better acquire the signal without affecting other local wireless systems. This optimizations will allow, in the future, for bio-radars to be more spectrum efficient, less prone to jamming and even reach better signal to noise ratios that where not possible in a conventional Bio-Radar implementations.

This cognitive bio-radar architecture analyses then the availability of the spectrum resources and uses this information to avoid collision with other transmitting RF devices. For this type of opportunistic operation the system has to periodically do spectrum sensing. The device constantly senses the RF spectrum and if a new signal is detected, the system will stop the transmission in that band as soon as possible to avoid interference with other RF devices. This cognitive feature also allows the avoidance of any type of unintentional or intentional jamming to the bio-radar due to the dynamic spectrum allocation.

1.2 Thesis background and objectives

This PhD thesis shares some of the concepts explored in the previous MSc dissertation entitled “Real time front-end for cognitive radio inspired by the human cochlea” held under the same supervisors of this PhD and had Instituto de Engenharia Electrónica e Telemática de Aveiro and Instituto de Telecomunicações as host institutions. The initial purpose of this PhD was to explore techniques that could enable an accurate spectrum sensing in cognitive radios. Therefore, the main goal is to determine the spectrum occupation in order to detect white spaces that could be used by opportunistic radios to transmit data.

The thesis was written during the process of three different research grants, two from Instituto de Engenharia Electrónica e Telemática de Aveiro research institute and one from Instituto de Telecomunicações. The thesis work started with an in-deep study on spectrum analysis methods by first exploring several implementations of cyclostacionary-based algorithms as cyclic autocorrelation and cyclic spectrum. In the course of this work it was discovered that the test statistics obtained by those methods were affected by noise that seem to had a relationship with the detected signal. The origin of the noise was studied and it was determined to be correlated spectrum leakage that could be used to improve the detection results. After exploring cyclostacionary methods, spectrum analysis algorithms based on analysis filter banks were studied, with a great focus in Discrete Fourier Transform (DFT) based filterbank polyphasic implementation and also multitaper analysis. Due to flexible nature of the DFT-based polyphasic implementation and greater computational performance compared with the multitaper implementation the first one was used on the following work. Eigenvalue based methods were also studied for spectrum analysis, this method allows a non quantized frequency response allowing a possible improvement in the frequency resolution. Nevertheless it was decided that the lack of ability to obtain a consistent frequency resolution was non optimal in future spectrum sensing applications and the method was not further pursued.

After exploring the spectrum analysis methods the focus was on noise model extraction. The noise model is dependent on the used method of spectrum analysis, therefore a good knowledge on the probability density function of the noise model is essential to determine the threshold that is used to classify the data between signal or noise. With a good knowledge of the noise model it is then possible to implement a Constant False Alarm Rate (CFAR) signal detection technique. The CFAR detection methods were explored and the first analysed was the energy detection. To determine a dynamic threshold for the energy detection the Expectation Maximization (EM) algorithm was evaluated. Using an energy estimator the received RF data energy can be modeled by a Gaussian Mixture Model (GMM). This allows the use of the EM algorithm with a GMM model to determine dynamically an estimation of the noise floor and then allowing the determination of a flexible threshold. The EM algorithm also has the advantage of determining the number of users in the channel and their occupation of the medium in time slots. The same algorithm was then expanded to two dimensions to be used in a two antenna receiver, showing improved results.

A novel subtractive histogram method based on the energy estimation histogram was developed to create a more computational efficient alternative to the EM algorithm. This method analyses the histogram in order to estimate the number of active users and their received energy. The next step was the development of a novel method based on a dual antenna receiver phase coherence detector which allows the determination of the spectrum occupation without the need of noise floor power estimation. This methodology allows to bypass the noise model estimation uncertainties that would induced error in the threshold. Furthermore, with the phase coherence detector is possible to implement a spatial spectrum sensing system by also determining the Direction Of Arrival (DoA) of the signal.

The phase coherence algorithm was also studied and evaluated for a hardware implementation in Field-Programmable Gate Array (FPGA). The implementation architecture was developed in order to allow real-time implementation of the phase coherence algorithm for a continuous evaluation of the streaming data coming from the ADCs. The algorithm was implemented in a FPGA development board that communicates with a custom protocol build on top of Ethernet Transmission Control Protocol (TCP).

Due to the given range of the work performed, this PhD thesis is then composed by an interception of all contributions, which are summarized in the following points:

- Usage of the cyclostacionary analysis leakage for signal detection improvement;
- Utilization of a Gaussian mixture model for spectrum sensing in conjugation with expectation maximization algorithm for one and two receiver elements;
- Estimation of the number of transmitting users and their received power with both expectation maximization and subtractive histogram method;
- Spatial spectrum sensing implementation based on phase coherence of a two antenna system;
- Hardware implementation of the phase coherence algorithm.

1.3 Thesis organization

This thesis is organized in six chapters that were developed to be self-contained but also part of the global structure.

- Chapter 1 describes the motivation that led to the development of this thesis, addressing new methods that would allows in the near future a more efficient usage of the spectrum. The cognitive radio implementation that is built in a SDR platform is analysed and upcoming implementations of cognitive radio architecture are explored. It is also explained the path taken in order to obtain the main contributions from this PhD work.
- Chapter 2 analyses spectrum sensing, the ability of the determining the occupation of wide bandwidth of the spectrum. The description of spectrum sensing is divided in three areas. The first is the spectrum analysis witch is detailed in Section 2.1 where several analysis methods are explained. The first one, and more simple, the periodogram, then filter banks with a uniform DFT polyphasic efficient implementation, multitaper method, cyclic spectrum and the section ends with eigenvalue analysis from the covariance matrix. In Section 2.2 the theory of signal detection and the binary decision of determining a channel occupation, is explored. This section dedicated to the analysis of spectrum sensing is concluded with Section 2.3 where the noise model, which is used to determine the threshold of the binary decision is explained and effects such as the SNR wall are detailed. In Section 2.4 the performance comparison between spectrum sensing methods is analysed with a focus in the Receiver Operating Characteristic (ROC) curve.
- Chapter 3 describes GMM analysis in spectrum sensing. In Section 3.1 it is evaluated how a shared spectrum environment can be described with a GMM and the considerations of this modeling. In Section 3.2 a novel subtractive histogram method that analyses the received signal energy histogram to obtain the number of users and their received energy is explored. In Section 3.3 the EM algorithm is explored to determine the number of users and their occupation of the channel through time using one antenna element. In Section 3.4 the EM algorithm is used in conjugation with the data acquired from two antennas, where both phase relationship between elements and the energy received from each one is analysed.

- Chapter 4 explores the application of spectrum sensing in the recent trend of Multiple-Input and Multiple-Output (MIMO) communications using highly directional transmissions. The determination of both the channel occupation and DoA of the detected signals is called spatial spectrum sensing and allows an even more efficient reuse of spectrum resources. An hardware implementation of the phase coherence algorithm for spectrum sensing based on FPGA is also studied and implemented.

- Chapter 5 closes this thesis by drawing the principal conclusions and interpreting the obtained results showing possible future research topics.

1.4 Main contributions

This PhD work produced relevant scientific contributions that were accepted in both conferences [C], journals [J] and book chapter [B] that are addressed in the thesis.

- [B1] - D. Malafaia, J. Vieira, A. Tomé “Part I: Networks of the Future - Cognitive Radio and Spectrum Sensing”, M. Elkhodr, Q. Hassan, S. Shahrestani “Networks of the Future - Architectures, Technologies and Implementations”, CRC Press 2017

This chapter starts by introducing the topics of SDR and the consequent cognitive radio with an overall of these architectures. The key element for cognitive radio is the ability to detect unused RF spectrum, this technique is called spectrum sensing. In this chapter the spectrum sensing is divided in three areas: first the spectrum analysis, followed by signal detection and noise model. Different spectrum analysis techniques are explored and explained. In signal detection, the binary decision of determining a channel occupation is explained. The noise model analyses the determination of the threshold for that decision. The chapter ends by exploring the application of spectrum sensing in the recent trend of MIMO communications with highly directional transmissions, by using spatial spectrum sensing to allow an even more efficient reuse of spectrum resources.

- [J2] - D. Malafaia, J. Vieira, A. Tomé “Adaptive Threshold Spectrum Sensing based on Expectation Maximization algorithm”, Physical Communication Journal 2016

In this article we purposed a novel method for spectrum sensing, based on expectation maximization algorithm applied to the histogram of the moving average signal power. The method enables the estimation of the number of active users in a given frequency band, the power received from each user, the occupied time slots and the front-end noise floor. The proposed approach takes advantage of the statistical properties of the averaging estimator output, which allows to model the received estimated power as a GMM. This model represents the distributions of the users transmitted signal power as well as the system noise floor. Moreover, the Gaussian with the lowest mean that is related with the noise floor, can be used to estimate an adaptive threshold for a constant false alarm rate detector. Finally, the method was validated in a Wi-Fi experimental setup, where real-world data was acquired with a SDR.

- [J1] - D. Malafaia, B. Oliveira, P. Ferreira, T. Varum, J. Vieira, A. Tomé “Cognitive bio-radar: The natural evolution of bio-signals measurement”, Journal of Medical Systems 2016

In this article we discussed a novel approach to bio-radar, contactless measurement of biosignals, called cognitive bio-radar. This new approach implements the bio-radar in a SDR platform in order to obtain awareness of the environment where it operates. Due to this, the Cognitive Bio-Radar can adapt to its surroundings in order to have an intelligent usage of the radio frequency spectrum to improve its performance. In order to study the feasibility of such implementation, a SDR based bio-radar testbench was developed and evaluated. The prototype is shown to be able to acquire the heartbeat activity and the respiratory effort. The acquired data is compared with the acquisitions from a Biopac research data acquisition system, showing coherent results for both heartbeat and breathing rate.

- [C6] - D. Malafaia, J. Vieira, A. Tomé "Energy based clustering method to estimate channel occupation of LTE in unlicensed spectrum", IWINAC 2017

In this article we propose a subtractive histogram clustering method to estimate the number of LTE users based on the uplink energy probability density distribution sensed by an RF front-end. The energy of the signal is estimated and its histogram is analyzed to determinate the number of different distributions. As the energy estimation of the sensed LTE uplink can be modeled by a Gaussian mixture, this allow us to have *a priori* information that allows us to determine the number of distributions presented. The lowest value Gaussian distribution can be used to accurately estimate the noise floor and the remaining distributions allow us to estimate the number of LTE users and their received power.

- [C5] - D. Malafaia, J. Vieira, A. Tomé "Channel utilization analysis based on EM algorithm for 5G spectrum management", 9th Congress of the Portuguese Committee of URSI 2015

In this article we addressed a novel method, based on the expectation maximization algorithm, that allows the estimation of several parameters like the number of active users in a given frequency band, the power received from each user, the occupied time slots and the front-end noise floor. The method takes advantage of the behavior from a signal under an estimator, that allow to model the analysed data from users and system noise floor as a Gaussian mixture. The number of different Gaussian distributions allows us to determine the number of users in the channel, as well as associate the occupation to a given user. The lowest mean in the mixture give us an estimation for the noise floor.

- [C4] - D. Malafaia, J. Vieira, A. Tomé "CFAR energy detector for LTE spectrum sensing", CONFTELE 2015

In this article a energy detection method with CFAR was implemented to detect temporal white spaces on the LTE uplink frequency band. Accordingly with the LTE protocol there are always, in each uplink frame, free resource blocks. Those can be used to dynamically estimate the noise floor level from an analysis filter bank. The method is validated in laboratory using LTE signals that are acquired trough a SDR.

- [C3] - D. Malafaia, J. Vieira, A. Tomé "Improving performance of bio-radars for remote heartbeat and breathing detection by using cyclostationary features", BIOSIGNALS 2015

In this article we presented a continuous wave radar created using a software defined radio platform that uses Doppler effect to measure the heart-rate and breathing. The measurements are evaluated using a classic energy detection method and a cyclic spectrum estimation technique, then the two methods are compared. The results show that by taking advantage of the cyclic autocorrelation of the bio-signals we can get better detection than the usual energy detection.

- [C2] - D. Malafaia, J. Vieira, A. Tomé "Blind detection of cyclostacionary signals taking advantage of cyclic spectrum leakage", EuMW 2014

In this article we described a novel process for blind detection in spectrum sensing taking advantage of the cyclostationary features of any digital modulation that uses a finite number of distinct signals to represent digital data. Traditional models only look at any peak in a cyclic spectrum that satisfies a given threshold, in this method we take advantage of the cyclic spectrum leakage to identify a signal. This method shows better performance at detecting low Signal-to-Noise-Ratio (SNR) signals than the traditional cyclostationary signal detection.

- [C1] - J. Vieira, A. Tomé, D. Malafaia "Wideband Spectrum Sensing for Cognitive Radio", EUSIPCO 2014

In this article we proposed a wideband spectrum sensing system based on hybrid filter banks. The polyphase implementation of the digital counterpart of the filter bank can be modified to include a parallelized version of the Fast Fourier Transform (FFT) avoiding this way any sampling rate expanders. In this work we show how to incorporate the FFT block in the structure in order to estimate the wideband frequency contents of the signal. The proposed structure is particularly suitable FPGA based implementations.

There is also an article submitted and currently waiting for review. The article was submitted in IEEE Wireless Communications Magazine and is called "Spatial Spectrum Sensing Implementation based on Dual Antenna Receiver Phase Coherence" it is based on part of the Chapter 4 of this thesis.

Chapter 2

Spectrum Sensing theory

Spectrum sensing has been an intense research topic with many different solutions being proposed in the literature. The main research focus is to create a reliable method that is able to detect the occupation of a given frequency band, even for unfavourable signal to noise ratio conditions [37]. In order to sense a wide span of the RF spectrum and evaluate which frequency bands are being occupied and which are free to use, three tasks need to be ensured:

- **Spectrum Analysis**, which comprises the frequency analysis of a received RF signal by computing an estimation of its frequency representation. This analysis comprises the separation of the acquired signal into frequency bands with uniform or variable bandwidth.

- **Noise Model** determination, where the noise process characteristics are *a priori* calculated or estimated in real-time. The noise model estimation is calculated using the spectrum analysis results in time and/or frequency.

- **Signal Detection**, whose goal is to decide about channel occupation of the spectrum estimation. The noise model allows to compute a threshold that is used to make this decision. The most common way to output the occupation is by a hard binary decision, either a given frequency band is occupied or it is free to use.

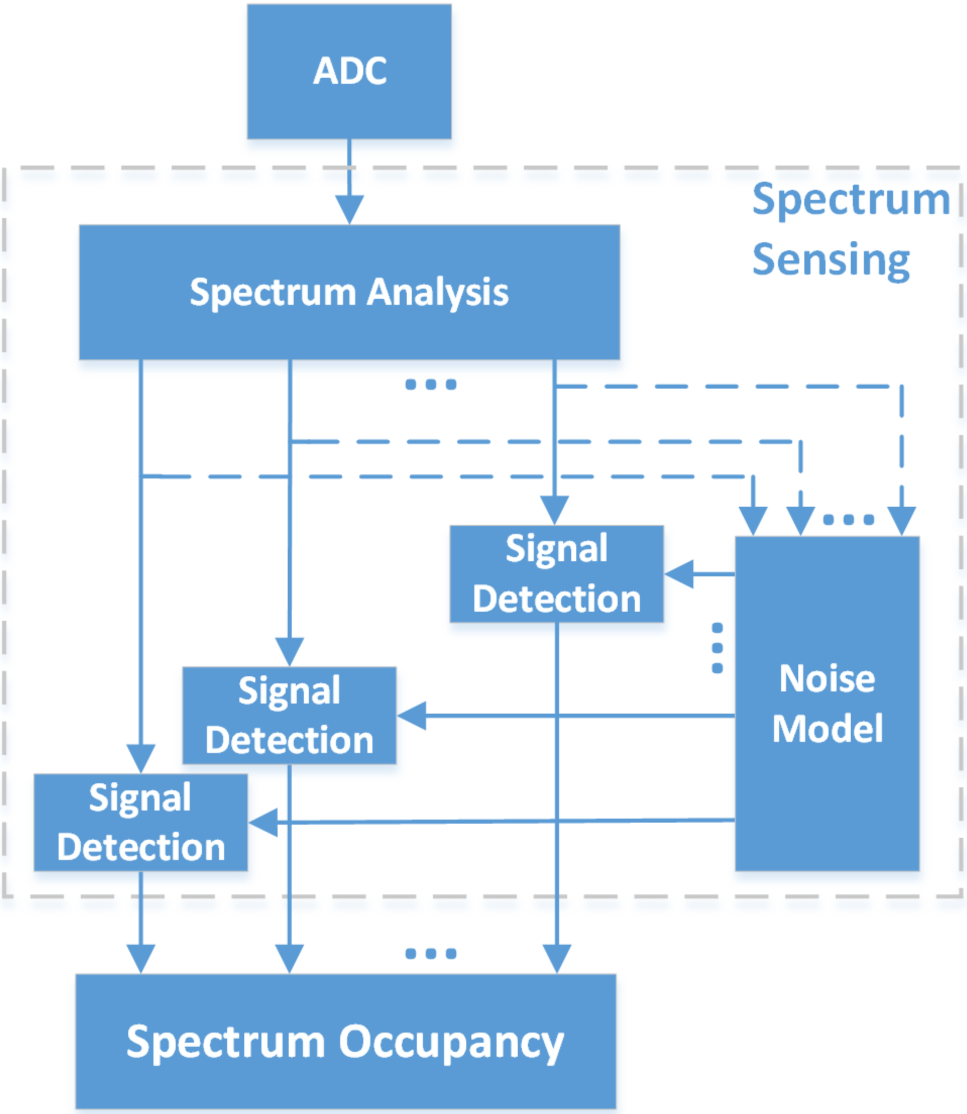

Figure 2.1: Spectrum sensing components block diagram.

A spectrum sensing unit will then operate as illustrated on Figure 2.1. A wide frequency band of the spectrum is acquired by an ADC. The data is then analysed by a spectrum estimation algorithm, to obtain the most accurate representation of the acquired signal into frequency bands. These bands are then analysed in order to detect short “quiet periods” as defined in various standards [38]. In order to achieve real-time spectrum sensing the algorithm implementation needs to have low computational costs. For a reliable detection the implemented algorithm also needs to have low spectral leakage. The frequency representation is then used to discern if a signal is present in that band.

The noise model is fundamental to the signal detection decision, as it allows to determine if the estimated spectrum data represents signal or noise. If the data does not fit the noise model then we are in presence of signal. The noise model estimation methods can be divided in two large groups:

- **Dynamical noise model**, normally used in dynamical threshold energy detection methods [39]. The outputs of the spectrum analysis block are used to calculate the noise floor parameters such as its probability distribution, variance and power level. It is expected that the values of the noise parameters change over time due to external effects, such as channel interference from out-of-band emitters, or from effects of the front-end itself such as an automatic gain control system. Due to these effects, a single evaluation of the noise floor is not enough, requiring then a dynamic estimation that is capable of handling energy fluctuations.

- **Fixed noise model**, that is unaltered during the spectrum sensing and creates a fixed threshold. In 802.11 protocol energy detection, the noise energy is assumed to be always below the hardware sensitivity level plus 20dBm, anything above that level is assumed to be signal [40]. For statistical moments based detection, the noise distribution can be considered to be a Gaussian distribution, while the signal can be, for instance, modeled by a Raleigh distribution. In that case the detection can be achieved by estimation of the kurtosis [41]. In eigenvalue based spectrum sensing, the noise covariance matrix can be assumed to always be a Wishart random matrix and the noise eigenvalues distribution can be calculated to then allow the application of maximum-minimum detection techniques [42]. In cyclostatiorary analysis the noise covariance can be assumed to be chi-square, while the signal can be modeled by a Gaussian distribution, allowing the use cyclostationary detectors [43].

While some methods assume a model not only for the noise but also for the signal, the signal's model is usually not used for signal detection. This is due to the small amount of information that can be used to represent the signal [42]. For instance, it may be assumed that all the detected signals follow a Rayleigh distribution as it is an appropriate distribution model for multi-path environments. However, in a direct transmission scenario, with lack of multi-path reflections, the Rayleigh distribution will be a poor model. Other reasons include the large number of modulation techniques that can be used to transmit the RF signal and the wide range of possible power level of the received signal. Due to these reasons the detection threshold is usually defined based not on the transmitted signal, but on the noise model. The noise model is then used by the signal detection system to calculate a threshold that is used to analyze a frequency span to determine if the band is occupied, while getting the best relationship possible between false and missed detection. The false alarm is usually specified in the standards [38].

2.1 Spectrum analysis

The chosen method for spectrum analysis can make the difference between the capability to detect weak signals or occluding them under leakage noise. Spectral leakage occurs when the signal energy contributes not only to one frequency band but also spreads to the nearby bands. The effects caused by the spectral leakage can be attenuated by using the proper spectrum analysis method. A Power Spectrum Density (PSD) comparative is shown on Figure 2.2.

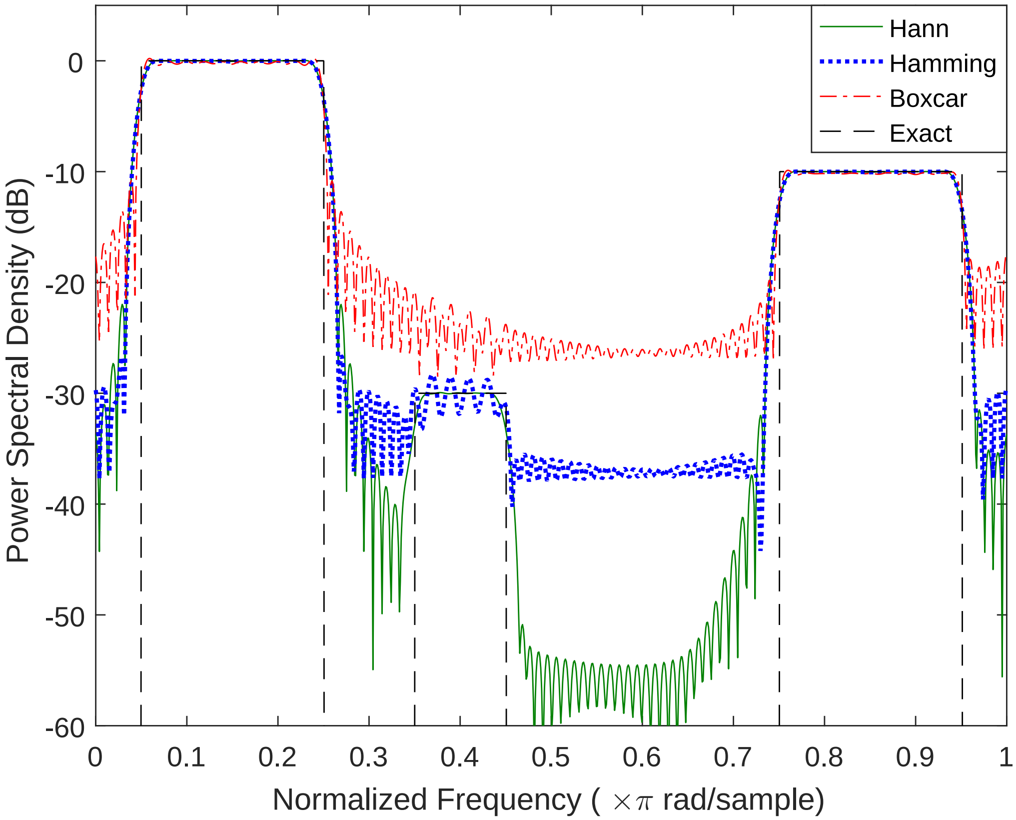

Figure 2.2: Example of a signal PSD calculated using a filter bank with three different prototype filters.

In this synthetic example, several window functions generate the prototype filter of the same filter bank and their results are compared to the exact PSD that is a sum of three different passband signals. The results show that a filter bank using the Hann function as prototype filter is able to detect the weakest passband signal that, if using the boxcar function, would be otherwise hidden.

It is then important to know and understand the various methods for spectrum analysis in order to pick the best ones for a given application. Some of the most relevant ones are:

- **Periodogram**: The most common way of analyzing the spectrum as it has low computational and implementation complexity. It uses a constant number of samples and analyzes them using a FFT that is then squared and the result integrated [44].

- **Eigenvalues**: spectrum sensing literature addresses the signal detection with the relation between the eigenvalues of the correlation matrix of the signal [42]. However, the eigenvectors of the matrix can also be considered as coefficients of a filter bank. Moreover, the eigenvalues are an estimate of the energy at the output of the corresponding eigenvector filter as shown in the submitted article [45]. The uniqueness of the method is that the eigenvector filter bank does not represent equally spaced frequency bands as in Fourier based methods.

- **Cyclic Spectrum**: Takes advantage of cyclostationary behavior of certain signals to improve the spectrum analysis, making it a good method for signals with periodic autocorrelation behavior as for example digital modulated signals [46]. The calculated cyclic spectrum features can also be used for signal modulation recognition [47].

- **Filter bank**: A filter bank is an array of band-pass filters that will decompose a given signal into multiple components, each component will then be a frequency band of the original signal. This process shows good performance for spectrum analysis due to its low spectral leakage [48]. Signal decomposition is performed by an analysis filter bank, that usually splits the signal using the same prototype filter that is centered in different, but equidistant, central frequencies. This method uses the concept of maximal energy concentration in a given central frequency with a constant bandwidth. A computational efficient implementation is achieved with the polyphasic decomposition of the prototype filter [49].

- **Multitaper**: The multitaper method may be seen as a filter bank that, instead of one, uses multiple orthogonal prototype filters, usually Slepian sequences, to improve the variance and reduce leakage [50].

The selection of a method of spectrum analysis should accomplish the best combination of three criteria. It is of critical importance for the method to have the lowest spectral leakage in order to avoid obtaining a smeared version of the original continuous-time spectrum, that would reduce the ability of detect spectrum holes. Also important is to have the least number of acquired samples needed for a correct representation of the spectrum to allow a fast sense of the spectrum to quickly occupy spectrum opportunities. Finally, the algorithm must not be expensive in terms of computational resources in order to be deployed in mobile devices and have a low power consumption. By achieving these criteria we then have the optimal system to, quickly and in real-time, identify spectrum opportunities and avoid possible collision with other concurrent users.

2.1.1 Periodogram

The most classical way to do spectrum estimates is using a periodogram [51]. First used in meteorological phenomena it allows for direct spectral estimate of the power spectral density function, but this method shows some problems, the principal is the bias produced by spectral leakage. There are usually two kind of bias, the leakage bias and the local bias [52]. The local bias is due to the use of a low number of bins that require for each one to have a large bandwidth. The leakage bias is given by any strong peaks in a specific frequency that spread in the neighboring bins.

The leakage bias can be redistributed to, according to the application, reduce its influence in the estimation. This operation can be applied in spectrum estimation by using a window function before the frequency transform.

For a $x(n)$ discrete data sequence, with N points, the windowed spectrogram can be written as,

$$\hat{S}(f) = |\sum_{n=0}^{N-1} x(n)w(n)e^{-2\pi i f n}|^2 \tag{2.1}$$

where $w(n)$ are the coefficients of the window function. This method is also known as single-taper and $w(n)$ the taper function [53].

2.1.2 Eigenvalues

Let us consider the received signal $x(n) = [x(0), x(1), ..., x(N-1)]$ with N samples. Its multidimensional variant, with M dimensions (also called the smoothing factor), is obtained by $\boldsymbol{x}_k = [x(k-1+M-1), ..., x(k-1)]$, $k = 1, ..., K$ where $K = N - M + 1$ [54]. These lagged vectors form the columns of the related data matrix $\boldsymbol{X}$, called a trajectory matrix [55]. The columns of M-dimension $\boldsymbol{X}$ matrix are given by the $\boldsymbol{x}_k$ vectors.

$$\boldsymbol{X} = \begin{bmatrix} x(M-1) & x(M) & \cdots & x(N-1) \\ x(M-2) & x(M-1) & \cdots & x(N-2) \\ \vdots & \vdots & & \vdots \\ x(0) & x(1) & \cdots & x(N-M) \end{bmatrix} \tag{2.2}$$

Note that the trajectory matrix has identical entries along its diagonals. Such a matrix is called a Toeplitz matrix [45]. From a segment of N samples of received data $x(n)$, M consecutive output samples can be formed. In practice, the covariance matrix of the input signal is unknown as it is only analysed a finite number of samples. Thus, the unstructured classical estimator of $\boldsymbol{R}$, the sample covariance matrix [56], can be used and is defined as,

$$\boldsymbol{R} \triangleq \frac{1}{N}\boldsymbol{X}\boldsymbol{X}^H = \frac{1}{N}\sum_{k=1}^{K} \boldsymbol{x}_k \boldsymbol{x}_k^H \tag{2.3}$$

where H is the Hermitian. The eigenvalues of the covariance matrix can then be calculated from the characteristic equation,

$$\det(\boldsymbol{R} - \lambda I) = 0 \tag{2.4}$$

where det is the determinant, λ give us the eigenvalues and I is the identity matrix. The $\lambda_{max} = \lambda_1 > \cdots > \lambda_L = \lambda_{min}$ is then the eigenvalue decomposition of the covariance matrix of the input signal.

2.1.3 Cyclostationary analysis

2.1.3.1 Introduction

There are many processes in nature that manifest periodic behavior [57]. This kind of processes that may not be periodic functions in time, can give rise to random data whose statistical characteristics do vary periodically with time and are called cyclostationary processes [58]. In telecommunications the periodicity can be due to the signal modulation, sampling, multiplexing and coding operations. When, for example, a limited constellation with a finite number of distinct signals to represent digital data is used, will lead eventually to the same signal being repeated that will create a periodic auto-correlation.

Wide-sense (second order) cyclostationary stochastic processes have autocorrelation functions that vary periodically with time and also have a periodic mean. This type of processes, under mild regularity conditions, can be expanded in a Fourier series whose coefficients, referred to as cyclic autocorrelation functions, depend on the lag parameter. The frequencies, called cycle frequencies, are all multiples of the reciprocal period of cyclostationarity [59]. For example in Orthogonal Frequency-Division Multiplexing (OFDM) a cyclic prefix is used that by repeating part of the frame that is being sent will create a periodic autocorrelation that can be used to detect cyclostationarity [60, 61, 62].

The importance of cyclostationarity based methods is that they provide a way to separate cyclostationary signals from additive white Gaussian noise which by definition is purely stationary with no correlation, while modulated signals are cyclostationary with cyclic autocorrelation due to the redundancy of signal periodicity. A cyclostationarity analysis can then differentiate the noise from the primary users of the spectrum and detect the presence of any communication [63]. This technique is in various situations better than traditional detection methods [64] as, for example, the energy detection method and allows us to detect in a wide spectrum band, signals that couldn't be identified in any other way. This is quite important in, for example, cognitive radio networks to avoid unintentional interference of a given communication channel.

2.1.3.2 Cyclostacionary analysis methods

In order to identify the presence of a cyclostationary digital signal in a given sampled spectrum we usually use two mathematical operations: cyclic autocorrelation and cyclic spectrum. These two methods will show unique features when in presence of a cyclostationary based signal.

Basic notions of cyclic autocorrelation To understand cyclic autocorrelation we first need to define what is correlation. Correlation is a mathematical operation that allows us to measure the degree to which two signals are similar and is the expected value of the inner product of the two signals. For the autocorrelation the procedure is similar, but instead of having two different signals we use the inner product of the signal with itself at a different time. By definition a cyclostationary signal has a periodic autocorrelation of a signal R_x. Lets define that period by being N_0 and the lag being τ, then:

$$R_x(n + N_0, \tau) = R_x(n, \tau). \tag{2.5}$$

If a periodic correlation exits then it can be proved [59] that $x(n)$ and its frequency-shifted version $x(n)e^{j2\pi k/N_0 n}$are correlated for any $k \in \mathbb{Z}$.Then we can define the cyclic autocorrelation as being:

$$R_x^\alpha(\tau) \triangleq E\{x(n + \tau)x^*(n)e^{-j2\pi\alpha n}\} \tag{2.6}$$

with $\alpha = k/N_0$ and $*$ the conjugate. Expanding the equation we have:

$$R_x^\alpha(\tau) = \lim_{N\to\infty} \frac{1}{N} \sum_{n=0}^{N-1} x(n + \tau)x^*(n)e^{-j2\pi\alpha n} \tag{2.7}$$

where N is signal number of samples.

As the signal is cyclostationary with a periodic autocorrelation in N_0 there is no need to sum the inner product of the signal with itself delayed to infinity as we did in (2.7). Using only the available number of samples N, we can then remove the limit from the equation and write:

$$R_x^\alpha(\tau) = \frac{1}{N} \sum_{n=0}^{N-1} x(n+\tau)x^*(n)e^{-j2\pi\alpha n} \tag{2.8}$$

Using (2.8) it is then possible to detect if a stochastic process $x(n)$ exhibit cyclostationarity at the cycle frequency α. If it does then $R_x^\alpha(t) \neq 0$ [59].

Cyclic autocorrelation demonstration for a sinusoid The cyclic autocorrelation function is given by (2.7). Let us analyse the output of a sinusoid with unitary amplitude and a frequency of f_0:

$$R_x^\alpha(\tau) = \lim_{N\to\infty} \frac{1}{N} \sum_{n=0}^{N-1} \cos(2\pi f_0(n+\tau))\cos(2\pi f_0 n)e^{-j2\pi\alpha n} \tag{2.9}$$

it can be demonstrated that the result is:

$$R_x^\alpha(\tau) = \frac{1}{4}\delta(\alpha+2f_0)e^{-j2\pi f_0\tau} + \frac{1}{4}\delta(\alpha-2f_0)e^{j2\pi f_0\tau} + \frac{1}{2}\delta(\alpha)\cos(2\pi f_0\tau) \tag{2.10}$$

where δ is the Kronecker delta function. Knowing what to expect from the cyclic autocorrelation function for a sinusoidal input, we can validate the algorithm implementation by creating a simulation and compare it with this theoretical result.

Computational implementation of cyclic autocorrelation For a computational efficient implementation of the discrete time cyclic autocorrelation function $R_x^\alpha(n)$ from (2.8), the FFT of the product $x(n)x(n+\tau)$ can be used [58]. The discrete Fourier transform of a finite-energy discrete-time signal $x(n)$ can be defined as [65]:

$$X(f) = \sum_{n=-\infty}^{\infty} x(n)e^{-j2\pi fn} \tag{2.11}$$

it is then easy to see that that (2.7) is nothing more than the Fourier transform of $x(n+\tau)x^*(n)$ divided by $\frac{1}{N}$.

Let us consider the demonstration in (2.10) and compare it with an sinusoidal input with frequency of $f_0 = 0.05Fs$.

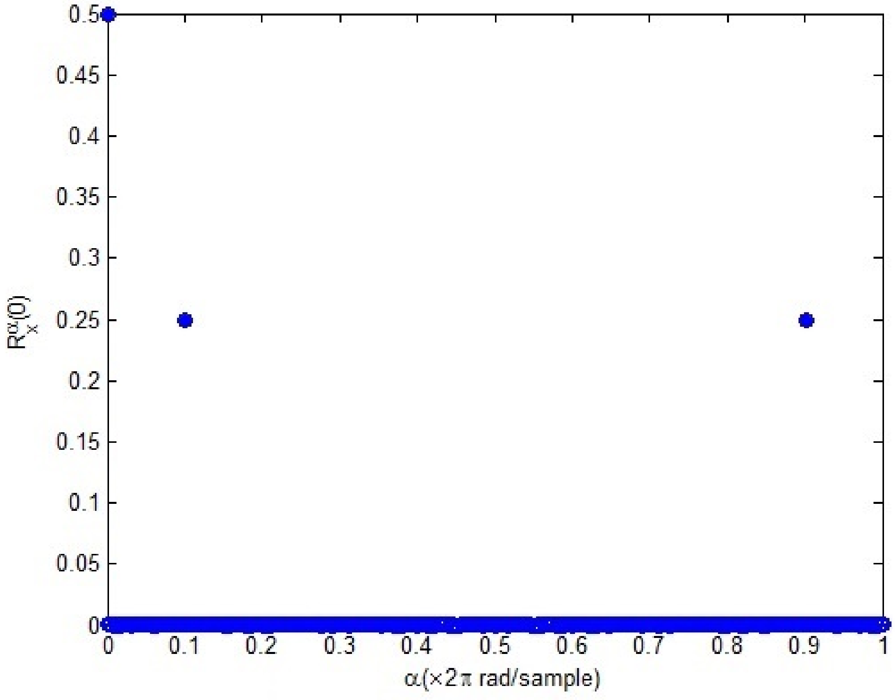

Figure 2.3: Cyclic autocorrelation of a sinusoid for $\tau = 0$.

As expected the simulation results for the $\tau = 0$ are the results that we achieved in the analytic way. The sinusoid was generated at $0.05Fs$ and as we can see the cyclic autocorrelation has peaks at the double of that frequency and at the image as well. The expected $\alpha = 0$ value is also present.

Cyclic Spectrum Another tool for analyzing cyclostationarity is the cyclic spectrum. To derive this function we do something very similar to the Wiene-Khinchin theorem [59] but applied to the cyclic autocorrelation from (2.8). The cyclic spectrum is then:

$$S_x^\alpha(f) = \sum_{\tau=-\infty}^{\infty} R_x^\alpha(\tau) e^{-j2\pi f\tau} \tag{2.12}$$

with $f = \pm\alpha/2$. That, once again, is nothing more than the Fourier Transform of the cyclic autocorrelation and can be calculated with the FFT of every τ from the previously calculated cyclic autocorrelation.

Using the cyclic spectrum for a band-pass signal the theoretical expected result is the one show in the Figure 2.4 [59].

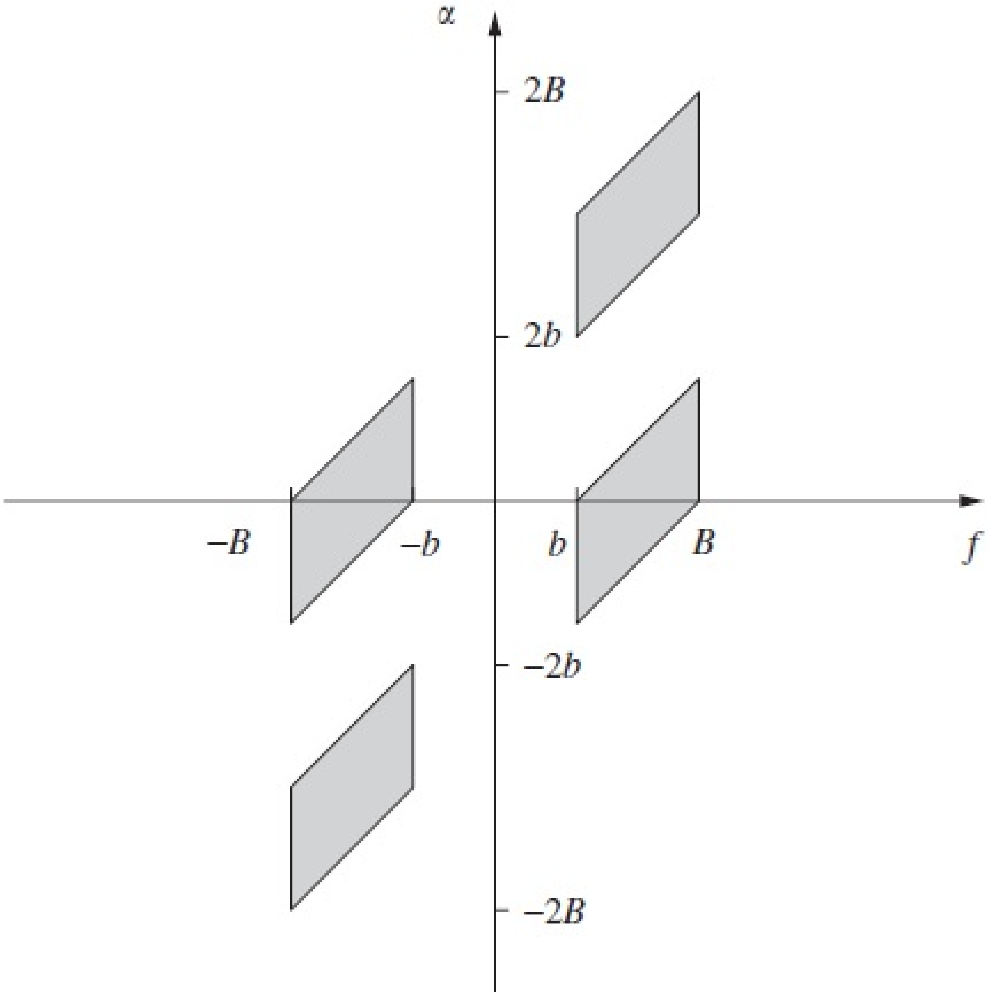

Figure 2.4: Theoretical cyclic spectrum of a band-pass signal .

being 'b' the lower cut frequency and 'B' the upper cut frequency. A simulation of a band pass signal with normalized central frequency of 0.25 and bandwidth of 0.3 would then give the same result as Figure 2.4 but with $b = 0.05$ and $B = 0.4$. The cyclic spectrum result is shown in Figure 2.5.

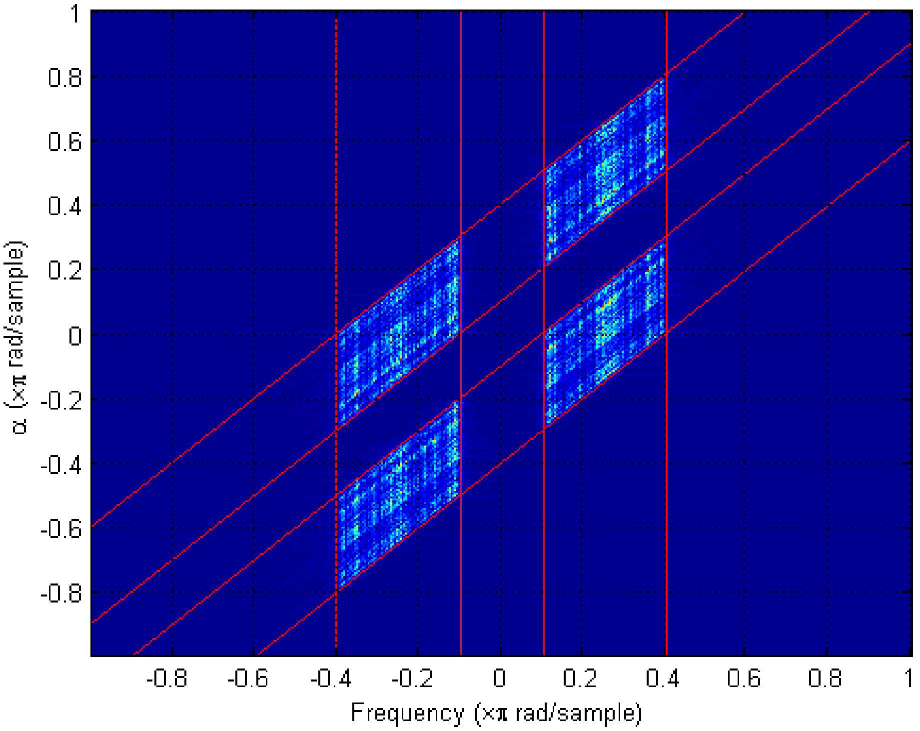

Figure 2.5: Cyclic spectrum of a band-pass signal, at red the theoretical lines .

As expected, the resulting cyclic spectrum of the simulated band-pass signal agrees with the theoretical results.

2.1.3.3 Contribution on cyclic spectrum behavior under noise

When the signal that is being received is corrupted with noise the cyclic spectrum will show leakage. This leakage is not uniform under all the domain of the cyclic spectrum but shows preference on the vertical and diagonal axis that intersect the expected results, as seen in the red lines of Figure 2.5.

Let us take a look in the following example that was done with a random Binary Phase-Shift Keying (BPSK) signal with a $Fc = 0.1Fs$, $BW = 0.04F$s, $SNR = -5$ dB with 1000 samples.

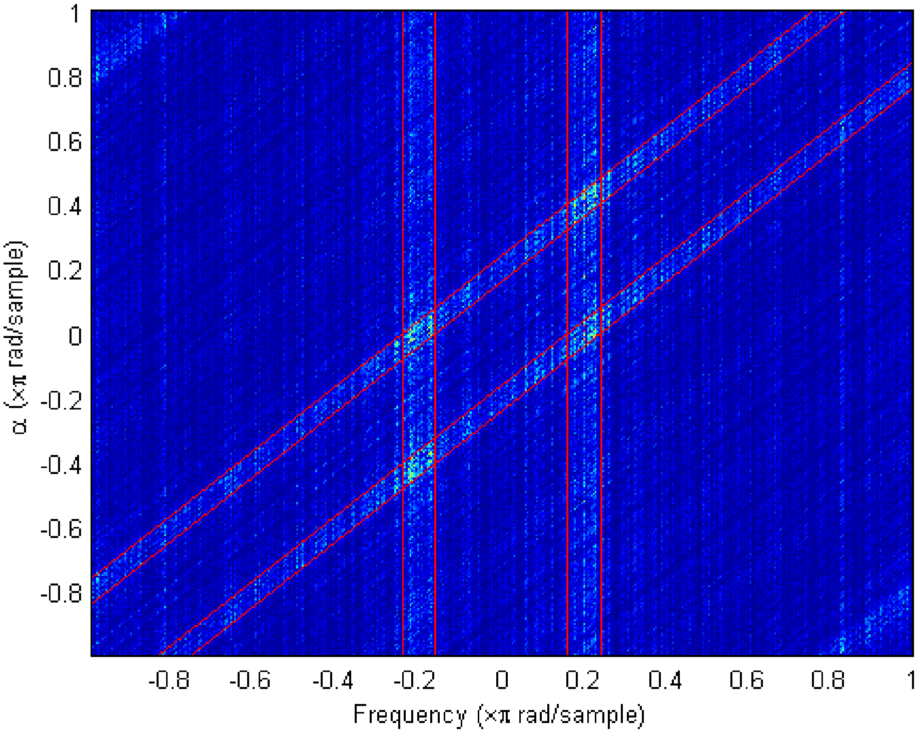

Figure 2.6: Simulation leakage in the cyclic spectrum of a BPSK signal.

As it can seen in Figure 2.6 there is both diagonal and vertical leakage on the cyclic spectrum results. We claim that this kind of leakage can help in the detection of signals, as is appearance depends on the central frequency and bandwidth of the signal in question.

Taking advantage of the cyclic spectrum leakage In order to take advantage of the spectrum leakage we propose the energy measurement of every diagonal and column of the two dimensional cyclic spectrum space.

This method is expected to improve the detection performance of the classical cyclic spectrum method that only makes a detection based on a single point of the domain. The maximum value of the dimensional cyclic spectrum space is then used to determine the occupied frequency.

Simulation Results To prove that we can indeed use both the diagonal and vertical leakage that is part of the cyclic spectrum a simulation was created to test each individual methods. We will then compare three different algorithms:

- Power method: Where the FFT of the signal under test is performed and the bin with the maximum value is obtained. The position of the maximum value gives us the frequency of the detected signal.
- Cyclic spectrum: Where the cyclic spectrum of the signal under test is performed, to find out the position, on the two dimensional domain, of the maximum value and thus determining the signal frequency.

- Cyclic spectrum taking advantage of the vertical and diagonal cyclic spectrum leakage: Where the cyclic spectrum of the signal under test is performed, and the power of each diagonal line and vertical line of the cyclic spectrum is calculated. Both are then taken into account to assign a value of power to each cycle frequency α. This is done by summing the normalized diagonals and columns for the same frequencies. After that, the frequency with the highest power is determined.

Each method has a successful detection when the identified frequency is inside the bandwidth of the generated signal.

For the next simulation we used a 16 Quadrature Amplitude Modulation (16-QAM) constellation signal with $Fc = 0.15Fs$, $BW = 0.02Fs$ and 1000 samples. An average of 5000 simulation was done and the results are plotted in Figure 2.7.

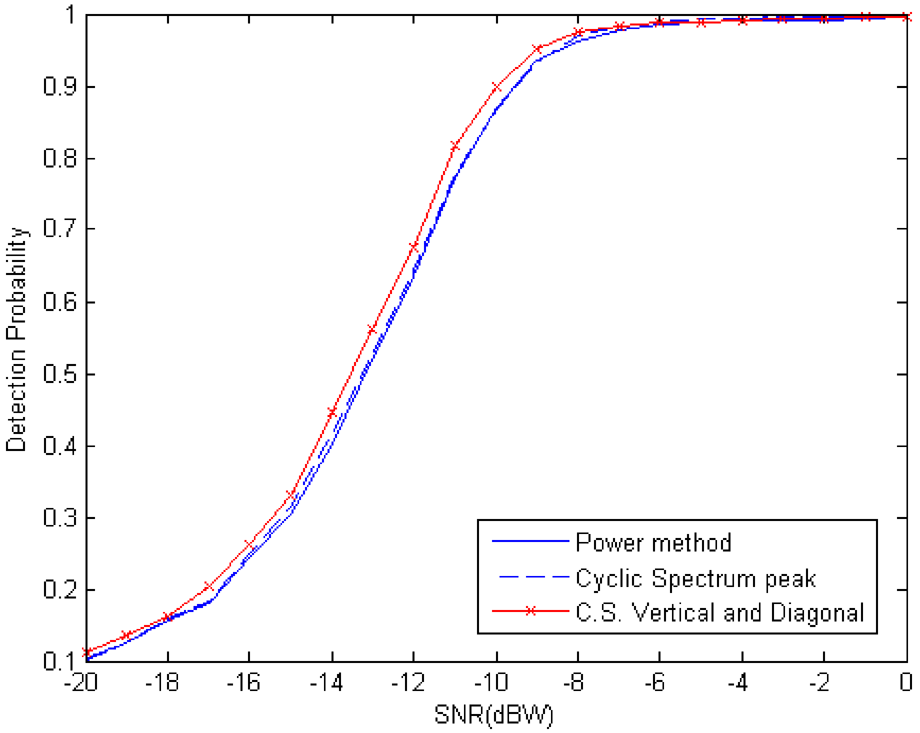

Figure 2.7: Detection probability comparison between methods.

As visible from the figure, the red crossed line where the vertical and diagonal leakage of the cyclic spectrum is used to improve the results, achieved a better detection probability compared to the frequency power method and the classical cyclic spectrum method. We expect to see even better results of the cyclic spectrum methods for signals with higher cyclostationarity features or with more samples than those used in this test.

There is still margin for improvement in the obtained results, by having *a priori* information of the signal's bandwidth there is no need to evaluate each cycle frequency individually and can be group in intervals. By using this frequency grouping, detection probability will increase as the method uses more signal power for each measurement. With the same example we test the diagonals and columns of the cycle spectrum in groups of 20 as we have $BW = 0.02Fs$ and 1000 samples.

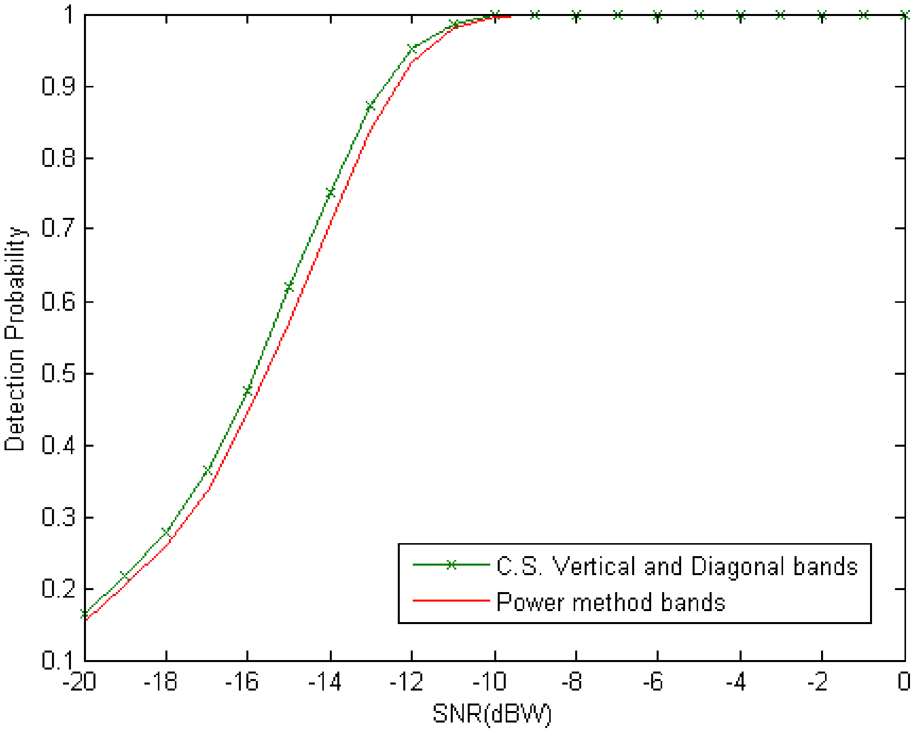

Figure 2.8: Detection probability comparison between methods using bands.

Once again the implementation of the vertical and diagonal leakage, at green, delivers better results than the power method also grouped in samples with the size of the bandwidth of the signal used as input.

Discussion from the contribution We showed how can the cyclic autocorrelation and cyclic spectrum be implemented in a simulation efficiently and with simulations we were able do demonstrate that it is possible to use the cyclic spectrum leakage to improve it is performance in detection, in blind conditions, of cyclostationary signals.

2.1.4 Filter bank

2.1.4.1 Introduction

A filter bank is an array of band-pass filters that divide the input signal in various components, each one containing a frequency band of the original input. The process of decomposing the signal is performed by an analysis filter bank. A Short Time Fourier Transform (STFT) can be view as a filter bank. Each bin of the transform is centered in an equidistant frequency grid and will filter the signal in frequency bands. It is well known that this analysis method suffers from the leakage phenomenon that can be minimized as illustrated in the Figure 2.9 by using a non-rectangular window with coefficients $h(n) = [h(0), h(1) \ldots h(M-1)]$ leading to a better frequency response behavior but not enough to spectrum sensing purposes where a higher dynamic range is needed.

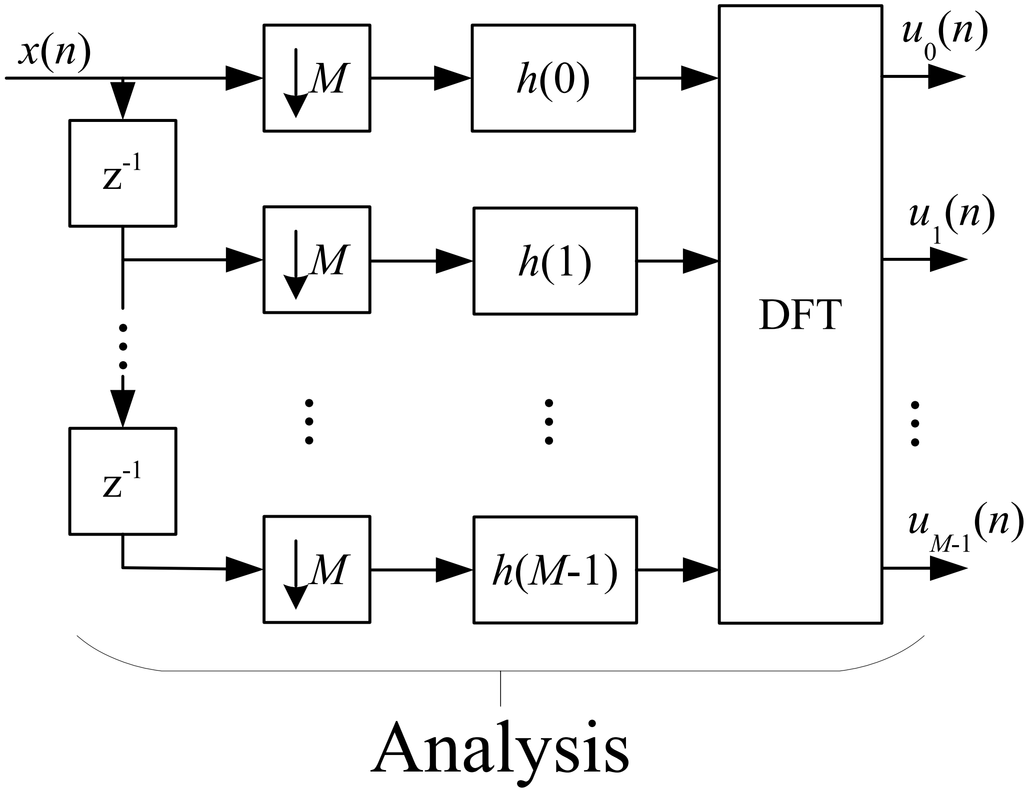

Figure 2.9: Non-rectangular window implementation for a DFT analysis filter bank.

One of the characteristics of the STFT is that for, non-overlapping windows, it requires for the window length to be equal to the number of channels of the filter bank and to the decimation factor. To improve the frequency response of the STFT, the number of coefficients of the prototype filter $h(n)$ must be larger than the number of frequency bands. This type of filter bank has a higher flexibility on the design of the prototype filter frequency response allowing to reduce the frequency leakage to a desired level by paying the price of having a larger analysis window, delay and processing complexity. However, this type of filter bank can be implemented quite efficiently using a polyphase decomposition of the filter and a DFT as shown in the Figure 2.10. where $H_0(z), H_1(z), \dots$ are the polyphase components of the prototype filter.

Polyphase implementation of a DFT based filter bank For an analysis filter bank with M channels each one having a $H_k(z)$ frequency response of a frequency modulated prototype filter $H(z)$ with $1/M$ bandwidth of the total used frequency spectrum we have,

$$H_k(z) = H(ze^{j\frac{2\pi k}{M}}), k = 0, 1, ..., M-1 \tag{2.13}$$

with $z = e^{j\omega}$we get,

$$H_k(e^{j\omega}) = H(e^{j\omega}e^{\frac{j2\pi k}{M}}) = H(e^{j(\omega+\frac{j2\pi k}{M})}). \tag{2.14}$$

As each channel has a limited bandwidth we can decimate the input that goes to each channel. The most efficient way to do this is trough a polyphasic filtering. For this method we need to divide our prototype filter in its various channels each filtering a different phase of the signal. So our prototype filter can be given by

$$H(z) = \sum_{l=0}^{M-1} H_l(z^M)z^{-l}. \tag{2.15}$$

Where $H_l(z)$ is each phase coefficients of the prototype filter and the coefficients are interpolated, $H_l(z^M)$, as their are followed by a decimation. But if we use the noble identities to decimate the input signal first we can avoid the interpolation of each filter phase coefficients. Each phase of the polyphasic filter is given by,

$$H_l(z) = \sum_{l=0}^{N/M-1} h(nM + l)z^{-n} \tag{2.16}$$

where N is a multiple of M and $N/M - 1$ is the number of coefficients in each channel of the polyphasic implementation, $h(n)$ is the coefficients of the prototype filter, l is the phase and M is the total number of phases of the filter. If we take (2.15) and substitute in (2.13) we get,

$$H_k(z) = \sum_{l=0}^{M-1} H_l((z\omega^k)^M)(z\omega^k)^{-l} \tag{2.17}$$

where $(z\omega^k)^M = z^M\omega^{kM} = z^M e^{\frac{j2\pi}{M}M} = z^M$, then we have,

$$H_k(z) = \sum_{l=0}^{M-1} z^{-l}H_l(z^M)\omega^{-kl}. \tag{2.18}$$

Each output will be decimated so if we apply the noble identity, by moving the decimation beyond H_l in (2.18), we will then have,

$$H_k(z) = \sum_{l=0}^{M-1} z^{-l}H_l(z)\omega^{-kl} \tag{2.19}$$

being $\omega^{-kl} = e^{-j\frac{2\pi}{M}kl}$ we can see the similarities between 2.19 and the DFT equation, as is it defined by

$$X_k = \sum_{n=0}^{N-1} x_n e^{-j\frac{2\pi}{N}kn}. \tag{2.20}$$

Therefore, we can assert that,

$$H_k = F_M^k H_l(z)z^{-l} \tag{2.21}$$

with F_M^k being the DFT matrix. The implementation is shown in Figure 2.10.

The output u_f of each filter from the DFT polyphasic filter bank is then given by,

$$u_f = \sum_{l=0}^{M-1} F_M^f H_l(z)\{X(z)z^{-l}\}_{(\downarrow M)}. \tag{2.22}$$

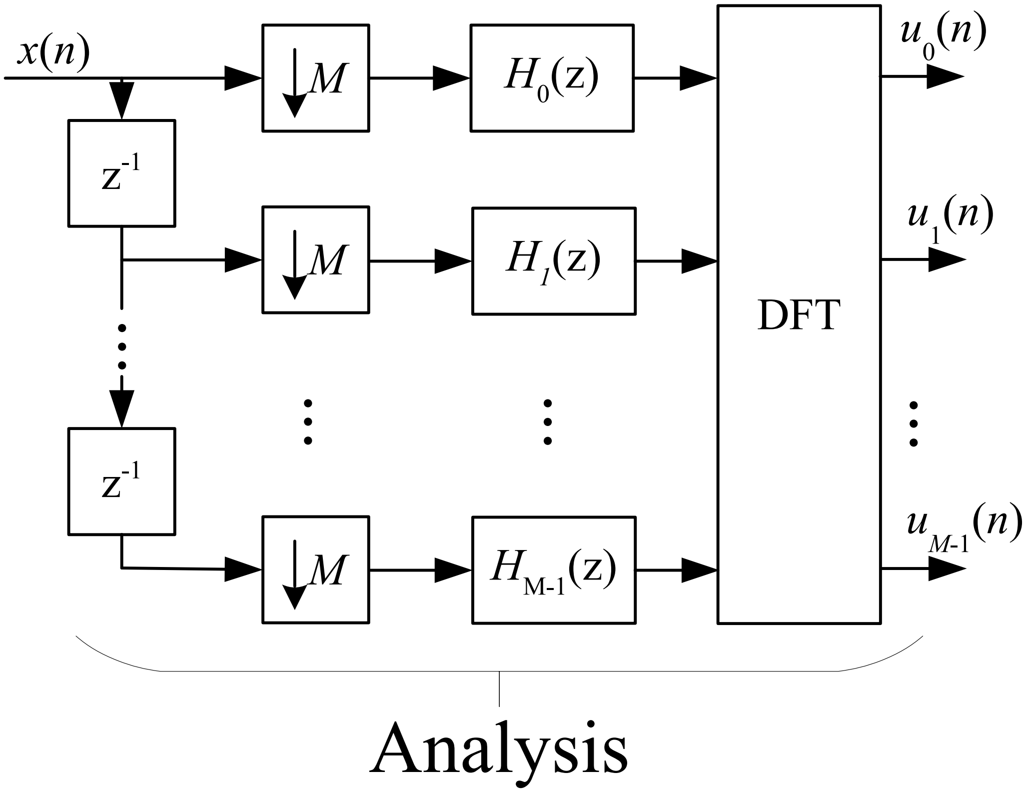

Figure 2.10: Implementation of the DFT filter bank.

The spectrum estimation $\hat{S}_{FB}$ obtained by using a DFT polyphasic filter bank is,

$$\hat{S}_{FB}(f) = |u_f|^2 = |\sum_{l=0}^{M-1} F_M^f H_l(z)\{X(z)z^{-l}\}_{(\downarrow M)}|^2. \tag{2.23}$$

2.1.4.2 Practical implementation

In the previous sub-section it was demonstrated an efficient implementation of a analysis filter bank using only a prototype filter in a polyphasic implementation together with a DFT, that can be employed efficiently by using a FFT.

For a practical implementation it is necessary to first chose a prototype filter. The selection of this filter should take into account some key characteristics. A good pass-band response for the passing band, a rapid decay and a exceptional good rejection band for a large bandwidth. As it is common for a filter bank in spectrum analysis to have a large number of filters, it is of critical importance to have a steady decay in frequency on the stop band to avoid frequency leakage. For illustration, it is plotted in Figure 2.11, using the same number of coefficients, the frequency response of a prototype filter by using some common window functions.

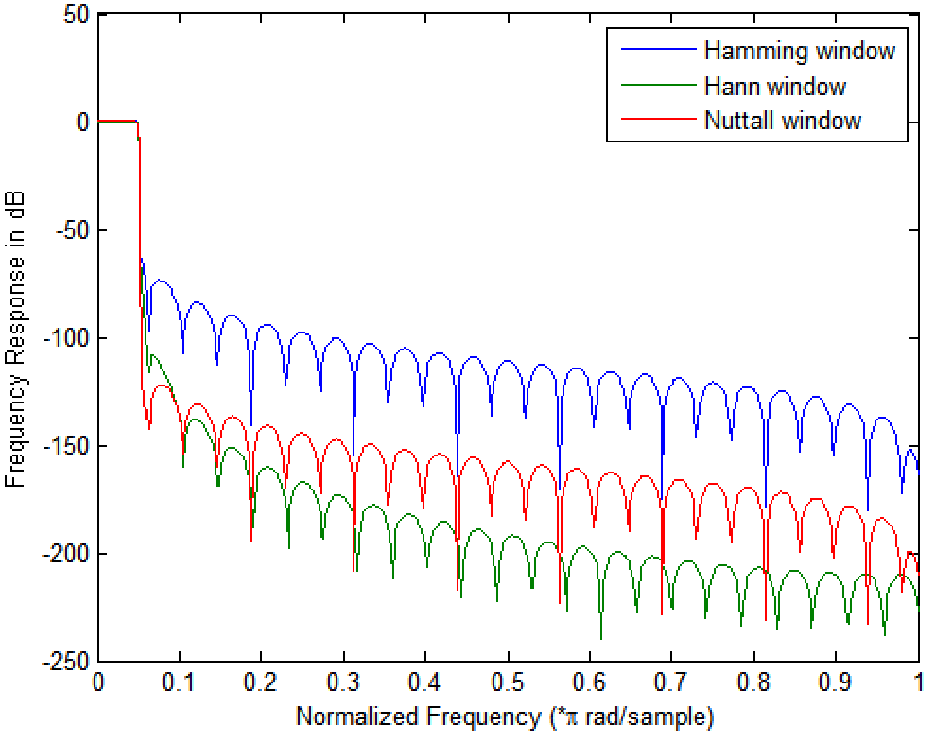

Figure 2.11: Evaluation of the frequency response of a prototype filter using three different window functions.

From the selected three functions, it can be determined that the best function in order to achieve a high attenuation outside the region of interest, of the prototype filter, its the Hann window.

Lets consider a DFT polyphase filter bank, that uses a Hann prototype filter with 10 thousand coefficients and a thousand filters. Each filter will have a bandwidth of one *per mille* of the analysed spectrum. In this situation the following frequency response from the DFT filter bank is illustrated in Figure 2.12.

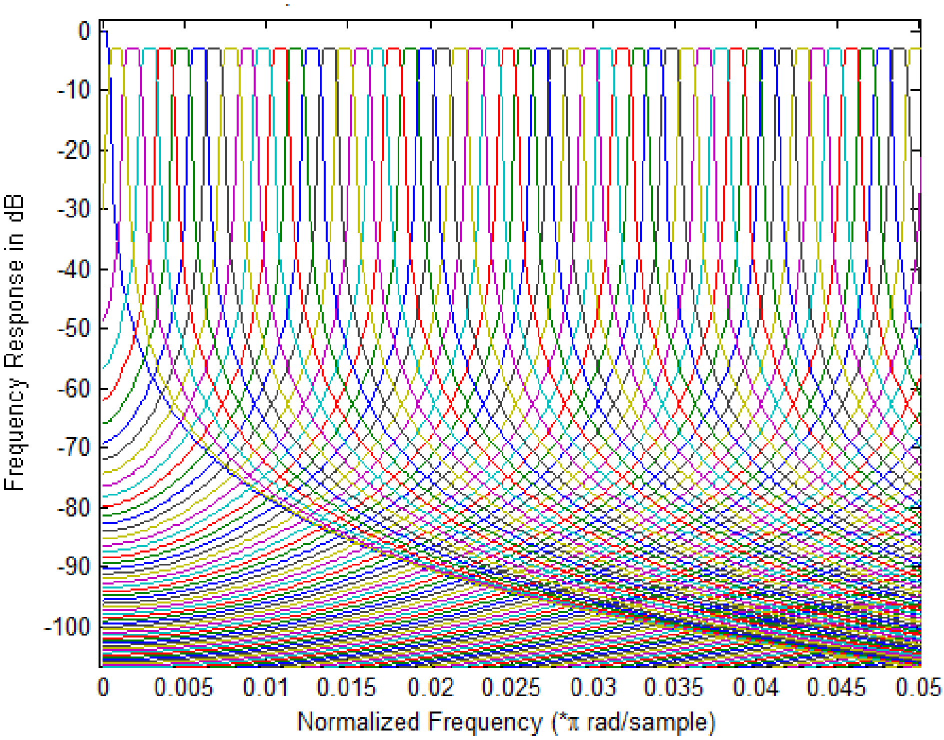

Figure 2.12: Frequency response of part of the DFT filter bank with $\frac{1}{5000}$ normalized frequency resolution.

It is visible that the original Hann prototype filter is replicated and translated in frequency for every filter central frequency of the filter bank.

2.1.5 Multitaper

2.1.5.1 Introduction

In 1982, Thomson [66] demonstrated that more than one tapering (also called window) function could be use for spectral analysis. He proposed a multitaper spectral analysis method, where the analysed data sequence is multiplied not by one taper, as in the periodogram spectral estimation, but by multiple data tapers. In the multitaper method this data tapers are a set of orthogonal sequences that form N estimations. This N estimations are then averaged to form the multitaper PSD estimation.

When using a traditional windowed periodogram, a large portion of the analysed signal is discarded due to the utilization of a single taper. This is due to the use of window functions that usually have zero-valued end-points. Increasing then the variance of the estimated spectrogram. Multitaper analysis tried to solve that problem by using multiple tapers.

To obtain a spectrum estimation using this method we first obtain the k eigencomponents:

$$\hat{S}_k(f) = |Y_k(f)|^2 = \left|\sum_{n=0}^{N-1} x(n)w_k(n)e^{-j2\pi fn}\right|^2 \tag{2.24}$$

Where $w_k(n)$, $k = 1, 2, ..., K$ are the K orthogonal taper functions. Usually two types of orthogonal taper functions are used, the Slepian sequences and sinusoidal tapers [67].

2.1.5.2 Slepian Sequences

In multitaper analysis, one of the most used taper functions are the Slepian sequences [68] also called Discrete Prolate Spheroidal Sequences (DPSS). They are defined by a K number of sequences, with a N number of weights and a W bandwidth parameter.

The selection of K is a compromise between spectral leakage and the variance of the estimation. The leakage gets worse as K increases and the variance decreases as K is incremented. The parameter W comes from the selection of K and as W increases the frequency resolution improves.

The first sequence of the Slepian functions has an eigenvalue of λ_0 that is very close to unity. Making the first taper the best in terms of spectral leakage for the chosen W.

The first $2NW - 1$ sequences also have eigenvalues that are close to unity, making $K = 2NW - 1$ a common selection [69]. The remaining sequences have increasingly worse spectral concentration proprieties and are only used for lower values of W. As an example, the Slepian sequences $w_k(n)$ with $NW = 2$ and $N = 100$ are plotted in Figure 2.13 and their DFT is in Figure 2.14.

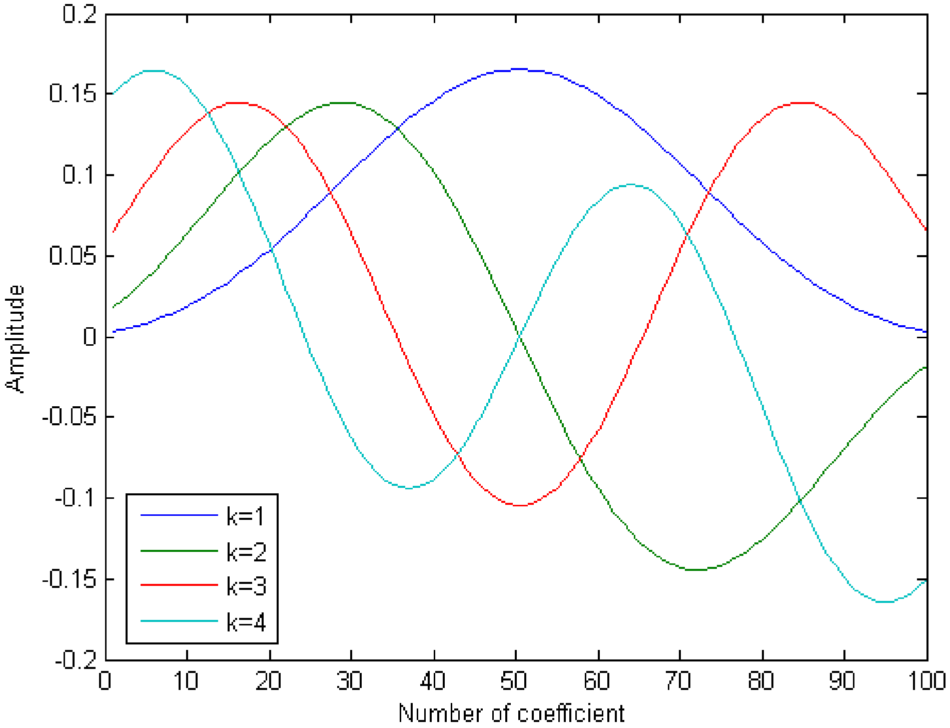

Figure 2.13: Tapers of the first four Slepian sequences with $NW = 2$.

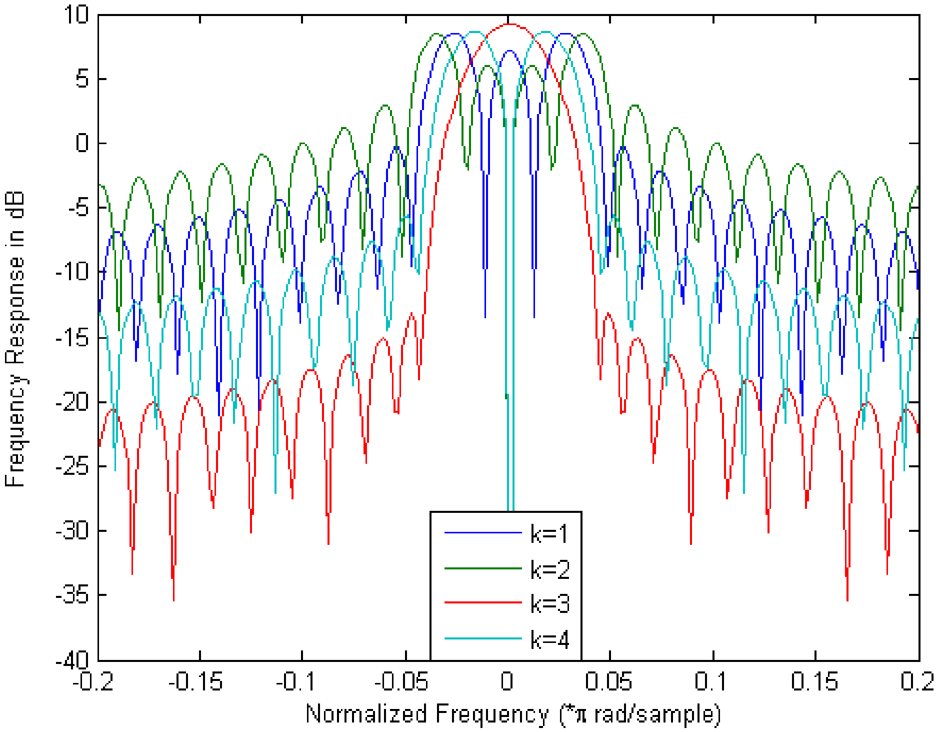

Figure 2.14: Frequency response for the first four Slepian sequences with $NW = 2$.

It is then possible to define K as a function of NW, in literature NW is sometimes refereed as half-bandwidth resolution. The number of data samples and NW are then used to create the Slepian sequences. For $K = 2NW - 1$ the lower limit of NW, by the multitaper definition, is given by $NW = 1.5$ as it is the lower amount of half-bandwidth resolution that still has at least 2 tapper sequences. The maximum value of NW is subjective and in literature is usually defined as $NW = 16$ [70]. This maximum value is defined as for high NW values the frequency resolution is lost and computational complexity, as more tappers are used in the calculation, is increased.

2.1.5.3 Combination of the individual tapered PSDs

As described in Section 2.1.5.2, for $K \leq 2NW - 1$ the eigenvalues of each tapper sequence are very close to the unity. In this situation the multitaper spectrum can be given by the averaging the multitaper estimations.

$$S_{MT}(f) = \frac{1}{K} \sum_{k=0}^{K-1} \hat{S}_k(f) \tag{2.25}$$

An alternative is to consider an weighed sum of the individual estimations, this is of critical importance for $K \gg 2NW - 1$ [71]. The weight of each sequence k is the given by its eigenvalue λ_k.

$$S_{MT}(f) = \frac{\sum_{k=0}^{K-1} \lambda_k^2 \hat{S}_k(f)}{\sum_{k=0}^{K-1} \lambda_k^2} \tag{2.26}$$

It is also possible to implement adaptive weights in order to allow a selective leakage suppression [72],

$$S_{MT}(f) = \frac{\sum_{k=0}^{K-1} b_k^2 \lambda_k^2 \hat{S}_k(f)}{\sum_{k=0}^{K-1} b_k^2 \lambda_k^2} \tag{2.27}$$

where b_k is the adaptive weight attributed for each tapper sequence [73, 74].

2.1.5.4 Multitaper implementation vs Polyphasic Filter Bank

Frequency response comparison For comparison, both multitaper and polyphasic filter bank were implemented in Matlab with the following conditions. Both methods use a input of 1000 samples and have an output of 20 frequency bins. The prototype filter of the filter bank has 1000 coefficients ans is generated using an Hann function. For a better computational performance the filter bank has a polyphasic implementation. The multitaper implementation is going to use a value of $NW = 25$ in order to have the same frequency response of the filter bank.

The results for the filter bank implementation are shown in Figure 2.15 and the multitaper implementation is shown in Figure 2.16.

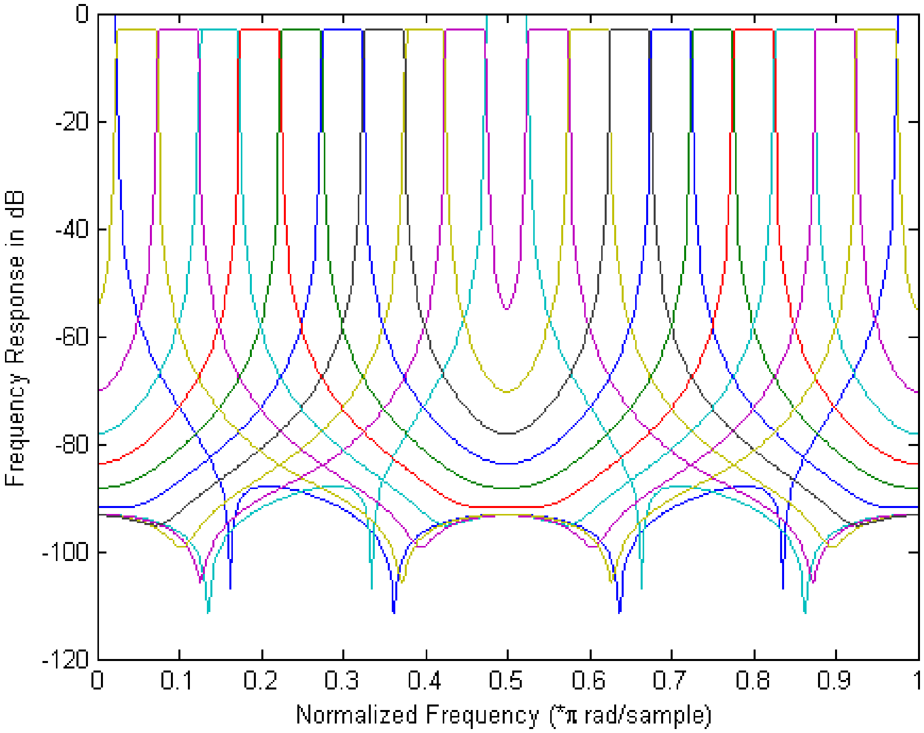

Figure 2.15: Frequency response of the filter bank implementation.

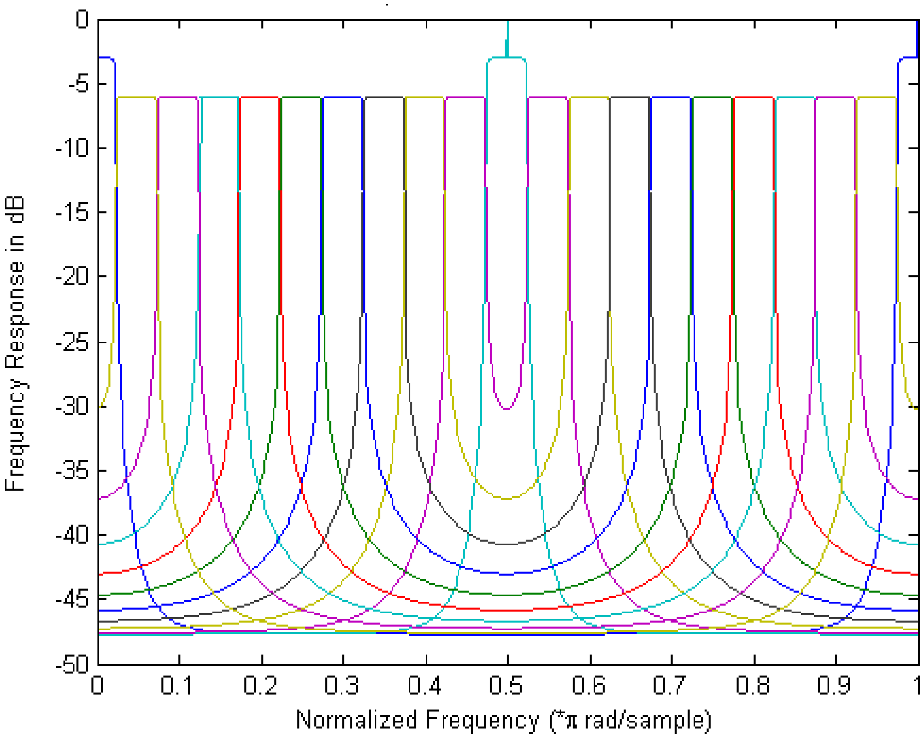

Figure 2.16: Frequency response of the multitaper implementation.

It is visible that the multitaper implementation does not decays at the same rate as the filter bank implementation does. It can also be observed that all the filters outputs shown an attenuation floor of -48 dB a value much lower than what is achieved with the filter bank implementation. Another important aspect in the filter bank method is that it is possible to increment the number of coefficients or change the prototype filter, such thing is not possible in the multitaper implementation. Let us take a closer look for a single filter frequency response for each method in order to directly compare they behavior,

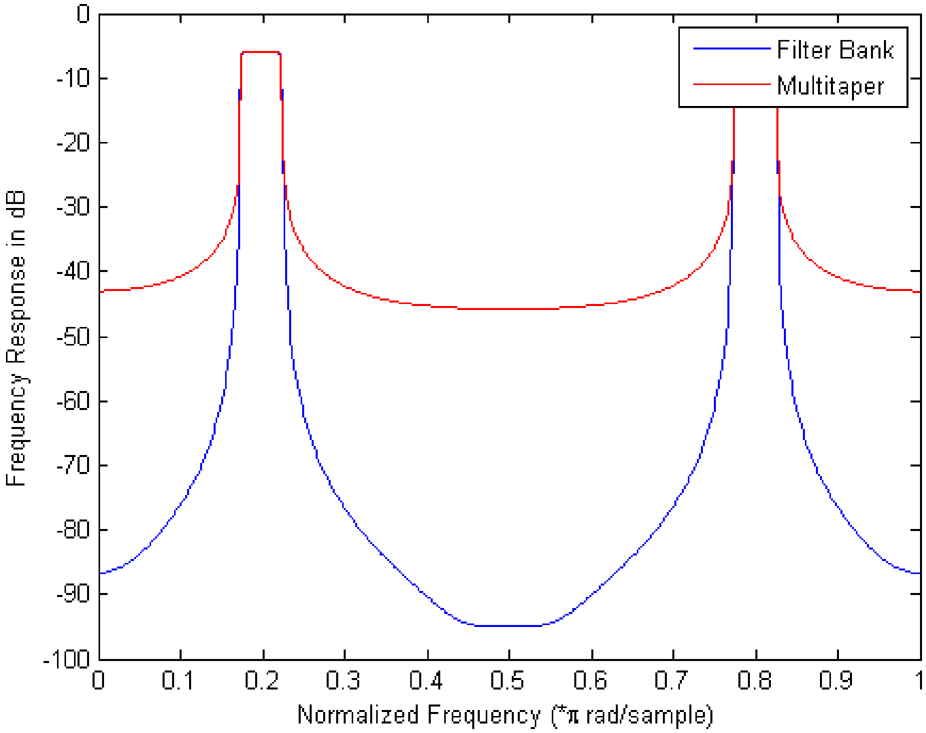

Figure 2.17: Frequency response for the 5th filter both for the filter bank and multitaper.

as it is visible in Figure 2.17 the filter bank method has a faster decay outside the passband frequency and also shows a higher rejection ratio than the multitaper implementation. This allows for a lower amount of frequency leakage.

2.1.5.5 Computational performance comparison

The performance comparison also shows very clear results. For the proposed conditions, with Matlab 2014a running in a Intel i7-2670QM processor the results are detailed in Table 2.1.

FFT	Polyphasic Filter Bank	Multitaper
0.3 ms	0.643ms	4.2ms

Table 2.1: Time needed for each spectrum sensing method.

The polyphasic filter bank shows a better computational performance against multitaper with also an improved frequency response. The lower computational time needed by the filter bank can be explained by its polyphasic implementation. This methodology reduces the time needed for signal filtering. In the other hand, the multitaper uses K windows each with the same size of the input data vector. Due to this, the multitaper has an increased complexity and takes more time to calculate. These results show that the polyphasic filter bank would have a more computational efficient implementation than the multitaper method. Thus, the following implementations of spectral analysis in this thesis will focus on the method of polyphasic filter bank

2.2 Signal detection

With every spectrum analysis measurement, there is the need to decide which frequency bands are occupied or which are free to use. The classic assumption model is to consider that the analysed signal in a given band can be in one of two states. This binary hypothesis can be formulated in the following way,

$$\begin{aligned} \mathcal{H}_0 &: y(n) = w(n) \\ \mathcal{H}_1 &: y(n) = s(n) + w(n) \end{aligned} \tag{2.28}$$

with $y(n)$ being the band-limited signal, $s(n)$ the received signal coming from a user and $w(n)$ the noise floor. By analyzing the spectrum, we need to be able to decide what specific frequencies represent noise or signal. This decision is made by assuming a threshold for each frequency band at the output of the spectrum analysis block. Therefore, a binary decision is taken by comparing the energy estimates with the threshold, as shown in Figure 2.18.

The most common method for detecting the existence of a signal, in a given signal-to-noise ratio, is the energy detection method. For this method, the acquired signal is constantly evaluated against a given threshold. This threshold is either a fixed value or it is adaptive. It is usually defined with three parameters in mind:

- **Probability of detection** (P_D), that is the probability of detecting a signal that is indeed present;
- **False alarm probability** (P_{FA}), that is the probability of detecting a signal where only noise exists;
- **Probability of miss detection** (P_{MD}), which is the probability of missing the detection of a signal.

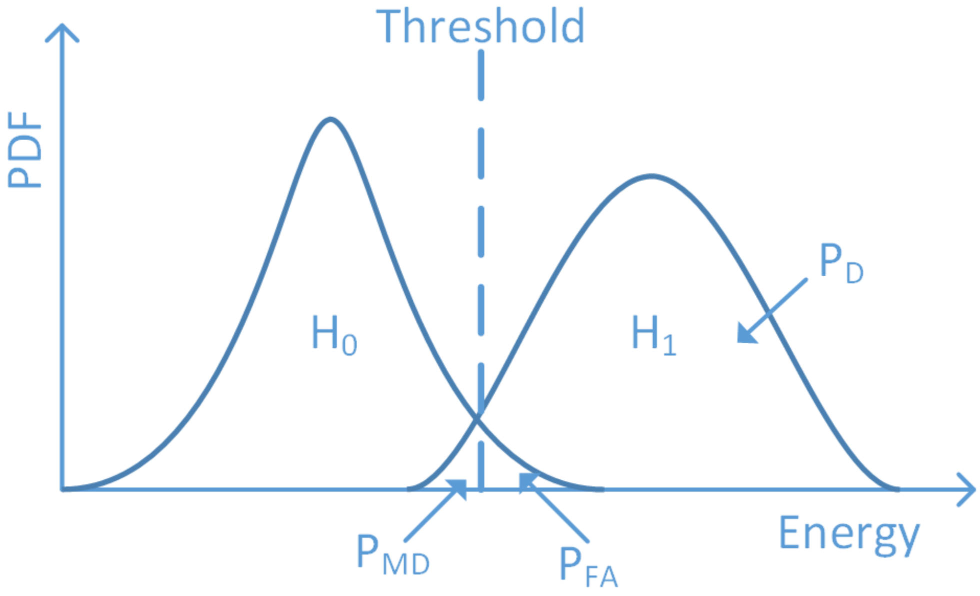

Figure 2.18: Probability diagram for the signal detection model.

The most common application of the energy detection method, with an adaptive threshold, is the CFAR detector. The CFAR method [75], proposes a dynamic threshold value based on a fixed probability of false alarm. Usually in radar detection the CFAR is achieved by continuously analyzing a fixed number of samples and compare them to their neighbor cells, also known as training cells [76]. These neighbor cells are then used as a reference for the noise floor that defines the threshold for CFAR detection [77].

This classical application has some faults and can not be directly applied to maintaining a constant false alarm rate in a spectrum sensing unit. For instance, if a signal with a flat-top frequency response is constantly transmitting the same energy level, then this value could be associated to both noise or to a constant power wideband signal.

In order to have a true constant false alarm rate, the noise floor Probability Distribution Function (PDF) must be known. As it is expected that this value does not remain constant in time, due to all the variable sources of RF noise that can affect the device, it is then important to frequently update the PDF estimation of the noise floor. In order to do so, one solution is to constantly evaluate the output from our spectrum analysis algorithms to obtain the noise floor mean power and variance to then create a threshold that will allow to achieve the defined false alarm rate.

2.3 Noise Model

There are key disadvantages in the fixed noise model estimation. In fixed noise probability distributions based detection, as previously discussed, the signal can have a similar distribution to the noise making them indistinguishable from one another. In the eigenvalue analysis, the detection is made based on the frequency analysis ratio distribution, making it impossible to differentiate a signal, with a flat top frequency response, from noise floor. A dynamical noise model estimation does not suffer from those limitations.

The practical RF noise floor behavior is dynamic both in energy and frequency response. This creates the need for a dynamic noise floor estimation that can be evaluated by calculating the threshold used to classify noise and signal [78]. However, the noise floor estimation will not give a perfectly accurate value and estimation error is to be expected. These uncertainties can be quantified by a position on the SNR wall where bellow that, the detector is unable to correctly determine the presence or absence of signals, even for an infinite observation time [79]. In spectrum sensing, the goal is to meet a given constraint of probability of detection and false alarm, even in low SNR scenarios. The noise uncertainty problem is usually attributed to the following causes:

- Temperature variation;
- Change in the Low Noise Amplifier (LNA) gain caused by thermal fluctuations;
- Calibration errors;
- Presence of interferes.

Noise power estimation with enough samples can be used to overcome constant uncertainties like calibration errors and slow variation phenomenons like thermal changes. In case of a shared RF medium the solution is usually to have "quiet periods" in the used protocol, allowing intervals where all the network cease transmission and the radio can observe the noise floor [80].

In order to obtain a noise power estimation, the received measured power from a determined bandwidth of the spectrum is sampled. Let $y(n)$ be this band limited signal, at instant i the received power ν, over an observation window of L samples, can be defined by,

$$\nu(i) = \frac{1}{L} \sum_{n=i-L}^{i} |y(n)|^2. \tag{2.29}$$

Assuming that the received signal has a Gaussian distribution, then ν will have a chi squared distribution of $2L$ order and by the central limit theorem, for a large value of L, it can be consider a Gaussian random variable [81]. In this case we have,

$$\nu(y) \sim \begin{cases} \mathcal{N}(\sigma_0^2, \frac{\sigma_0^4}{L}), & H_0 \\ \mathcal{N}(\sigma_1^2, \frac{\sigma_1^4}{L}), & H_1 \end{cases} \tag{2.30}$$

where σ_0^2 is the noise variance and σ_1^2 is the sum of both the signal and noise variance. Assuming a constant noise variance the SNR could thus be calculated by $SNR = \frac{\sigma_1^2}{\sigma_0^2} - 1$. In a practical implementation the noise-floor will not be constant, due to this uncertainty its value can only be estimated. Let us assume an unbiased asymptotical noise variance estimator $\hat{\sigma}^2$. Using the observation window from Equation 2.29 this noise estimation will then follow a Gaussian distribution given by $\hat{\sigma}^2 \sim \mathcal{N}(\sigma_0^2, \frac{\sigma_0^4}{N})$. The noise floor estimation can then be used to determine a threshold γ for signal detection. The probability of false alarm (P_{Fa}) and the probability of detection (P_D) of this threshold can be calculated with the tail probabilities of the Gaussian distribution given by,

$$P_{Fa} = Q\left(\frac{\gamma - \sigma_0}{\mathrm{var}(\hat{\sigma}^2)}\right) \tag{2.31}$$

$$P_D = Q\left(Q^{-1}(P_{FA}) - SNR\right) \tag{2.32}$$

Considering an energy detection test where the noise power σ_o^2 is estimated by the$\hat{\sigma}^2$, an arbitrary desired pair of probability of false alarm an detection $(P_{Fa}^{DES}, P_D^{DES})$ can always be reached by increasing the observation time, by increasing the collected number of samples N, for all possible values of SNR, if and only if the variance of the noise power estimator, $\mathrm{var}(\hat{\sigma}^2)$ converge to 0 for $L \to \infty$. On the other hand if $\mathrm{var}(\hat{\sigma}^2)$ converges to a constant value, different of zero, for $L \to \infty$, then there is a minimum SNR that is called SNR wall, under which it is impossible to achieve the desired $(P_{Fa}^{DES}, P_D^{DES})$ pair [82]. In this situation the minimum SNR for $L \to \infty$ converges to,

$$SNR_{min}^{(\infty)} = \frac{1 - \delta\sqrt{\phi}}{1 - \alpha\sqrt{\phi}}. \tag{2.33}$$

As it is assumed that the noise has Gaussian distribution we define $\phi = var(\hat{\sigma}^2/\sigma_0^2)$, $\alpha = Q^{-1}(P_{Fa}^{DES})$ and $\delta = Q^{-1}(P_D^{DES})$, where $Q(x)$ is the tail probability of the standard normal distribution.

In the presence of a non ideal estimation of the noise power, the SNR wall phenomenon does not arise if $\hat{\sigma}^2$ is a consistent, with L, estimator of the noise power. Due to this, it is recommended that dynamical noise floor estimation uses as many samples as possible.

There are two methods to obtain an adaptive estimation for the noise floor. The first method based on “quiet periods” estimates the noise floor for each frequency, is applied if the frequency bands and are expected to have a duty cycle of usage. When the channel is not in use, the power value can be used to evaluate the noise floor and get an updated estimation. The second method uses information from adjacent frequency bands to estimate the noise floor, and is used if there are frequency bands that are constantly being occupied, as happens in FM broadcast. An example of the power spectrum, calculated with a filterbank, of an acquisition of the FM broadcast spectrum in a typical urban area is shown in Figure 2.19 .

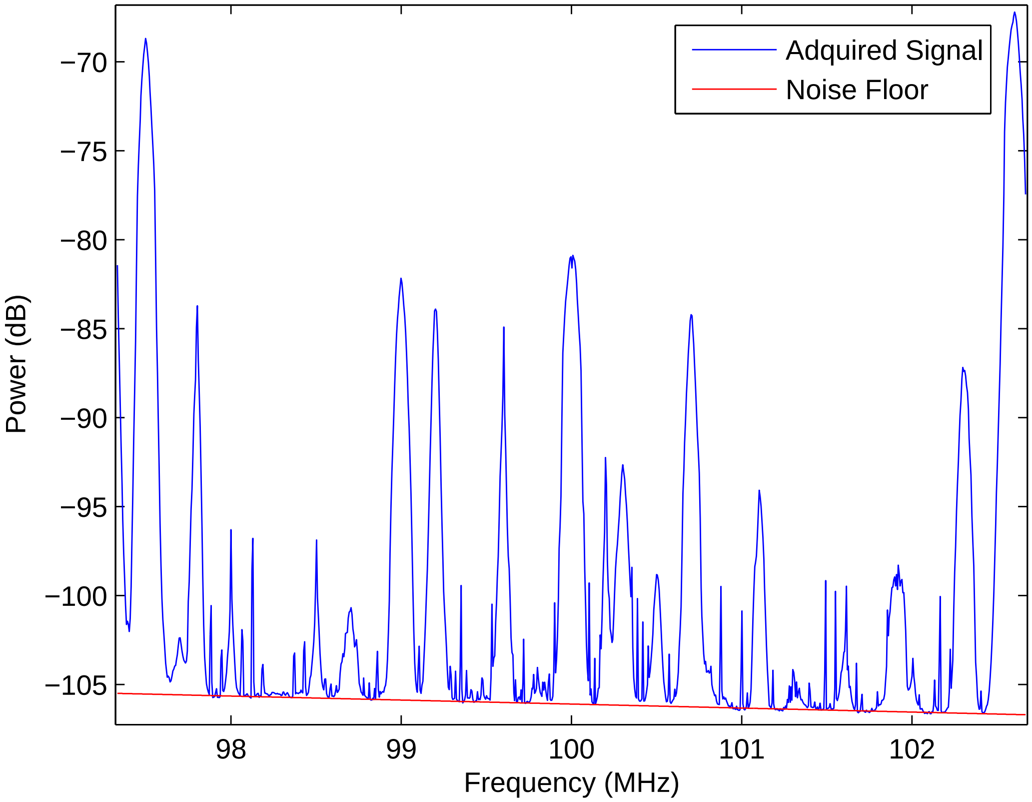

Figure 2.19: The power spectrum of part of the FM broadcast spectrum where the broadcast stations are visible as well as the noise floor power in between.

The non-occupied channels might then be used to estimate the noise floor, as is visible in Figure 2.19. This of course requires that the system is precisely equalized in order to obtain the same noise floor behavior for all the analysed frequency spectrum and may be unsuitable in presence of noise with non-uniform frequency response (colored noise).

In shared frequency bands, where multiple users are present, it is expected to exist different sources of signal that depending on the distance to the spectrum unit, will be received at different energy levels. This fact occurs in various technologies, as Wi-Fi, LTE and so on, where the RF bands are shared between all users. When a large amount of users occupies actively the allocated RF band, then only small sporadic intervals of time in which the channel is not occupied. This relatively small period where only noise floor is present can make the task of estimating its level extremely complex.

It is common that RF protocols have a short period of time where there are no transmissions on the shared medium. For the LTE protocol, in TDD configuration there is every radio frame of 10 ms a special frame. This special frame is segmented in three periods, first the downlink pilot time slot, then a guard period than the uplink pilot time slot. There are no transmissions in the Guard Period, and the smallest duration for this segment is of approximately 71 μs [83] .

In the 802.11 standard, the Distributed Coordination Function (DCF) determines that it is expected to always exist a waiting period where a station needs to check the medium before transmitting data. This period, where the user needs to sense the channel before using it, is called the DCF Interframe Space (DIFS). Only after the medium is idle during the DIFS interval the station is allowed to transmit [84]. Even if only one user is using the channel to communicate with the access point, there still is a minimum specified time-slot that is not occupied called Short Inter Frame Space (SIFS) interval. The SIFS interval defines the minimum time-slot between data fragments or immediate response from the medium user (e.g. data acknowledge) when the medium is not being occupied.

The worst case scenario is for 802.11n where the spectrum sensing unit needs to be able to estimate the noise floor using SIFS intervals of $10\,\mu$s or DIFS intervals of $34\,\mu$s.

One method that can be used in order to estimate the noise floor, that does not require any *a priori* knowledge, is to acquire enough samples, to allow to do a precise estimation based on observed data, of all the acquired unobservable underlying processes probability density function. This processes can be divided in two groups:

- **Noise floor** (H_0), when no user is present on the allocated RF band and all that is observable is the noise produced by the environment and by the RF front-end itself.
- **User occupation** (H_1), when a given user transmits a signal with a given and approximately constant power.

The probability distribution function of an acquired time interval signal will then be the sum of all the processes probability density.

If an energy estimator, that averages a large number of samples, is used then by the central limit theorem [85], the histogram of the analysed process converges toward a Gaussian distribution. The result, in a spectrum sensing scenario, will then be the sum of all the Gaussian components, giving rise to a PDF that follows a GMM. The lowest mean component will then be the noise floor and the highest value components will be different users transmitting at different powers or at different distances.

2.4 Performance comparison of spectrum sensing techniques

A spectrum sensing system is composed by three blocks: spectrum analysis, signal detection and noise model estimation. All these components are chosen and combined in order to achieve the best implementation for a given application. Due to this, it is of key importance to establish a performance criterion between spectrum sensing implementations in order to be able to compare them. While there are many aspects that could be used to compare the performance of spectrum sensing methods, there is a method that can analyze the performance over a wide range of conditions. This method is called the ROC curve.

The ROC curve is a standard comparison method in spectrum sensing systems. The graph is plotted with the P_{Fa} in the horizontal axis and the P_D in the vertical axis. The curve points are determined by the binary classification of the analysed data. The data samples are classified as either being part of the noise floor or signal. The better the accuracy of this classification the closest the ROC curve will be to the point of $P_D = 1$ and $P_{Fa} = 0$ as seen in Figure 2.20.

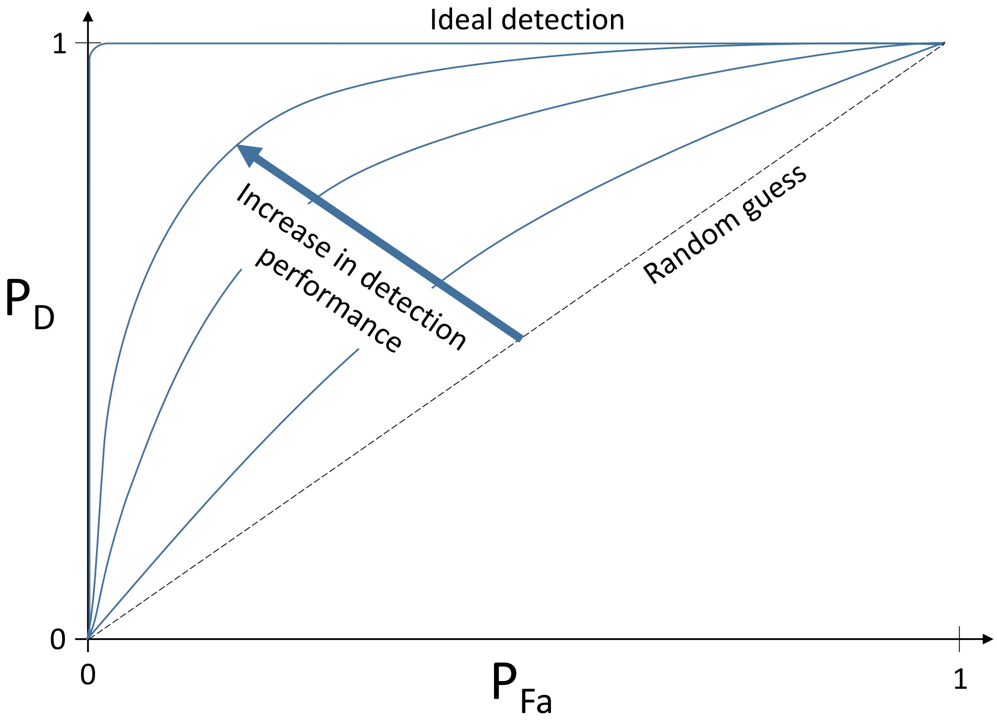

Figure 2.20: Performance analysis in the ROC space.

In order to obtain an empirical ROC curve for a given spectrum sensing method, a data segment composed by both signal and noise data must be analysed. In this data there must be *a priori* knowledge of which point belongs to each state (signal or noise). The data is then classified using a varying threshold. The lowest and highest values that can be attributed to the threshold are given by data segment boundary values. By varying the threshold along these values, it is possible obtain the empirical classification of the analysed data. For each threshold the binary results are then compared to the known attributions of each data point (signal or noise) in order to obtain the P_{Fa} and P_D. The final ROC curve will then be a two dimensional plot where each (P_{Fa}, P_D) point is given by a different threshold. Using a changeless threshold vector, this process can be done as many times as needed in order to obtain a closer approximation to the theoretic ROC curve. This method is independent from any threshold calculation technique.

If the goal is to evaluate different methods of threshold calculation an identical empirical ROC curve determination can be done. The difference is that in this situation there is not a varying threshold, the threshold is calculated for each data segment. In this empirical determination each ROC curve point is not determined by a different threshold, but is obtained for each data segment. This is of critical importance for comparing different noise floor estimation techniques and threshold calculation methods usually for CFAR.

The simplest comparative method for the performance of spectrum sensing methods is then to compare the ROC curves obtained from each one. Usually the closest curve to the point $P_D = 1$ and $P_{Fa} = 0$ shown then the best accuracy for detection with the lowest percentage of false alarms. If the plotted curves are close to each other than visual comparison may not be possible. In those situations, is normally used the Area Under the Curve (AUC) parameter.

The AUC is obtained by calculating the integral of the ROC curve. An estimation of it can be obtained by numerical integration of the empirically obtained ROC curve $f(x)$. Assuming an uniformly spaced grid of N points with a a grid spacing of h, the AUC can be obtained by,

$$\widehat{AUC} = \frac{h}{2} \sum_{k=0}^{N-1} (f(x_{k+1}) + f(x_k)) \tag{2.34}$$

There is an expected empirical error due to the effect of the trapezium rule, more evidently by splitting the range from zero to one into a number of sub-intervals, that approximate the curve, and summing the areas of the trapezium.

Chapter 3

GMM for Spectrum Sensing

The previously discussed signal detection methods, as the CFAR, provide a binary decision concerning channel occupation. The channel may be, at a given moment, free or occupied. The decision is based on the knowledge of the noise floor statistical properties, as its probability distribution function. The noise floor proprieties are then estimated to determine the detection threshold.

For further information about the frequency channels usage, different signal analysis methods need to be explored. In addition to the binary decision of occupation there is other relevant information about the channel usage that could help in collaborative spectrum sharing as well as for the radio regulation agencies that ensure the correct use of the spectrum. Some relevant information could be: the number of users sharing the channel, their occupation in time-slots and the evolution of the noise floor power. As far as we know, there are no methods capable of obtaining this additional information without the demodulation of the received signals. A solution that would allow to classify the received signals through the spectrum without the without the burden of having to demodulate every single signal would be of great value. This could be done by tracking the received power of the sensed signals. This solution does not need to demodulate the signal, having then the security of obtaining the information trough anonymous data. The obtained usage characteristics of the spectrum are useful for regulatory agencies to detect non-authorized transmissions or as inputs to machine learning algorithms incorporated in collaborative spectrum sensing systems.

One possible method to obtain these channel utilization characteristics can be done based on the EM algorithm, as proposed by the author in [86]. The EM algorithm is usually employed to estimate unknown parameters of an observed data set with a known distribution function. One of the most common estimation problems is the estimation of the mean and variance of a data that is a mixture of several signals and noise [87]. For this reason, the EM has typically been associated with reconstruction and clustering of data, with emphasis on image processing [88],[89].

More recently, the application of EM has been used in spectrum sensing. In [90] spectrum measurement data acquired by a spectrum analyzer are analysed using the EM algorithm. In this article the authors state that the transmitted wireless signals follow a Rayleigh distribution while noise follows a Gaussian distribution. This statement allows the use of a Rayleigh-Gaussian mixture as a model for the data analysed in the EM algorithm. In [91] EM is used for Spectrum Sensing in a multi-antenna and multi-user scenario. In the article it is assumed that the noise and signal are modeled by Gaussian distributions. The discrete

Fourier Transform of the data is then analysed by the EM algorithm using a complex GMM [92].

The assumption that the noise fits a Gaussian model may not always be the best approach, as it may not be adequate to model atmospheric noise, man-made RF and other sources of ultra-wideband interference [93],[94]. The same can be described for a Rayleigh fit on the transmitted RF signals, that may not be always the best approximation for all possible cases [95].

The issue of determining the distribution that models both signal and noise can be solved by the central-limit theorem. This is done by estimating the energy of the received data, from the spectrum sensing unit, using a moving average. For a high order average the data distribution will then converge to a Gaussian distribution. In this situation both signal and noise can the be approximately model by a GMM.

3.1 Analysis of spectrum occupation as a GMM

3.1.1 Signal Model for a Shared Spectrum Environment

Consider a spectrum sensing front-end that is constantly analyzing the RF spectrum. The sensed spectrum is divided in multiple channels, where each channel can be either vacant (only noise floor is present) or occupied by one of U possible users. It is assumed that each user will be sensed by the RF front-end with an unique power level. This is due to the path between each transmitting user and the sensing front-end being unique.

At a particular instance of time n, the received signal will then from one of the $K-1$ users or, if no one is transmitting, the received signal will be the background noise floor. This scenario is modeled by the following hypothesis:

$$\begin{aligned} H_o : x(n) &= w(n) \\ H_k : x(n) &= s_k(n) + w(n) \end{aligned} \tag{3.1}$$

where $x(n)$ is the discrete received time signal in the front-end, s_k denotes the signal transmitted by the user $k = 1, 2, ..., K-1$ and $w(n)$ the additive zero-mean white Gaussian noise. A sensing interval, encompassing N samples, will be a sequence of received user signals, represented by H_k, and also noise floor, described by H_o. Let $\mathbf{x}$ denote the received signal vector for an interval of N samples. This vector is given by the concatenation of data from a set of H_0 and H_k states. The vector $\mathbf{x}$ contains a mixture of at most $K-1$ transmitted users signals and the noise floor. As we assume that each sensed user has a unique power level, an energy estimation analysis of the $\mathbf{x}$ data vector will be able to differentiate the different users of the spectrum.

3.1.2 Signal Energy Estimation

In order to analyze the occupation, the spectrum can be divided into individual frequency bands. This spectrum division can be performed, for example, by a band-pass filter bank, with the necessary bandwidth for the required specifications. For each individual band, the filtered signal can be analysed to detect occupation. On the other hand, each k user of the shared medium will transmit different data at a different power level. Then, to characterize the energy in the channel, the processing steps illustrated in Figure 3.1 are proposed. The input x is the acquired complex signal with component in phase (x_I) and quadrature (x_Q). Each component is assumed to be an approximate Gaussian distribution with zero mean. The complex absolute square of the signal is calculated in order to obtain its instantaneous energy. As the data is assumed to follow a Gaussian distribution, squaring it gives origin to a Chi-Square distribution. The squared data is then filtered with a moving average that, as mentioned previously, for a high order L gives arise to a approximate Gaussian distribution [96]. Finally, the smoothed energy estimation is converted to decibels.

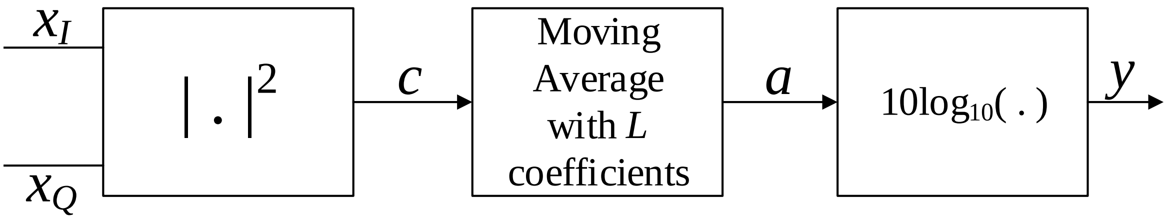

Figure 3.1: Functional diagram of the used energy estimator.

Considering the model described in Equation 3.1 the instantaneous energy estimation can correspond to a particular user or noise. The probability density function of the output y can be modeled as a GMM of K Gaussian distributions corresponding to $K-1$ active users and the noise floor. Each Gaussian has an unknown mean, which corresponds to its received power, however the variance depends on the order L of the moving average as will be proven latter.

3.1.3 Complex Absolute Square

For convenience of calculation, let us assume the front-end input as zero-mean Gaussian complex data, then the absolute square of the input is given by the sum of the squares of the phase and quadrature part of the signal.

$$c = |x|^2 = \left(\sqrt{x_I^2 + x_Q^2}\right)^2 = x_I^2 + x_Q^2 \tag{3.2}$$

By definition the Chi-Squared distribution is the result of squaring a standard normal random variable [97]. So, if $x \sim \mathcal{N}(0, \sigma^2)$, $x^2 \sim \sigma^2\chi_1^2$, where χ_1^2 is the Chi-Squared distribution with 1 degree of freedom. The mean and the variance of Chi-Squared are $\mathrm{E}[\chi_1^2] = 1$ and $\mathrm{Var}[\chi_1^2] = 2$, respectively. The mean of the squared signal is given by $\mathrm{E}[x^2] = \sigma^2$ and the variance by $\mathrm{Var}[x^2] = 2\sigma^4$ [98]. By assuming that the two components of the complex value are normally distributed independent variables $x_I, x_Q \sim \mathcal{N}(0, \frac{1}{2}\sigma_x^2)$, i.e. both with zero mean and equal variances. Then, the square of the quadrature and phase components of the signal will follow the Chi-Squared distribution $x_I^2, x_Q^2 \sim \chi_1^2(\frac{1}{2}\sigma_x^2, \frac{1}{2}\sigma_x^4)$ with the mean and variance calculated as explained before.

The output of the first block, c, is the sum of the squared phase and quadrature components. Therefore, the c signal is the sum of two independent components which have identical Chi-Squared distributions. The distribution of the signal at the output of the first block of the Figure 3.1 is also a Chi-Squared distribution $c \sim \chi_1^2(\sigma_x^2, \sigma_x^4)$. Therefore, the mean is equal to the variance of the input signal, while the variance is the square of the input variance.

3.1.4 Moving Average

By averaging the signal with a high L order filter the central-limit theorem is applicable and the filter output distribution can be modeled by a Gaussian distribution [96]. Assuming that the input corresponds to L independently repeated measurements of the same user transmission process, i. e., the data points are Independent and Identically Distributed (IID), then the expected value of the sample mean, calculated in the moving average, is given by [99],

$$\begin{aligned} \mathrm{E}[a(n)] &= \frac{1}{L}\mathrm{E}\left[\sum_{n=0}^{L-1} c(n)\right] \\ &= \sigma_x^2. \end{aligned} \tag{3.3}$$

Thus the expected value is the variance of the original complex input signal x.

The variance given by the moving average is given by [99],

$$\begin{aligned} \mathrm{Var}[a(n)] &= \frac{1}{L^2}\sum_{n=0}^{L-1} \mathrm{Var}[c(n)] \\ &= \frac{\sigma_x^4}{L} \end{aligned} \tag{3.4}$$

thus allowing to reduce the variance of the input signal by a factor L.

Finally, we get the distribution for the moving average filter as the following normal distribution, $a \sim \mathcal{N}(\sigma_x^2, \frac{\sigma_x^4}{L})$.

3.1.5 Analyzing the output distribution of the energy estimator

The estimated energy value, from the moving average is converted to decibels. The distribution function of this new variable can be computed but the mean and the variance can only be approximated. For this purpose a Taylor series approximation of the energy estimator distribution function is proposed.

3.1.5.1 The PDF of the output

As shown before, the moving average filter output signal follows a normal distribution given by,

$$f(a) = \frac{1}{\sigma\sqrt{2\pi}} \exp\left(-\frac{(a-\mu)^2}{2\sigma^2}\right) \tag{3.5}$$

where the mean is μ and variance is σ^2. Then applying the following logarithmic transformation we obtain,

$$g(a) = y = 10\log_{10}(a) \Leftrightarrow a = 10^{\frac{y}{10}}. \tag{3.6}$$

The distribution function of the estimated energy output, y, is computed as $f(y) = f(a(y))|\frac{da}{dy}|$ [100]. The two terms of this equation are the following:

$$\begin{cases} f(a(y)) = \frac{1}{\sigma\sqrt{2\pi}} \exp\left(-\frac{(a-\mu)^2}{2\sigma^2}\right) \\ \\ \frac{da}{dy} = \ln(10)10^{\frac{y}{10}-1} \end{cases} \tag{3.7}$$

The probability distribution function of the output of the energy estimation system is then,

$$f(y) = f(a(y))\left|\frac{da}{dy}\right| = \ln(10)10^{\frac{y}{10}-1}\frac{1}{\sigma\sqrt{2\pi}}\exp\left(-\frac{(10^{\frac{y}{10}}-\mu)^2}{2\sigma^2}\right) \tag{3.8}$$

this distribution function will be analysed next.

3.1.5.2 Mean and Variance Estimates

The random variable a has a Gaussian distribution with a positive mean and, for a high-order (L) filter, the a values will never be zero. Note that the variance of a reduces with L, but the mean stays constant. So the concentration of a around its mean is proportional to the order L of the moving average. This allows to replace the logarithm in a short interval by a linear approximation with a small error.

To evaluate the approximation, we consider the signal with mean 0.5 (i.e, ≈ -3dB) and define two different ratios between the signal mean and variance. Figure 3.2 shows the results for two different ratios, 50 and 1000.

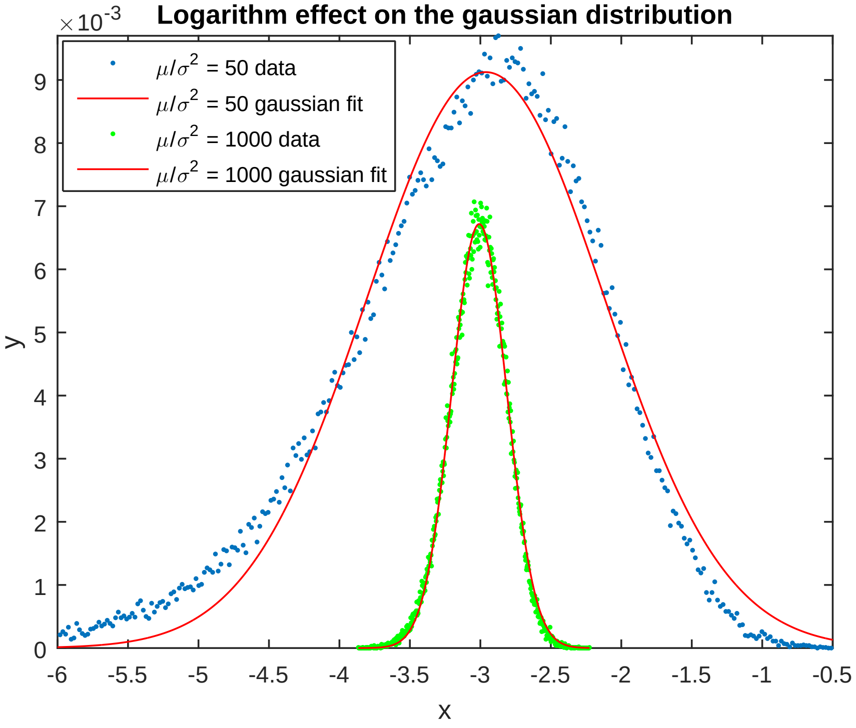

Figure 3.2: Effect of the logarithm function in the output distribution compared to a Gaussian distribution.

For a ratio of 50 the distribution has a Kurtosis value of 4.3 and for the second ratio distribution the Kurtosis value is 3.02. This demonstrates that for a high ratio between the mean and the variance the logarithm's output can also be approximated by the Gaussian distribution. This effect is also illustrated in Figure 3.2, where the distribution of the largest ratio is closer to the Gaussian fit.

The distribution is concentrated around its positive mean, avoiding an approximation to the value of zero and the consequent impact in the derivatives of the logarithmic function $g(a)$. This allows the use of the Taylor series to approximate the moments of the logarithm of a.

Considering an approximation with the Taylor expansion, using three terms, the first two moments are estimated as follows:

- **First moment**:

$$\mathrm{E}[g(a)] = \mathrm{E}[g(\mu_a + (a - \mu_a))] \tag{3.9}$$

$$\mathrm{E}[g(a)] \approx \mathrm{E}\left[g(\mu_a) + g'(\mu_a)(a - \mu_a) + \frac{1}{2}g''(\mu_a)(a - \mu_a)^2\right] \tag{3.10}$$

As $\mathrm{E}[a - \mu_a] = 0$ and $\mathrm{E}[a - \mu_a]^2 = \sigma_a^2$ we can then write that,

$$\mathrm{E}[g(a)] \approx g(\mu_a) + \frac{g''(\mu_a)}{2}\sigma_a^2 \tag{3.11}$$

- **Second moment**:

Analogously to the first moment we can write [101],

$$\mathrm{Var}[g(a)] \approx (g'(\mathrm{E}[a]))^2\mathrm{Var}[a] = (g'(\mu_a))^2\sigma_a^2 \tag{3.12}$$

The first and second moment are proportional to second and first order derivatives. As $g(a) = 10\log_{10}(a)$ then the first and second derivatives can be obtained.

$$\begin{cases} g'(a) = \frac{10}{\ln(10)a} \\ \\ g''(a) = \frac{10}{\ln(10)a^2} \end{cases} \tag{3.13}$$

Substituting the moments by their Taylor expansion, we can finally obtain an estimate of the expected value and variance.

$$\mathrm{E}[g(a)] \approx 10\log_{10}(\mu_a^2) - \frac{10\sigma_a^2}{2\mu_a^2\ln(10)} \tag{3.14}$$

$$\mathrm{Var}[g(a)] \approx \frac{100\sigma_a^2}{\mu_a^2\ln^2(10)} \tag{3.15}$$

3.1.5.3 Results in order of the input signal statistics

As the process $g(a)$ that generates y, has in the input the values from the output of the moving average of the system under study, with a random value that can be approximated by $\mathcal{N}(\sigma_x^2, \frac{\sigma_x^4}{L})$ we have,

$$\begin{aligned} \mathrm{E}[g(a)] &\approx 10\log_{10}(\sigma_x^2) - \frac{10\frac{\sigma_x^4}{L}}{2\sigma_x^4 \ln^2(10)} \\ &= 10\log_{10}(\sigma_x^2) - \frac{10}{2L\ln(10)} \end{aligned} \tag{3.16}$$

$$\mathrm{Var}[g(a)] \approx \frac{100\frac{\sigma_x^4}{L}}{\sigma_x^4(\ln(10))^2} = \frac{100}{L\ln^2(10)}. \tag{3.17}$$

Note that for large L, the mean of y is then the value in decibels of the expected value of the energy estimator input x. The variance of the output y is only dependent on the order L of the moving average. As L is a known and fixed value this allows us to then have an *a priori* knowledge of the expected variance of the energy estimation output. This information can then be used to improve detection of the signals modeled by a GMM.

3.2 Subtractive histogram method for estimation of both noise floor and number of transmitting users

3.2.1 Subtractive histogram method

The proposed subtractive histogram method uses the energy estimation y (see Figure 3.1) of the received channel RF signal and estimates its PDF by calculating the data histogram. As assumed in Subsection 3.1.1 the data follows a GMM. The histogram will then be a mixture of at most K Gaussian distributions, where K is the number of different UE received transmissions with unique power plus the noise floor.

The subtractive method iteratively searches, one by one, the Gaussian distribution components in the histogram of the y energy estimation from the GMM data. Searching by the maximum value of the histogram and then using it as a starting value for a Gaussian fit. The method obtains then the mixture model that will better fit the y histogram and, as K is unknown, also estimates the number of Gaussian distributions in the GMM. The Gaussian components of the GMM are extracted using the algorithm seen in Figure 3.3.

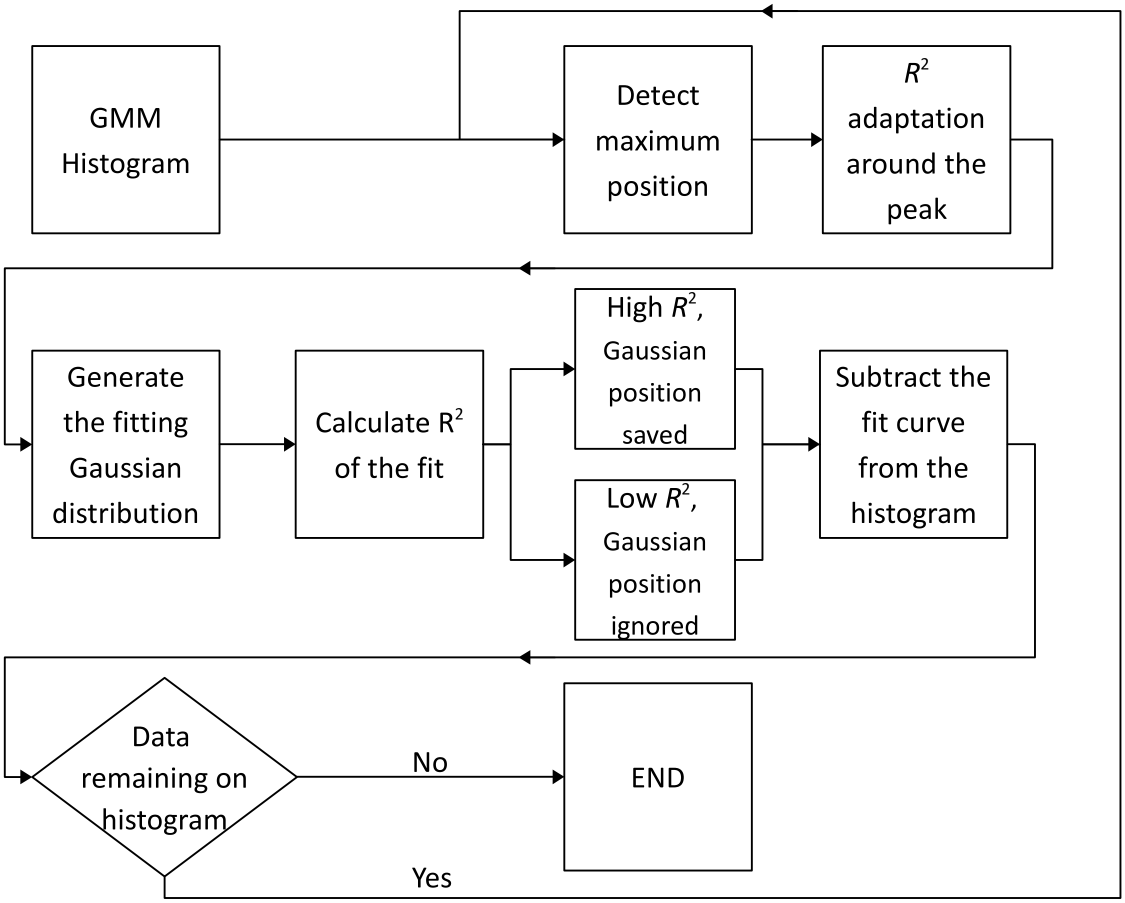

Figure 3.3: Subtractive histogram method for analysis of Gaussian components of the GMM signal.

The method iterates till most of the histogram y, that is defined as 90%, is fitted. The first step is to detect the maximum value on the histogram under evaluation, this will give us the user signal that occurs more often, or the most frequent contribution in the observation for the the GMM. After determining the peak value, the coefficient of determination R^2 is obtained,

$$R^2 = 1 - \frac{\sum_{i=1}^{n}(h_i - \hat{h}_i)^2}{\sum_{i=1}^{n}(h_i - \bar{h})^2} \tag{3.18}$$

where n is the number of bins of the histogram being evaluated, h_i is the Gaussian distribution PDF for each i energy value, $\bar{h}$ is it mean and $\hat{h}_i$ is the y histogram [102]. The R^2 is calculated for multiple fitting Gaussian distributions, with a fixed $v = \mathrm{var}(y)$ variance (from Subsection 3.1.5.2) and a variable M mean. The tested interval for M is given by:

$$M \in [p - v, p + v] \tag{3.19}$$

where p is the detected peak value of the histogram. The value of M that generates the distribution with the closest fit to the original PDF (having a higher R^2) is selected and defined as the mean value that generates the closest Gaussian distribution fit for that energy interval.

For this goodness of fit evaluation, it is defined an interval of three times the theoretical standard variation, where 97.7% of the Gaussian distribution energy is concentrated [103]. This interval around the detected peak is then used for analyzing the R^2.

The difference between the calculated fit and the histogram data in that interval is calculated, if it is an acceptable fit, defined as R^2 being higher than a threshold value of 0.7, then the Gaussian is identified as an transmitting user or the noise floor. If the determined R^2 is low, then the analyzed data does not represent a Gaussian of the GMM and the obtained peak value position is ignored. Nevertheless the calculated Gaussian distribution, that fits the detected peak, is subtracted from the original histogram. The value of $\hat{h}_i$ is updated by removing the Gaussian fit in the following manner:

$$\hat{h}_i^{(k)} \leftarrow \hat{h}_i^{(k-1)} - h_i^{(k-1)}, \tag{3.20}$$

where k is the iteration number. The algorithm will iterate and detect the next maximum value position till $\hat{h}_i^{(k)}$ reaches the majority of the y histogram data is fit by the method. After k iterations, if the remaining data is less than 10% of the original histogram data then the method ends.

3.2.2 LTE Uplink

It was chosen to use LTE uplink signals in order to test the subtractive histogram method. LTE is the current standard for high-speed wireless communication systems. The current trend of moving the LTE to unlicensed spectrum, as discussed in Sub-Section 1.1.3.1, makes spectrum sensing of LTE signals a relevant topic.

The uplink of the LTE standard air interface transmission scheme is based on a Single-Carrier Frequency Division Multiple Access (SC-FDMA) which converts a wideband channel into a set of sub-channels called resource blocks [104]. For each User Equipment (UE) a number of resource blocks are attributed according to the user's needs.

In order to obtain the number of users using LTE in a given spatial region, without demodulating the transmitting signals, the best option is to evaluate the energy of the LTE uplink air interface. The energy analysis allows to separate the users signal by receiving power. Different users generate different powers at the receiver due to path loss and multi-path effect [105].

For the noise floor, in order to obtain a good estimation, it needs to ensured that there are time-slots where no users are transmitting. This is true on the LTE uplink. According to the LTE protocol, there are always, in each uplink frame, free Resource Blocks (RB). One reason for that is that the Physical Uplink Control Channel (PUCCH) that carries the uplink control information is never transmitted simultaneously with user data coming from Physical Uplink Shared Channel (PUSCH) [106]. These periodical free blocks can be used to dynamically obtain an estimation of the noise floor.

As the LTE uplink is a shared medium, at a given moment a resource block may be in one of two states. Noise floor, when no user is present on the resource block and only the noise produced by the environment and by RF front-end itself is observable. User occupation, when a given user transmits a signal with an approximately constant power. The PDF of an interval of acquired signal will then be the sum of the noise and the users processes PDFs.

The energy estimator used in the subtractive histogram method will average a large number of samples of the received RF signal. From the central limit theorem, more specifically De

Moivre–Laplace theorem [107], the histogram of each transmitting user will converge toward a Gaussian distribution. The result, will then be the sum of all users Gaussian components that gives rise to a PDF that follows a Gaussian Mixture Model. The lowest mean component will be the noise floor and the highest value components will be the different UEs received signals with different values of mean power.

3.2.3 Practical experiment with LTE Uplink signals

In order to test the method with Frequency Division Duplex (FDD) LTE signals, three PUSCH symbols for TS36.104 Uplink FRC A3-3 [108] using 15 RBs with a total of 3 MHz of bandwidth, were generated. Each of these three signals are generated with a unique radio network temporary identifier (to simulate different UEs) and the data block contains random generated data. The modulation used is Quadrature Phase Shift Keying (QPSK) and the scheduling is that the three users are allocated in three resource blocks on the same frequency band.

The complete frame that will be tested will be composed of a blank resource block that has the same length as the PUSCH subframe, the PUSCH subframe from the first user, the second user's PUSCH subframe with 4 times higher amplitude than the first and then the third user with a PUSCH subframe with 16 times higher amplitude than the first.

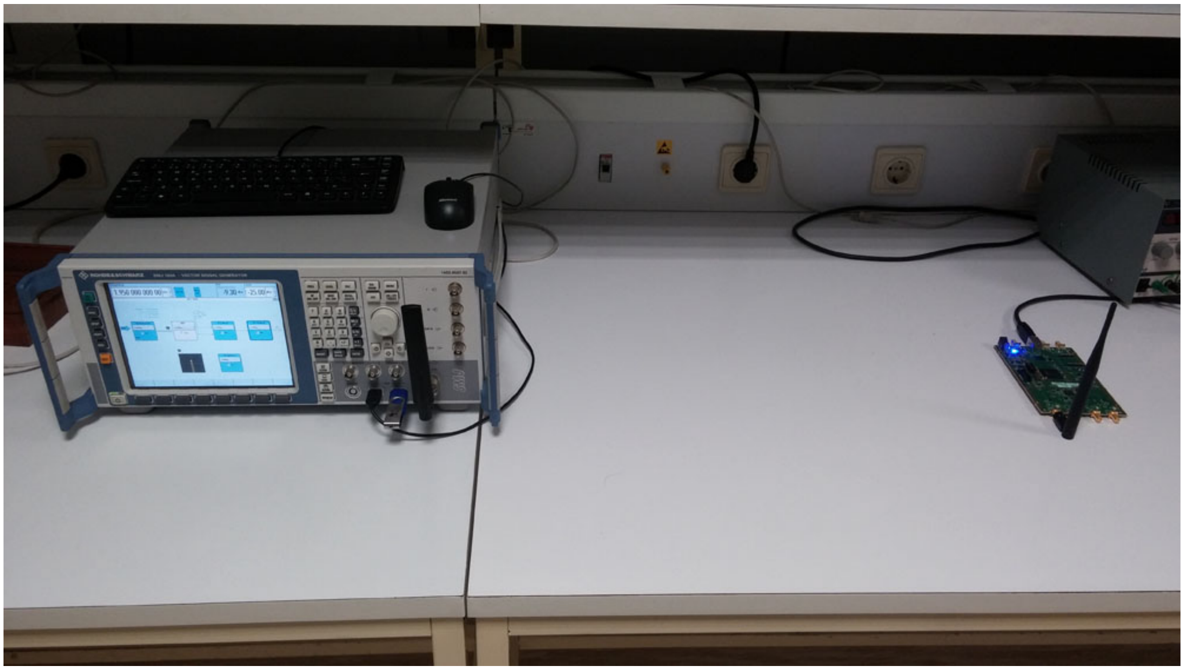

Figure 3.4: The experimental setup to simulate multiple UE up-link transmissions.

The frame is transmitted by a Rohde & Schwarz SMJ100A at −25 dBm and centered at Channel 1 Uplink, 1950 MHz and it will simulate the usage of the LTE uplink by three different UEs. The data will be received by the detection unit, an ETTUS USRP B210 connected trough USB3 to a personal computer as seen in Figure 3.4. The B210 is configured to operate at 4 MSPS in the same central frequency as the LTE signal is transmitted. The received signal has 8900 samples and is analysed with an energy estimator of order 50. This energy estimator has a theoretical variance given from Equation 3.17 of approximately 0.38. The output of the power estimator can be seen in Figure 3.5.

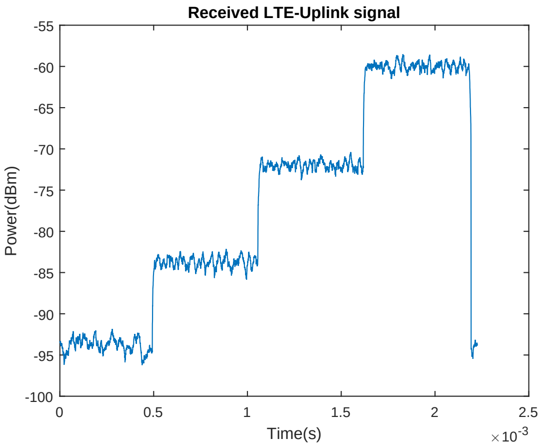

Figure 3.5: Energy estimation of the received LTE-Uplink signal.

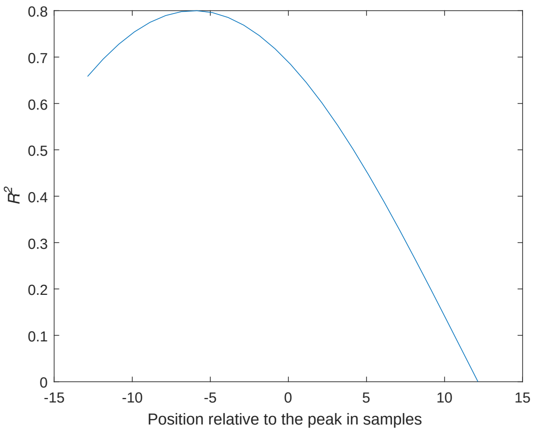

Figure 3.6: Variation of the coefficient of determination around the first detected peak bin.

This data is then analysed using a histogram with a thousand bins and the algorithm from Section 3.2.1 is used with a threshold of 10% of the total energy of the histogram. Distributions with a goodness of fit, $R^2 < 0.7$ are ignored.

The first histogram peak value, is detected at -72dBm and the fit of the mean value is illustrated in Figure 3.6. The curve obtained by the coefficient of adaptation, shows that the first detected peak is approximately six bins away from the local optimum, this allows for a better fit, compared to use only the detected maximum as the mean for the fitting Gaussian. This fit is then removed from the original PDF and a new iteration is run. This iterations of the applied algorithm can be seen in Figure 3.7.

After detecting the four Gaussian distributions present on the signal segment, the remaining data represents 7.8% of the occurrences from the original generated histogram. The calculated R^2 values for the various detected distributions are the following: 0.8 ; 0.86 ; 0.92 and 0.86. As the remaining histogram data is bellow the defined threshold of 10%, the algorithm concludes the iterations. If that wouldn't be the case, then the next distribution that would be detected, by ignoring the data remaining threshold, would reduce the data left in the histogram to 6,6%. This detection would have a coefficient of determination of 0.04 that would be ignored by the method due to the low R^2.

From the obtained distributions it is then possible to have a power estimation for the noise floor, that is given by the lowest detected power distribution. The other three detected distributions refer to the number of transmitting UE present on the shared medium.

3.2.4 Results discussion

The subtractive histogram method proposed in this article was able to determine the number of users and their power in a simulated LTE channel scenario using a PUCSH data transmitted from a signal generator and received in a SDR unit. The energy of the received signal is estimated and its histogram was analyzed to determinate the number of different

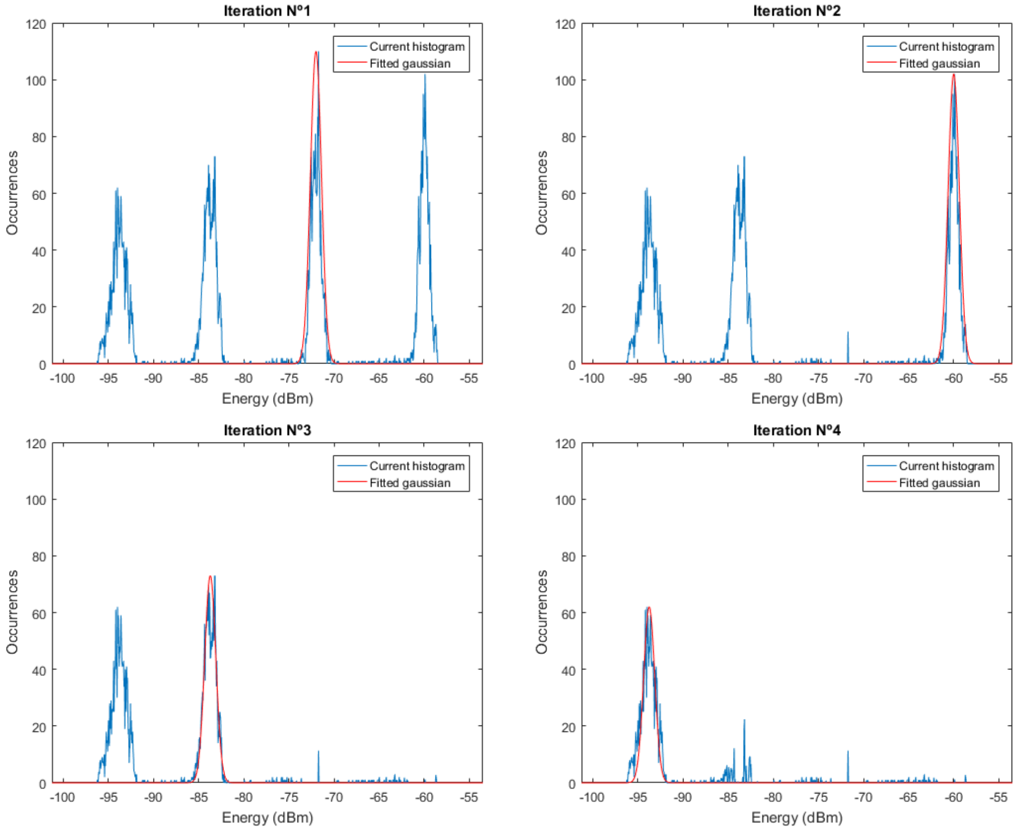

Figure 3.7: Iterations of the subtractive histogram method for the LTE-Uplink data.

distributions. As the energy estimation of the sensed LTE uplink can be modeled by a Gaussian mixture, this allow us to have *a priori* information that allows us to determine the number of distributions presented. The lowest value Gaussian gives an estimation of the noise floor and the remaining distributions give us an estimation of the number of LTE users and their received power.

3.3 Single antenna energy EM clustering

3.3.1 EM algorithm applied to the Time Domain Signal

In the spectrum sensing model as described by Equation 3.1 it is implicitly assumed that a long segment of data samples is formed by the concatenation of sub-segments where either one user is using the channel or noise is present. Therefore, as the energy estimator y can be approximated by a Gaussian distribution, the suitable model for the probability distribution function is the GMM [109]. The mean of each Gaussian would then represent a user and the noise floor can be related with the lowest Gaussian mean estimated. Assuming this model the EM algorithm is used to estimate unknown parameters of the GMM. The EM algorithm was modified to allow histogram-based estimation of the GMM unknown parameters.

3.3.1.1 EM algorithm

Given a set of observations, the EM algorithm aims to compute the maximum likelihood estimation of the unknown parameters of a statistical model [110]. Hence, the available data is assumed to be a set of observations drawn from a mixture of different probability distributions. For the energy estimator we consider the data modeled by a GMM, explaining each data value y as follows,

$$m(y|\Theta) = \sum_{k=1}^{K} \pi_k \varPhi_k(y|\theta_k) \tag{3.21}$$

where $\Theta = \{\theta_1, \theta_2 \dots \theta_K, \pi_1, \dots \pi_K\}$ denotes the set of parameters of the K normal distributions, with normal density given by $\varPhi_k$ that is characterized by the parameters $\theta_k = \{\mu_k, \sigma_k^2\}$ and π_k is the weight of each distribution for the data y. The weights are constrained to sum to one, e.g $\sum_k \pi_k = 1$.

The algorithm starts with initial guesses for each unknown parameter of the Θ set. A common way to set up the initial values is to choose K random samples from the data points for the means $\hat{\mu}_k$ and the overall data variance as the initial value for $\hat{\sigma}_k^2$. For the parameters $\hat{\pi}_k$ an equal proportion, $1/K$, can be initially attributed to each distribution.

After the initial guesses, the algorithm proceeds by recursively applying the following two steps:

- **Expectation step**: For each data value, given the parameters of the mixture model, compute the *a posteriori* probabilities of belonging to each distribution. Using the Bayes Rule, the probability that each data value, $y_i, i = 1, 2, ..., N$, belongs to a $\varPhi_k(.)$, also called *responsibilities*, is given by

$$\hat{\gamma}_{k,i}(\varPhi_k|y_i) = \frac{\hat{\pi}_k \varPhi_k(y_i|\theta_k)}{\sum_{l=1}^{K} \hat{\pi}_l \varPhi_l(y_i|\theta_l)} \tag{3.22}$$

- **Maximization step**: The estimated probabilities on the Expectation step are integrated in the maximum likelihood estimation of parameters of the normal distributions [111]. Therefore, the updates depend on the weighted values. The aim of the maximum likelihood estimation is to compute the parameters Θ that give the best fit to the given set of independent data observations.

$$\hat{\mu}_k = \frac{\sum_{i=1}^{N} \hat{\gamma}_{k,i} y_i}{\sum_{i=1}^{N} \hat{\gamma}_{k,i}} \tag{3.23}$$

$$\hat{\sigma}_k^2 = \frac{\sum_{i=1}^{N} \hat{\gamma}_{k,i}(y_i - \hat{\mu}_k)^2}{\sum_{i=1}^{N} \hat{\gamma}_{k,i}} \tag{3.24}$$

$$\hat{\pi}_k = \sum_{i=1}^{N} \frac{\hat{\gamma}_{(k,i)}}{N} \tag{3.25}$$

The Expectation step and Maximization step are iterated until the convergence criterion is met (e.g., a maximum number of iterations). The algorithm's output will then give us the estimation of the mean value, variance and mixture proportion of each normal distribution on the analysed model.

3.3.1.2 Illustrative Example

To test the described method we have generated an artificial signal, encompassing three users where each one is being received with a different power. A period where only noise floor is present, which has the lowest power level, was also defined. The users and the noise floor are interleaved in order to create the test signal, as described in Table3.1.

Signal	Power (dB)	Estimated Power (dB)	Appearance order
Noise Floor	-100dB	-100.08	3rd
Low power	-98dB	-98.04	1st
Medium power	-96dB	-95.94	2nd and 5th
High power	-94dB	-93.89	4th

Table 3.1: Generated test signal components.

The test signal x is divided in 5 time slots with $N = 1000$ samples. Each user is present in different time slots, one of the users occupies two time slots, and one of the time slots has no user transmitting (noise floor). The data is generated as a complex Gaussian random variable. Due to its simplicity, it is used as an approximate model for both the noise floor and the received signal. Notice that OFDM signals, as in 802.11n, are expected to have Gaussian distributions [112]. The power of the generated signals is given in Table 3.1, and is then evaluated with the energy estimator as described in Figure 3.1 with $L = 100$. The output y of the estimator is shown in Figure 3.8.

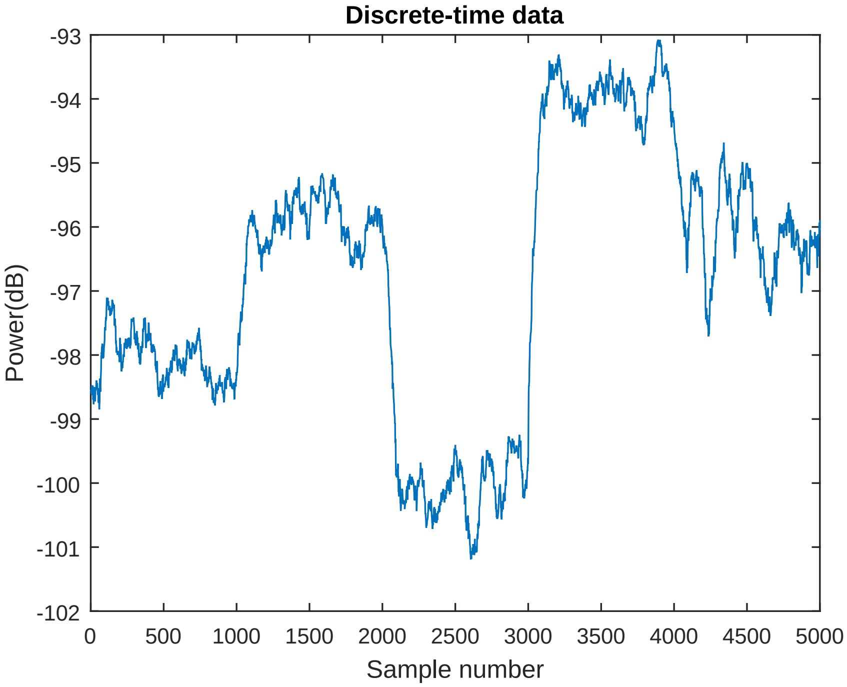

Figure 3.8: Power estimation of the generated data.

The data is then analysed with the Expectation Maximization algorithm in order to obtain the unknown parameters of the normal distributions present in the model. The stopping criteria in the EM is 100 iterations. The Figure 3.9 shows the evolution of the estimated mean for each of the $K = 4$ distributions.

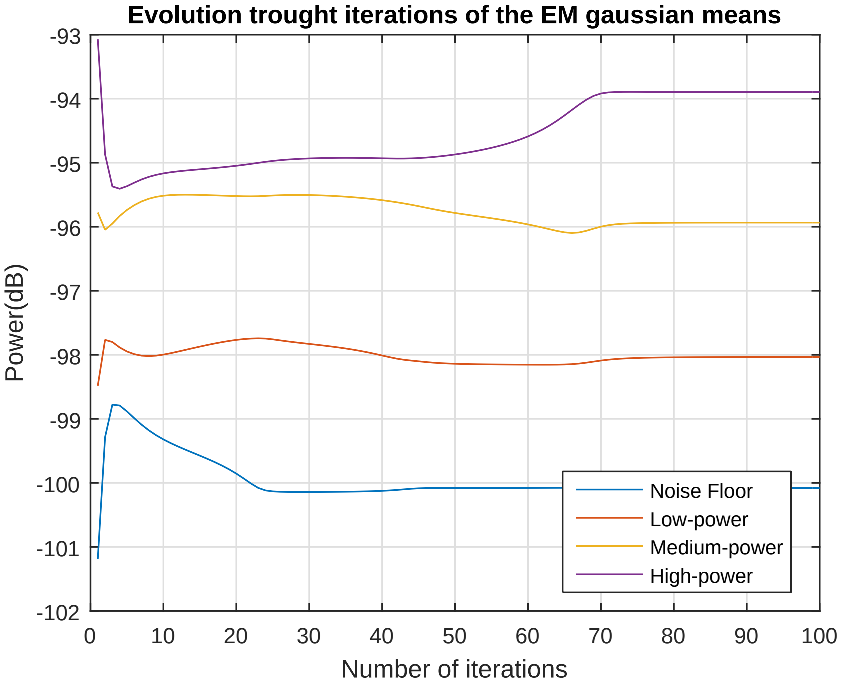

Figure 3.9: Analysis of the convergence of each distribution mean.

After convergence, the mean values of the Gaussian distributions are -100.08 dB, -98.04 dB, -95.94 dB and -93.89 dB. After the EM convergence, the *responsibility* parameter for each sample is also informative. This parameter gives us the channel occupation through time, and also identifies the individual user within a specific time slot. The responsibilities were smoothed with a moving average filter or order $L = 100$, and are illustrated in Figure 3.10.

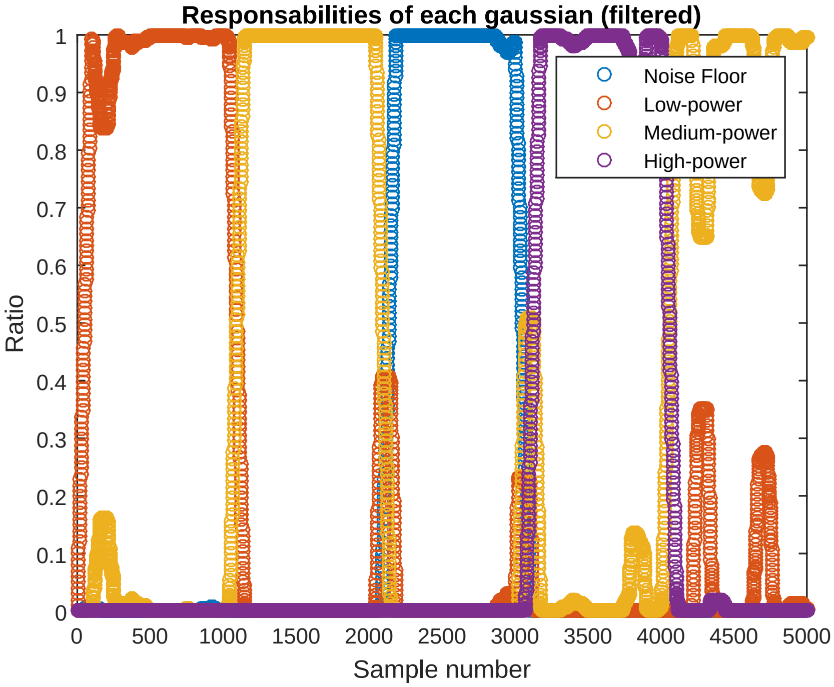

Figure 3.10: *Responsibility* of each distribution in discrete-time.

The EM output can be analysed by using the estimated parameters from the method to generate the probability density function of the mixture. These distributions are then compared with the input data histogram. Figure 3.11 compares the two approaches.

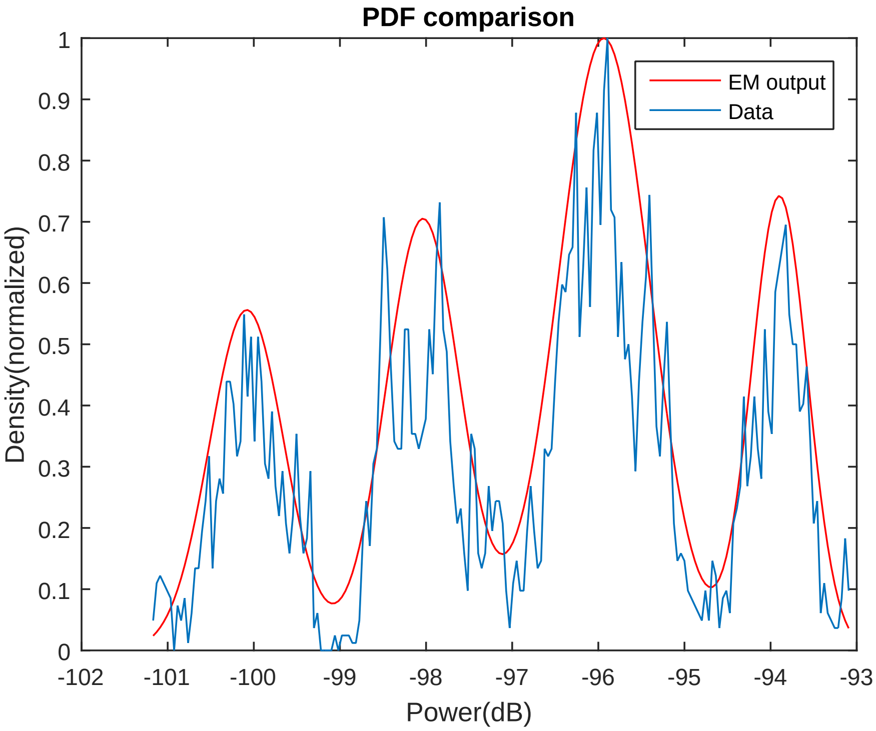

Figure 3.11: Comparison of the data histogram and the EM estimated distribution. The data was generated according with the parameters of Table 3.1.

To analyze the performance of the EM algorithm, the ROC curve of the Energy Detection (ED) was calculated from the previously generated simulation. In this evaluation a threshold with a variable probability of false alarm is applied to different uncertainty values Δ of the noise power estimation. The calculated curves are compared with the performance obtained when using the estimated noise floor with the Expectation Maximization method.

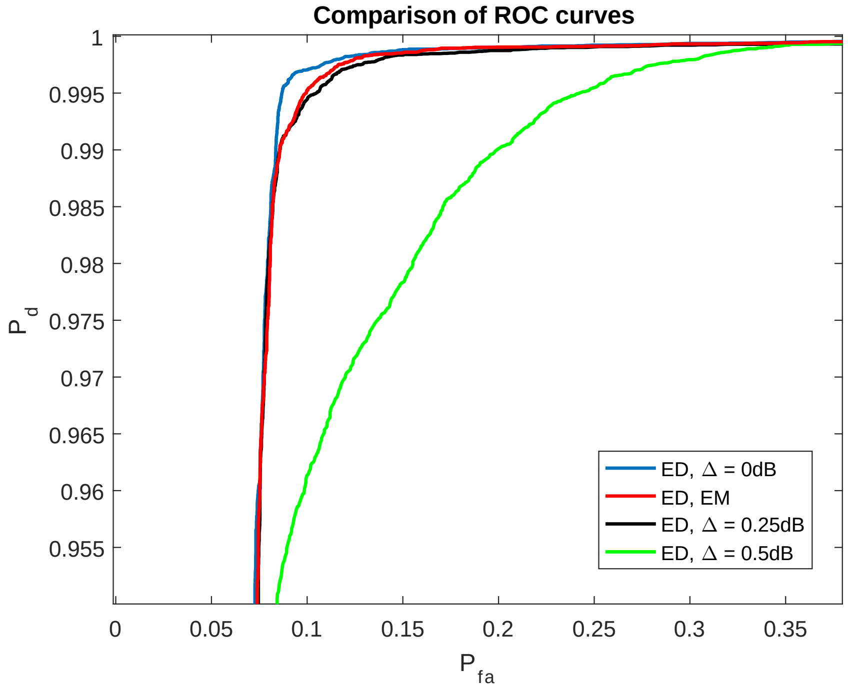

Figure 3.12: ROC curve comparison between a fixed noise floor estimation with variable uncertainty and the EM noise floor estimation.

In Figure 3.12 the various ROC curves are compared. The energy detection that used the noise power estimation with the EM algorithm has, as expected, a worse performance than the ideal ED at $\Delta = 0\,\text{dB}$, but shows a similar performance to an ED with $\Delta = 0.25\,\text{dB}$.

3.3.2 Histogram Based EM Algorithm

In the previous section the standard EM algorithm in the time domain was described. The parameters of the Gaussian mixture model were estimated directly from the energy estimation output. Therefore, the method allows not only to determine these parameters, but can also identify the Gaussian component to which a data point belongs. To obtain a more efficient approach an algorithm version based on the data histogram was developed. The EM algorithm will then be applied to the bin values and not to all energy values in a segment of data. That way, as the number of bins is smaller than the number of data points in the energy estimation output, the complexity, either in terms of memory and operations, is reduced significantly. The disadvantages are the loss of precision in identifying the exact sample where the distributions are present and the quantization error induced by the histogram intervals.

The EM algorithm applied to the time domain can be easily adapted to work with histogram data. Let $y_i, i = 1, 2, ..., N$ be the input data, then $\bar{y}_j, j = 1, 2, ..., M$ denotes the center of the bins of the histogram, and M gives the number of intervals. The number of occurrences in each interval is given by o_j.

- **Expectation step**: For each histogram bin, compute the *a posteriori* probabilities of belonging to each distribution given the parameters of the mixture model. Using the

Bayes rule, the probability that a bin $\bar{y}_j$, with o_j occurrences, belongs to a $\mathit{\Phi}_k(.)$, also called *responsibilit*ies, is given by

$$\hat{\gamma}_{k,i}(\mathit{\Phi}_k|\bar{y}_j) = \frac{\hat{\pi}_k \mathit{\Phi}_k(\bar{y}_j|\theta_k) o_j}{\sum_{l=1}^{K} \hat{\pi}_l \mathit{\Phi}_l(\bar{y}_j|\theta_l) o_j} \tag{3.26}$$

- **Maximization step**: The estimated probabilities on the Expectation step are integrated in the maximum likelihood estimation of parameters of the normal distributions. Therefore, the updates depend on the weighted values. The aim of the maximum likelihood estimation is to compute the parameters Θ that give the best fit to the given set of independent data observations. The calculated mean for k will then be the weighted mean of the histogram values using the calculated responsibilities for that distribution.

$$\hat{\mu}_k = \frac{\sum_{j=1}^{M} \hat{\gamma}_{k,j} \bar{y}_j o_j}{\sum_{j=1}^{M} \hat{\gamma}_{k,j} o_j} \tag{3.27}$$

The variance will be a weighted sum of the variances within each bin

$$\hat{\sigma}_k^2 = \frac{\sum_{i=1}^{N} w_{k,j} (\bar{y}_j - \hat{\mu}_k)^2}{\sum_{j=1}^{N} w_{k,j}} \tag{3.28}$$

where these weights are given by

$$w_{k,j} = \frac{\hat{\gamma}_{k,j} o_j}{\sum_{j=1}^{N} \hat{\gamma}_{k,j} o_j} \tag{3.29}$$

The mixing coefficients of GMM are calculated by

$$\hat{\pi}_k = \frac{\sum_{j=1}^{N} \hat{\gamma}_{k,j} o_j}{\sum_{j=1}^{N} o_j} \tag{3.30}$$

Once again the expectation and maximization steps are iterated until the convergence criterion is met. The algorithm's output will then give us the estimation of the mean value, variance and mixture proportion of each normal distribution on the analysed model from the histogram data.

The performance improvement in the EM can be observed by comparing the number of FLoating-point OPerations (FLOP) using both methods. The complexity, in terms of FLOP, of the algorithm is measured using the data described in section 3.3.1.2 but with a variable number of samples N. The number of bins used on the EM based histogram is one hundred. Table 3.2 presents the results.

Number of points	Histogram (MFLOPS)	Time (MFLOPS)
100	2.4	2.2
150	2.4	3.3
200	2.4	4.4

Table 3.2: Comparative of FLOP by EM implementation.

As expected for the histogram implementation the number of FLOP remains constant with increasing number of points, as the histogram will always have a fixed number of outputs. Using the time dependent data directly, the number of FLOPS is smaller but quickly matches the value for the histogram implementation. The time implementation complexity will increase linearly with the analysed number of points.

3.3.3 Estimating the number of distributions on the model using EM

The EM algorithm assumes that the number K of distributions is fixed and known *a priori*. If there is no information on the number of distributions present on the received signal, then an alternative solution needs to be addressed. The next sections present two different strategies to estimate the GMM model order, i. e.,the number K of distributions.

3.3.3.1 Elbow method

The elbow method is based on the comparison of two Cumulative Distribution Functions (CDF) [113]. One of the CDFs is estimated using the GMM model, for a variable order K, obtained by the EM algorithm and the second is obtained directly from the complex-valued input data. The Mean Squared Error (MSE) between the two CDFs is then estimated for increasing values of K, that are part of the mixture model used in the EM algorithm. The optimal value for K corresponds to the largest slope variation in the MSE for the different values of K.

A block diagram describing the elbow method process is described in Figure 3.13.

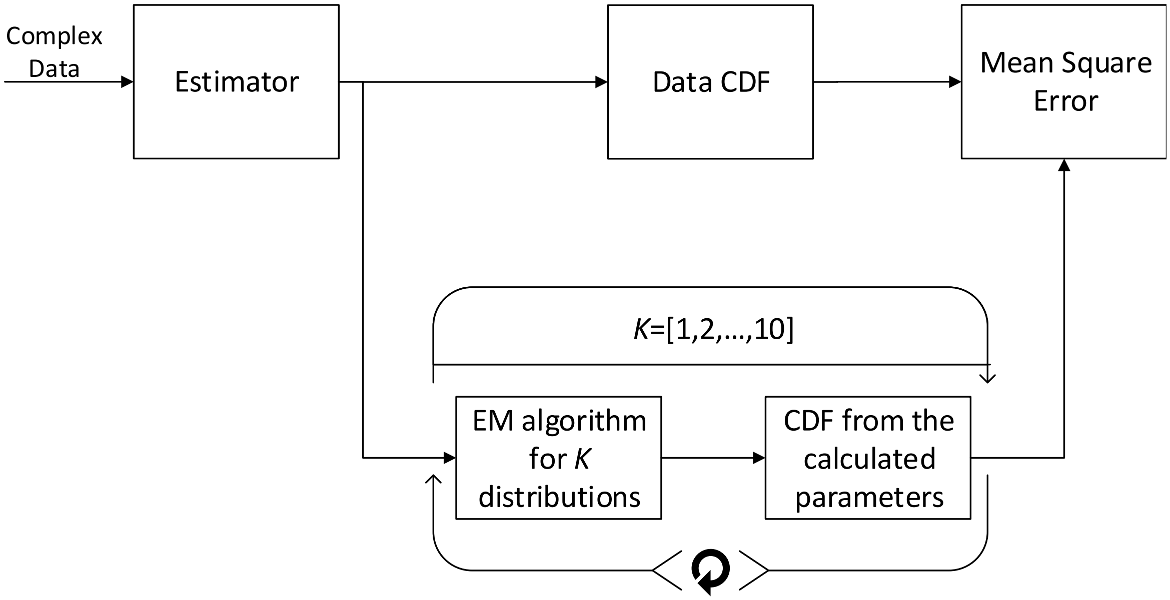

Figure 3.13: Elbow method used to determine the number of distributions present on the data.

In this method the input of the EM algorithm is the output of the energy estimator, as described in the block diagram of Figure 3.1. The EM algorithm is repeated for K varying from $1 \rightarrow 10$ Gaussian distributions in the GMM model until the error reaches an elbow point.

The CDF of the GMM, estimated by the EM, is then compared to the cumulative histogram of the energy estimator output.

Figure 3.14 illustrates the MSE between the CDFs for the different values of K using the simulated data described before (sec. 3.3.1.2). Furthermore, the largest value of the derivative of the MSE error is also for $K = 4$.

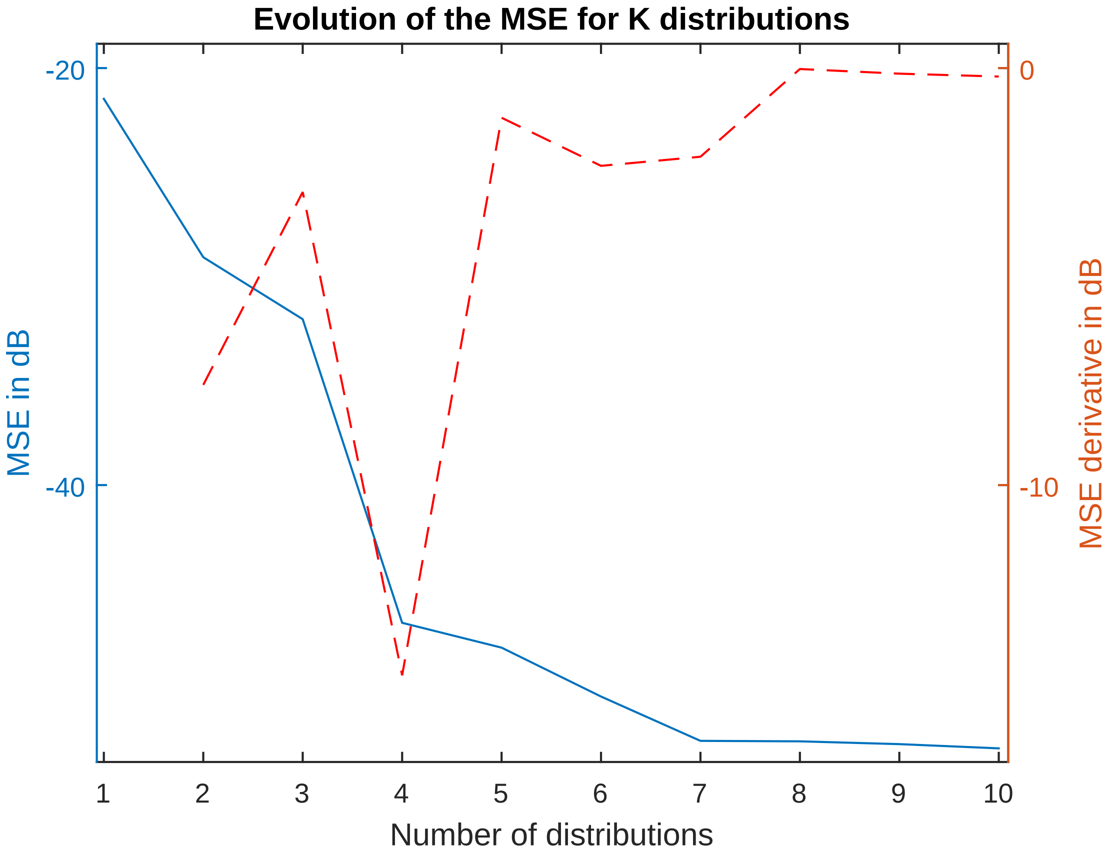

Figure 3.14: MSE evolution (full line) for an increasing number of distributions. The inflection point is clearly visible in derivative (dashed line) of the MSE for $K = 4$.

However, as will be seen in the section 3.3.4, the elbow method does not perform well with real world data, as the latter follows the GMM model only approximately.

3.3.3.2 Overfitting Method

In this section we propose a more robust method to estimate the number K of Gaussian mixtures even when the data does not follow a low order GMM. From Equation 3.17 we can verify that the variance of the Gaussians that compose the mixture is a function of the order L of the moving average. We can take advantage of this *a priori* information by considering a large number of Gaussians to overfit the number of components of the GMM. The distributions with a variance largely different from the theoretical value given by Equation 3.17 are then discarded.

In this overfitting methodology, the GMM will have an initial order of $K_o \ll K$ which corresponds to the number of transmitting users and noise floor. Using (3.17) we can distinguish between Gaussian distributions, from noise floor and transmitting users, from other noise sources. This method can be compared to a model selection based on hypotheses testing [114], where the testing hypotheses are the known variance of each Gaussian distribution used on the overfitting.

For a robust fit of the analysed data histogram, every Φ_k of the GMM whose variance is not close to the theoretically expected value or its contribution to the overall model is negligible, is discarded. Therefore, after the overfitted model is obtained from the EM, the Φ_k of the GMM is chosen according to the following criteria.

1. The distribution's variance σ_k^2 should be in the range defined by,

   $$\frac{1}{t}S_y^2 < \sigma_k^2 < tS_y^2, k \in \{1, 2, ..., K\}. \tag{3.31}$$

   Where $\mathrm{Var}[y] = S_y^2$ is the calculated theoretical variance of y calculated by using Equation 3.17, $t \in]1, +\infty[$ is a tolerance factor to accommodate the model imprecisions and the ovefitting initialization.

2. Additionally, the distribution's *responsibility*, π_k, should be larger than a threshold α.

Both t and α are two user defined parameters according to the experimental conditions.

3.3.4 EM application in real-world Wi-Fi data

A setup for a real-world application of the EM algorithm for spectrum sensing was assembled with two smartphones connected through Wi-Fi to an access point. The sensing device is an Universal Software Radio Peripheral (USRP) B200 SDR platform controlled by a personal computer.

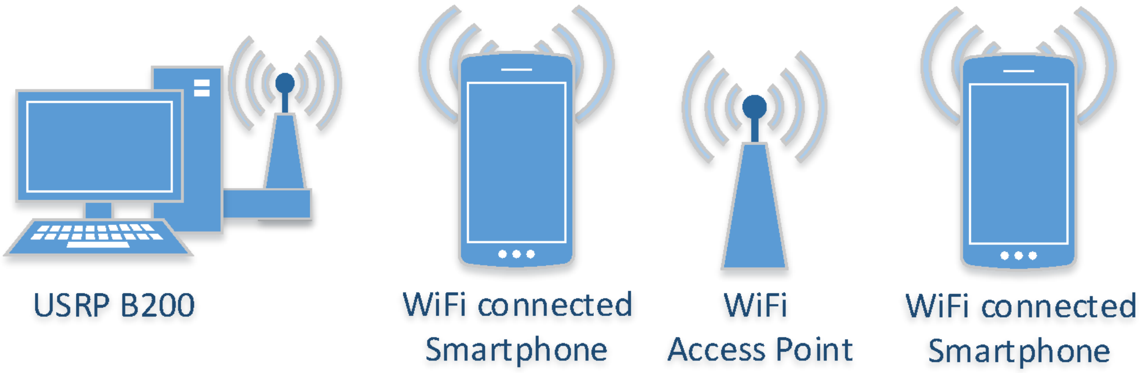

Figure 3.15: Diagram of the Wi-Fi setup.

The test was conducted indoors in a dense urban environment. In this setup the USRP is in the same room as the first smartphone. The router is further away in an adjacent room and the second mobile phone, that is the farthest from the USRP, is in a third separated room. The equipment does not change position during the setup and there are no moving elements in the setup.

Due to the different distances of these three devices to the USRP, the received signals from each equipment will have different power levels. The USRP B200 acquired 10^7 samples during 2.5 seconds using a sampling frequency of 4 MHz, centered at 2432 MHz (802.11 - Channel 5). This data was analysed by the energy estimator described in Figure 3.1 with a moving average of $L = 100$ coefficients, which corresponds to an integration time of $25\,\mu$s. Since the length of the impulse response in an indoor environment is generally of a few hundred nanoseconds [115], this integration time allows us to ignore the multi-path fading effect. We can approximate the variance for the energy estimator output by using (3.17), which for our case is approximately given by $S_L = \text{Var}[e] \simeq 0.189$.

For detection purposes, the histogram version of the EM algorithm presented in section 3.3.2 was used. In this method, the output of the energy estimator is evaluated by forming a total of 1000 histograms, each encompassing 10^5 samples. Each histogram has 1000 bins, uniformly distributed in amplitude. Each histogram was analysed with the EM algorithm with a stopping criterion of 100 iterations. In Figure 3.16, we can observe the application of the elbow method to one of the data segments.

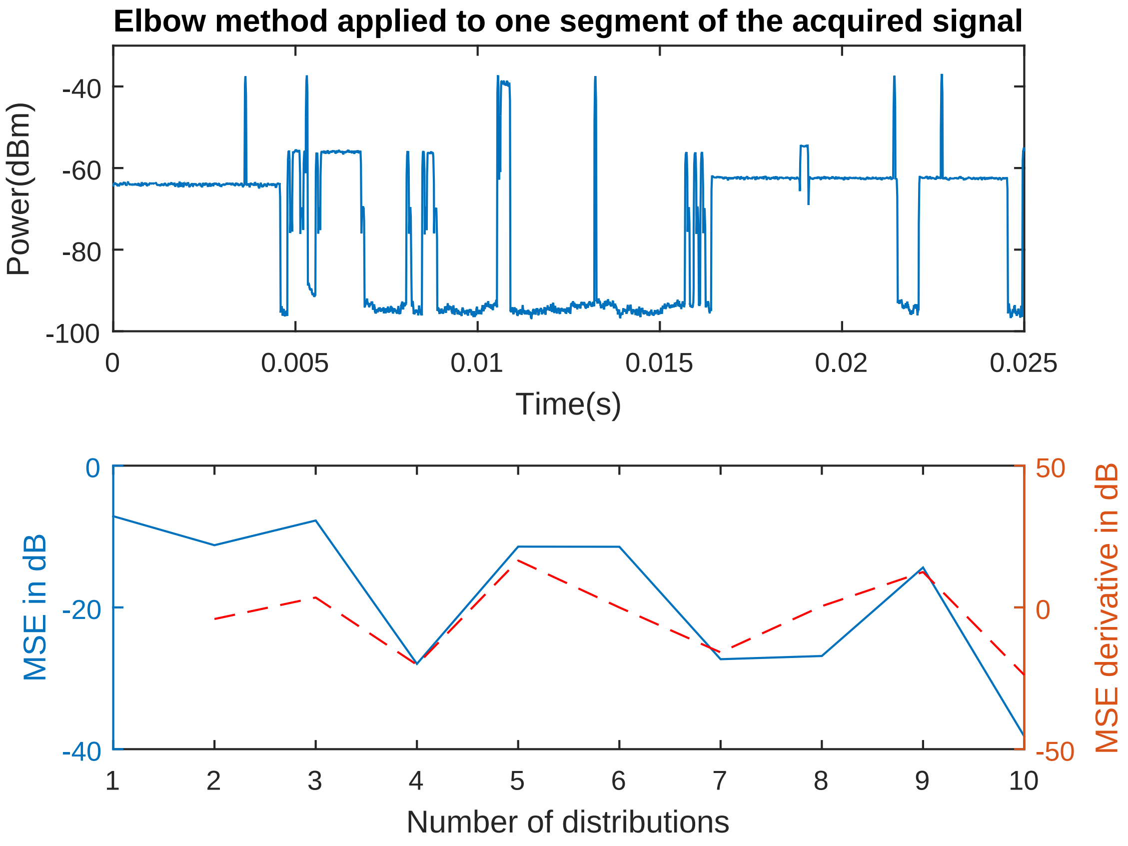

Figure 3.16: On the top the used data segment. On the bottom the MSE derivative of the elbow method where a clear inflection point is not present for $K = 4$.

It is not possible to obtain a conclusive answer for the number K of distributions, as the elbow point is not present on the MSE plot. A similar behavior is obtained for the other data segments. The absence of a clear inflection point is due to an acquisition in a non controlled urban environment, where interference from other Wi-Fi devices is to be expected.

For comparison we applied the overfitting method, as explained in Section 3.3.3.2, to the same signal. Each data segment is evaluated with a histogram of 1000 equally distributed bins. In spite of knowing the number of users in the experimental set-up, we consider to initially overfit the data with $K_o = 10$ Gaussians.

Taking advantage of *a priori* knowledge of the variance, the nuisance parameter $t = 5$ was set. This means that distributions with a variance five times lower or five times higher than the expected S_y^2 will be discarded. The other nuisance parameter was chosen as $\alpha = 0.001$ to discard Gaussian distributions with a small contribution (*responsibility*) to the GMM. By repeating this process for all the segments, we obtained the results shown in Figure 3.17.

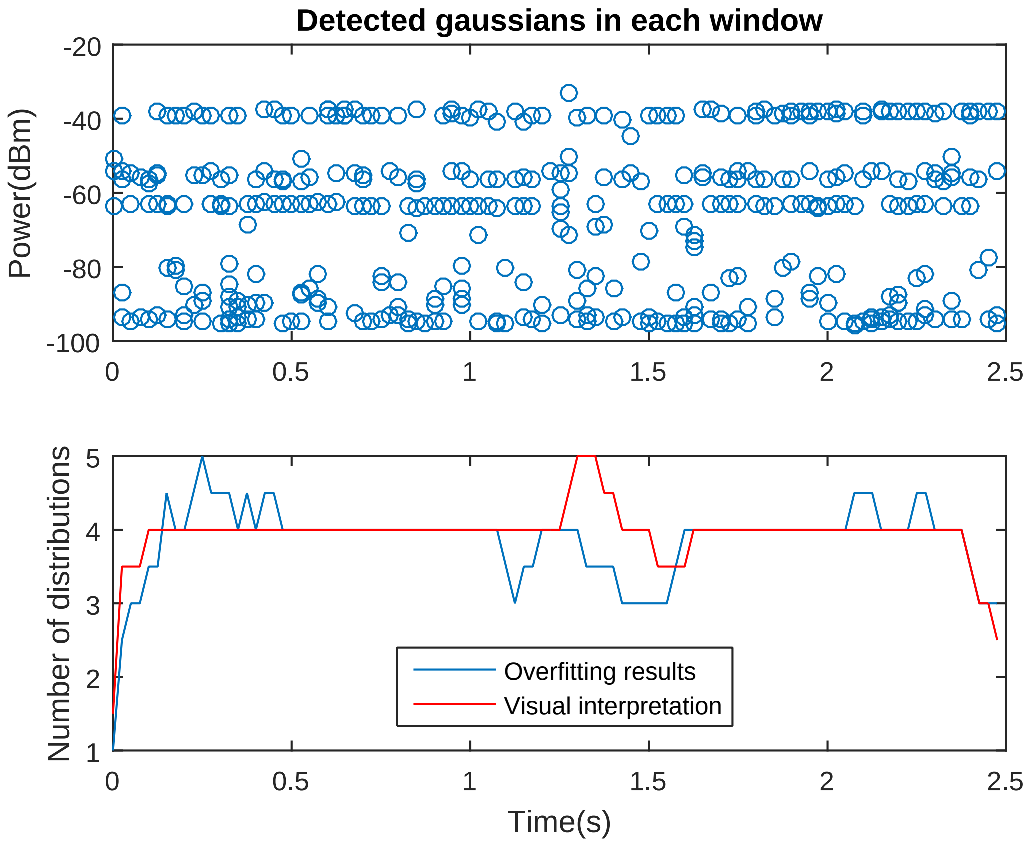

Figure 3.17: On top the mean power of the identified distributions. On bottom the number of detected distributions and the number obtained by visual inspection.

In the experiment three Wi-Fi devices were transmitting information in a non-controlled way. Due to this, for each segment a different utilization of the channel occurs for each Wi-Fi device. To overcome this indeterminacy, each segment was visually analysed thus determining the number of expected users for each segment. As both estimations are noisy, a median filter of order ten was used to obtain a more stable result.

The results show a visible tendency for the detected Gaussian distributions to concentrate around four different power values. The three highest concentration values can be attributed to the two smartphones and the access point transmissions. The lowest value is the contribution of the noise floor to the GMM. The observed large dispersion near the noise floor is explained by the nature of the test. This test was performed in a real urban environment and other remote access points are being received, with a low power, during the experiment.

The mean of the number of detected distributions is 4.16, which is very close to the true value of $K = 4$. The number of estimated distributions in each segment is shown on the bottom of Figure 3.17. While the curves of the number of detected distributions are not exactly identical, they show a similar behavior, reliably determining the expected number of distributions on the experiment.

The responsibilities of each distribution of the GMM in the data are calculated by the EM algorithm. These responsibilities can be used to determine which time slots are being occupied by each user. They can be seen in Figure 3.18.

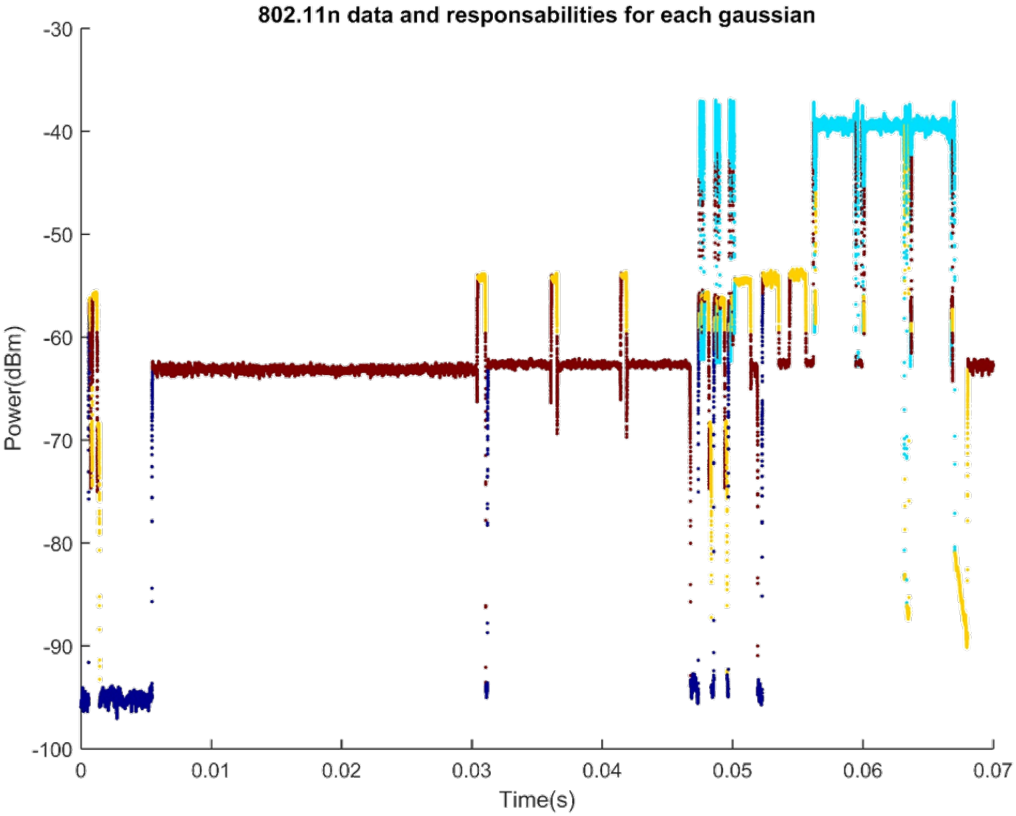

Figure 3.18: Responsibilities of each Gaussian distribution on a signal segment.

The Wi-Fi channel is not constantly occupied. In an analysed segment of data, there may be a time interval with no transmissions. In this situation, the distribution with the smallest power models the background noise. This allows a robust estimation of the background noise power level and to determine the detection threshold to implement a CFAR detector. For this application, the threshold is defined to have a CFAR of 0.1%. The instantaneous noise floor value is estimated using the lowest Gaussian distribution given by the overfitting method in the last ten segments. The distribution mean and variance is then used to extract the threshold for the defined CFAR. Figure 3.19 illustrates the obtained estimation of the noise floor level and also the corresponding threshold.

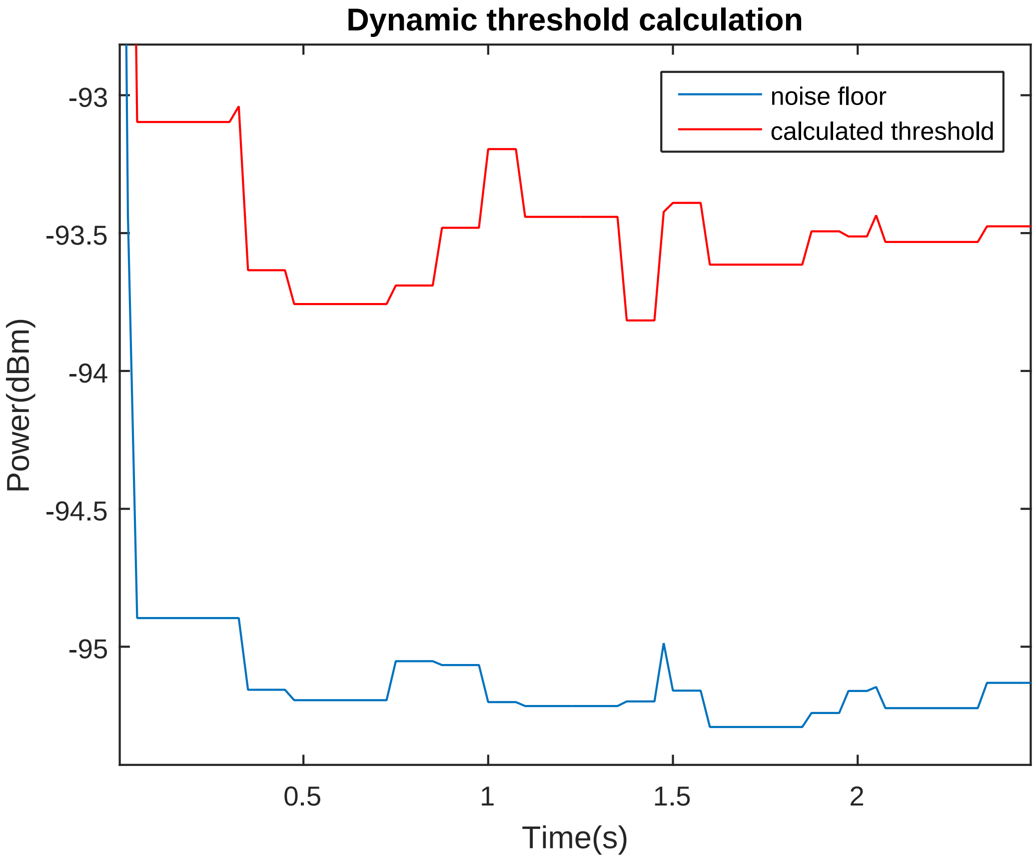

Figure 3.19: Calculation of the dynamic threshold based on minimum variance estimation.

For reference the noise level of the USRP front-end was measured without any transmission and the measured mean value for the noise floor was of $-95.5\,\mathrm{dB}$, consistent with the estimation obtained by the proposed method. For each new segment of data a new threshold is calculated based on the instantaneous noise floor estimation. This value is used to detect white spaces on the analysed frequency band as illustrated in the data segment presented in Figure 3.20.

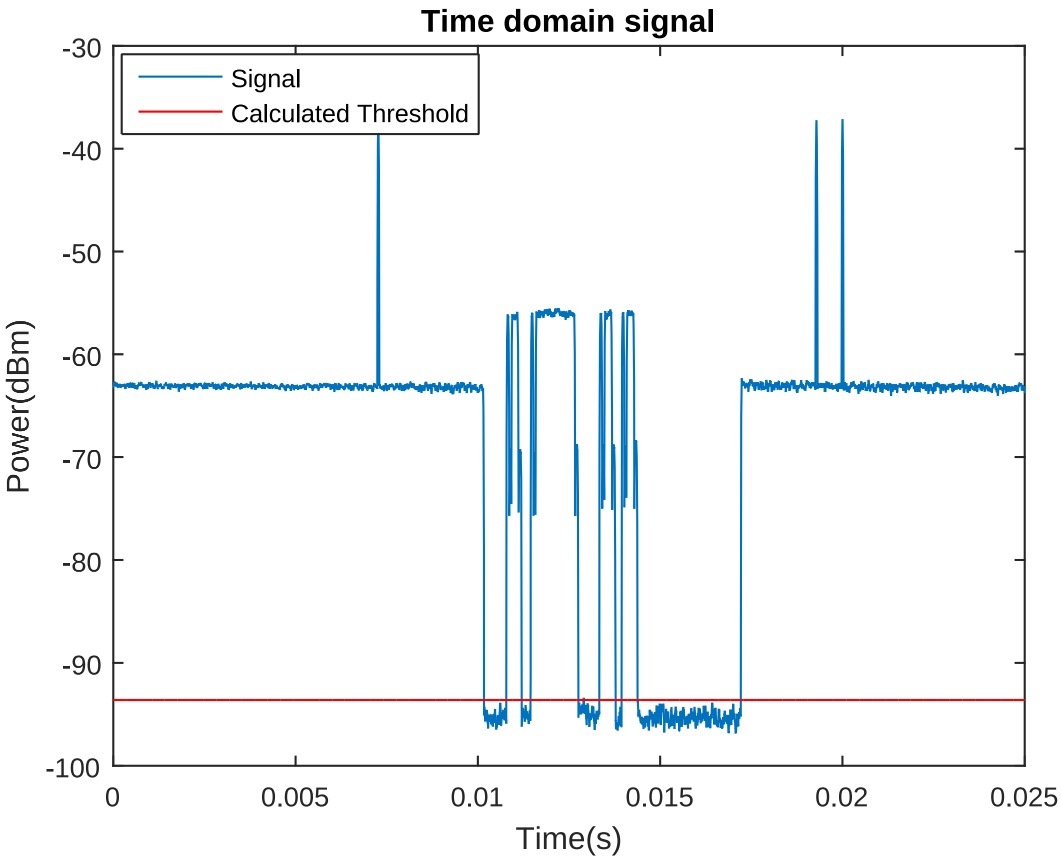

Figure 3.20: 802.11 signal in time and threshold.

The calculated CFAR threshold, based on the noise floor estimation, allows to quickly detect the occupancy of the transmission band.

3.3.5 Results discussion

The used Expectation Maximization algorithm is able to automatically extract useful information from energy spectrum sensing. The algorithm analyzes the logarithm of the averaged signal energy estimates, allowing a better dynamic range in the calculated histogram. It was shown that for a sufficiently long integration time, a GMM can be assumed for the RF signal acquisition and the EM algorithm can be used. This method dynamically estimates the noise floor from the input signal, provided that there are regular periods with no transmissions on the channel. It was also shown that the EM algorithm is able to obtain the number of transmitters, their relative power and an estimation of the amount of time each one is occupying the channel. The classical EM algorithm was also adapted to analyze histogram data instead of raw data samples, making the algorithm more amenable to real time implementations. The method allows the implementation of a CFAR detector to quickly determine white spaces on the spectrum. The results from the real-world environment Wi-Fi test, acquired with a USRP B200 software defined radio, attest the validity of the proposed methodology.

3.4 Two antenna EM Clustering using both phase relationship and energy

3.4.1 Hybrid phase relationship and energy detection

Energy detection is the most employed method for determining the occupation of the RF medium. It is a non-coherent method where no *a priori* knowledge of the received signal is known. Both implementation and computational complexity of this method are relatively low. In the previous Sub-Chapter the EM algorithm was evaluated using as input data the energy estimation of the acquired RF signal from a single antenna. In this Sub-Chapter the usage of the EM algorithm for a two dimensional (2D) case will be evaluated to improve detection performance. Using a two antenna system the EM will model both energy and phase relationship between antennas with 2D Gaussian distributions and classify the acquired data into noise and signal subspaces.

3.4.1.1 Phase relationship between two antennas

In a dual antenna receiving RF system each individual element will have different propagation distances from the transmitted signal S.

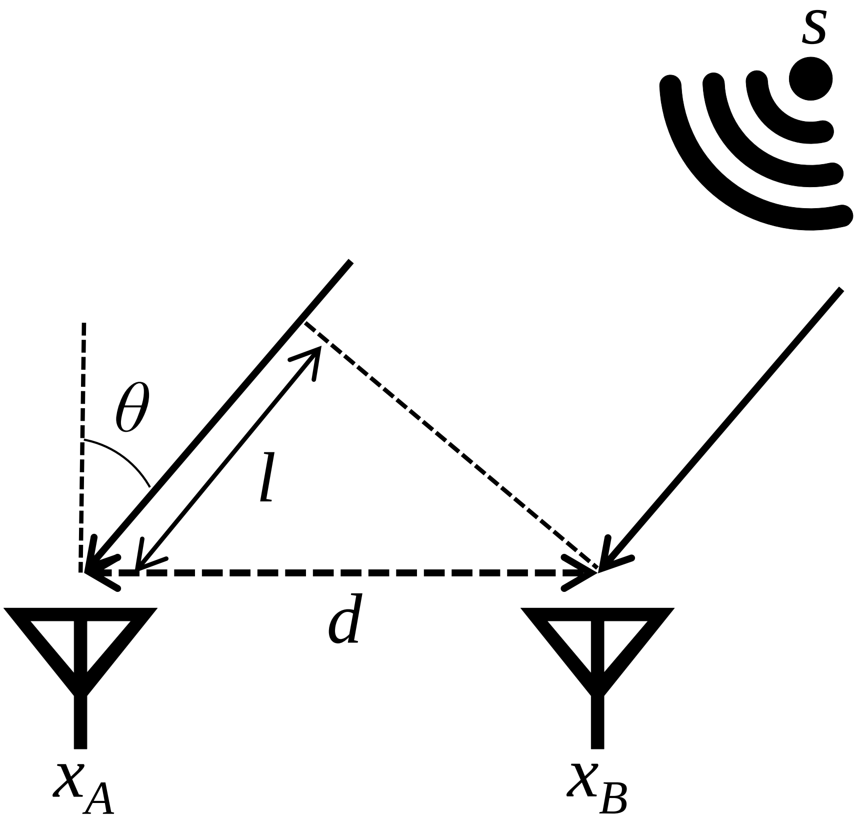

Figure 3.21: DoA scenario with a S transmission being received by two elements, x_A and x_B .

As the radio wave propagates at the speed of light c, then each antenna will obtain the same RF signal but with a phase shift α that can be given by,

$$\theta = \frac{2\pi}{\lambda} l \tag{3.32}$$

where λ is the transmitting signal wavelength and l is the path length difference between antennas.

Assuming the far-field case, where is assumed that the wave propagates in parallel through space [116], we have the scenario seen in Figure 3.21. The phase difference α can be calculated by the inner product of both received signals and is given by,

$$\alpha(n) = \angle[x_A(n)x_B^*(n)] \tag{3.33}$$

where $x_A(n)$ and $x_B(n)$ are the complex sampled signals from respectively the first and second antenna, * indicates the complex conjugate and $\angle$ denotes the phase angle of the complex number.

3.4.1.2 Two dimensional analysis of energy and phase relationship

The instant energy estimation e, of the acquired signal from both antennas can be given by,

$$e(n) = x_A(n)x_A^*(n) + x_B(n)x_B^*(n). \tag{3.34}$$

Assuming that the sampling frequency is higher than the minimum duration of the signal that is to be detected, a better testing value for the signal energy can be obtained by averaging the incoming signal. The energy test statistic T_e, will then be a moving average of order L of the instant energy.

$$T_e = \frac{1}{L}\sum_{n=0}^{L-1} e(n). \tag{3.35}$$

The same process is done for the phase difference estimation, where the phase difference test statistic T_α, can be given by,

$$T_\alpha = \frac{1}{L}\sum_{n=0}^{L-1} \alpha(n). \tag{3.36}$$

Assuming a high order L, both energy and phase difference test statistic distributions can be approximated to Gaussian distributions [117]. These two test statistics are, at a given moment, part of a two dimensional plane of both energy and phase relationship of a acquisition from a frequency channel. Let $\boldsymbol{y}$ be a two dimensional vector of $\mathbb{R}^2$ domain given by,

$$\boldsymbol{y} = (T_e, T_\alpha). \tag{3.37}$$

Assuming a model of two states, at a given n sample the received data is either signal or noise floor. Using the acquired interval data, two clusters can be obtained. The first one, where no signal is present is given by the noise floor energy and a random phase relationship between antennas as each receiving element will have independent noise sources associated to each acquisition RF front-end. The second one, where a signal is being received, where the energy is that signal received power and the phase relationship will given by Equation 3.33. Each of these clusters can be modeled by two 2D Gaussian distributions with the EM method.

3.4.1.3 EM algorithm for two dimensional data

In this spectrum sensing model it is assumed that a long segment of data samples is formed by the concatenation of sub-segments where either there is a user using the channel or only noise is present. Therefore, $\boldsymbol{y}$ can be approximated by 2D Gaussian distributions, the suitable model for the probability distribution function will then be the 2D GMM. The mean of each Gaussian will then represent either a user or the noise floor. The noise floor is expected to be the Gaussian will the lowest estimated mean.The EM algorithm is then used to estimate unknown parameters of the 2D GMM.

Given a set of observations, the EM algorithm aims to compute the maximum likelihood estimation of the unknown parameters of a statistical model. Hence, the available data is assumed to be a set of observations drawn from a mixture of different probability distributions[118]. For the energy estimator we consider the data modeled by a GMM explaining each data point $\boldsymbol{y}$ as follows,

$$m(\boldsymbol{y}|\Theta) = \sum_{k=1}^{K} \pi_k \mathit{\Phi}_k(\boldsymbol{y}|\theta_k) \tag{3.38}$$

where $\Theta = \{\theta_1, \theta_2 \ldots \theta_K, \pi_1, \ldots \pi_K\}$ denotes the set of all parameters of the K normal distributions, with normal density given by $\mathit{\Phi}_k$ and π_k its the weight of each distribution for the data $\boldsymbol{y}$. The weights are constrained to sum to one, e.g $\sum_k \pi_k = 1$. The normal density of each distribution is characterized by the parameters $\theta_k = \{\boldsymbol{\mu}_k, P_k\}$ where $\boldsymbol{\mu}_k$ is the mean and P_k the covariance matrix.

The algorithm starts with initial guesses for each unknown parameter of the Θ set. A common way to set up the initial values is to choose K random samples from the data points for the means $\hat{\mu}_k$ and the overall data covariance as the initial value for P_k. For the parameters $\hat{\pi}_k$ an equal proportion, $1/K$, can be initially attributed for each distribution.

After the initial guesses, the algorithm proceed by recursively applying the following two steps:

- **Expectation step**: For each data value, compute the *posteriori* probabilities of belonging to each distribution given the parameters of the mixture model. Using the Bayes rule the probability that each data value, $\boldsymbol{y}_i, i = 1, 2, ..., N$, belongs to each $\mathit{\Phi}_k(.)$, also called *responsibilit*y, is given by

$$\hat{\gamma}_{k,i}(\mathit{\Phi}_k|\boldsymbol{y}_i) = \frac{\hat{\pi}_k \mathit{\Phi}_k(\boldsymbol{y}_i|\theta_k)}{\sum_{l=1}^{K} \hat{\pi}_l \mathit{\Phi}_l(\boldsymbol{y}_i|\theta_l)} \tag{3.39}$$

- **Maximization step**: The probabilities estimated on the expectation step are integrated in the maximum likelihood estimation of parameters of the normal distributions [111]. Therefore, the updates depend on the weighted values. The aim of the maximum likelihood estimation is to compute the parameters Θ that give the best fit to the given set of independent data observations.

$$\hat{\boldsymbol{\mu}}_k = \frac{\sum_{i=1}^{N} \hat{\gamma}_{k,i} \boldsymbol{y}_i}{\sum_{i=1}^{N} \hat{\gamma}_{k,i}} \tag{3.40}$$

$$P_k = \frac{\sum_{i=1}^{N} \hat{\gamma}_{k,i}(\boldsymbol{y}_i - \hat{\boldsymbol{\mu}}_k)(\boldsymbol{y}_i - \hat{\boldsymbol{\mu}}_k)^T}{\sum_{i=1}^{N} \hat{\gamma}_{k,i}} \tag{3.41}$$

$$\hat{\pi}_k = \sum_{i=1}^{N} \frac{\hat{\gamma}_{k,i}}{N} \tag{3.42}$$

The expectation step and maximization step are iterated until the convergence criteria is met. As output the algorithm gives the estimation of the mean value, covariance matrix and mixture proportion of each normal distribution on the analysed data model.

3.4.1.4 Implementation of hybrid phase relationship and energy detection

It is expected that the $\boldsymbol{y}$ data follows a two multivariate normal distribution, as such, the EM Algorithm is applied for a GMM of two 2D Gaussian distributions. When the EM converges to the maximum likelihood solution the weight of each distribution π_k, on the data $\boldsymbol{y}$ is then used to determine the probability of a data point to belong to either the signal or noise floor subspaces. The π_k is then used to decide the occupation of the channel as seen in Figure 3.22.

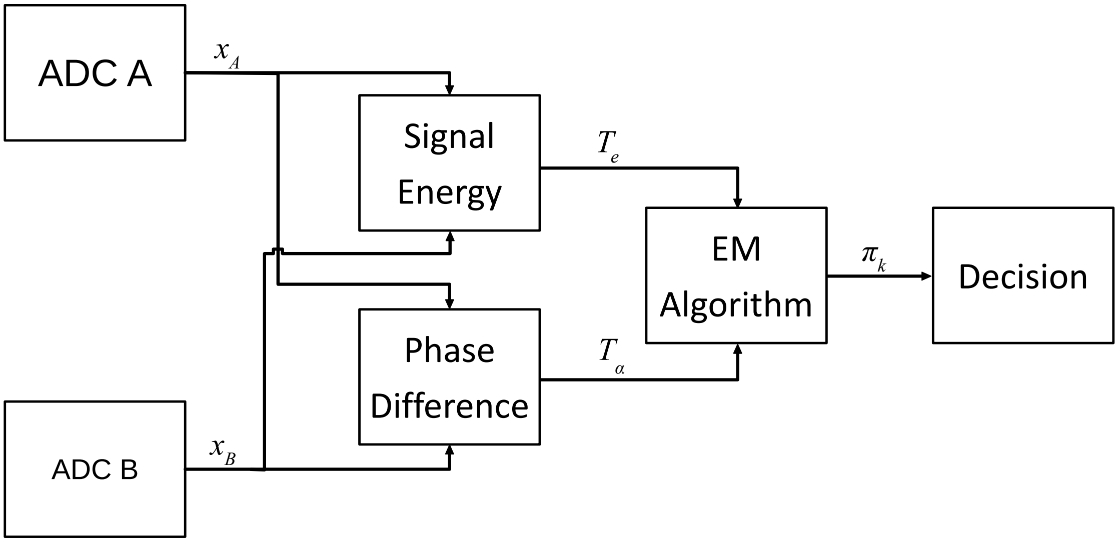

Figure 3.22: Purposed detection method diagram.

3.4.2 Practical experiment for evaluation of the hybrid detection method

The purposed detection method was then evaluated in laboratory using a USRP B210 [119] SDR as a dual receiver RF front-end that is controlled by a personal computer. The B210 SDR is based on the AD9361 [120] that allows synchronous acquisition of two RF channels. The two receivers ports used in this experiment are A:RX2 and B:RX2 that are 2.5 cm separated apart. As the transmitting signal half-wavelength is higher than the separation between receiving elements, ambiguity in the phase difference measurements between the antenna elements is avoided. Both ports are connected to two omni-directional VERT2450 antennas able to operate from 2.4 to 2.48 GHz and 4.9 to 5.9 GHz. The selected central frequency for this experiment was $f_c = 5.3\,\text{GHz}$ that is part of the U-NII radio band [121].

The USRP will be synchronously sampling the signal coming from both antennas at 2 MSPS. The transmitter will be is a R&S SMU200A [122] Vector Signal Generator connected to a 24 dBi horn antenna as shown in Figure 3.23.

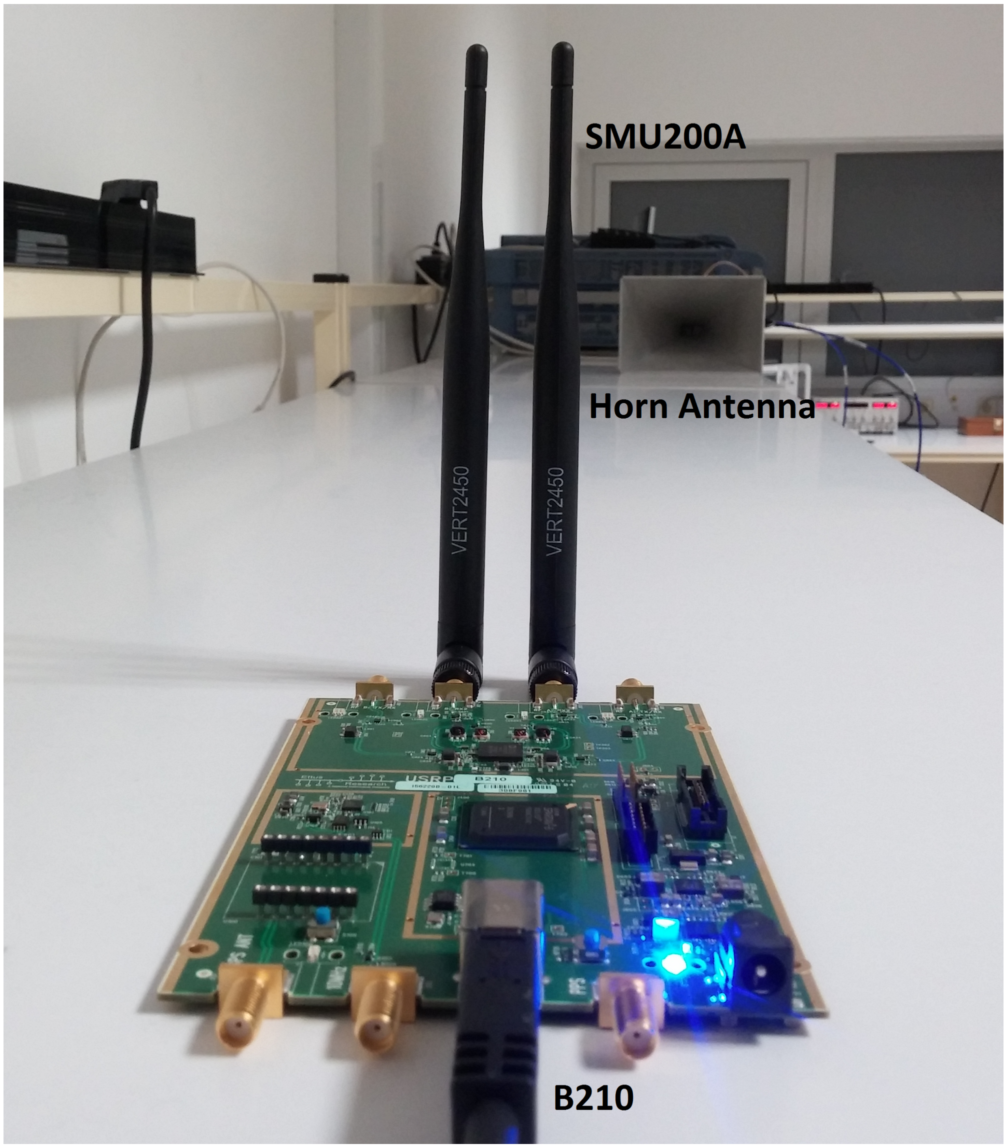

Figure 3.23: Experimental setup for the purposed hybrid detection method evaluation.

The generator transmits a 16-QAM modulated signal, with bandwidth of 0.4 MHz and centered at $f_c + \triangle$, with $\triangle = 300\,\text{kHz}$. This frequency offset of $\triangle$ allows to overcome the leakage of the USRP local oscillator that will be part of the receiving signal when using a heterodyne receiver. This signal is transmitted trough the air with a duty-cycle of 10% where during 0.2 s the signal is on and during 1.8 s the signal is off. The received signal spectrogram can be seen in Figure 3.24.

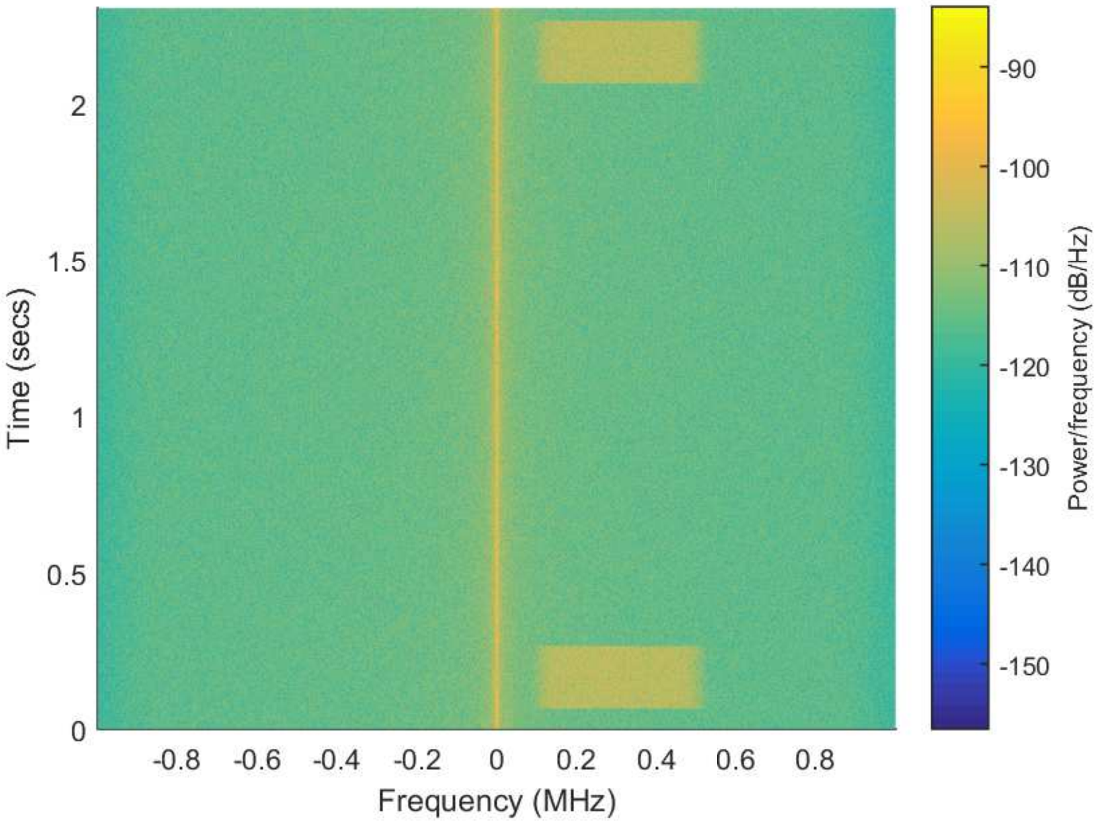

Figure 3.24: Spectrogram of the signal received at the SDR with 15 dB of SNR.

The transmitted power was then reduced in order to have a SNR of -10 dB at the receiver. The acquired data at this SNR is then analysed with the proposed EM algorithm and the results of the cluster segmentation can be seen in Figure 3.25.

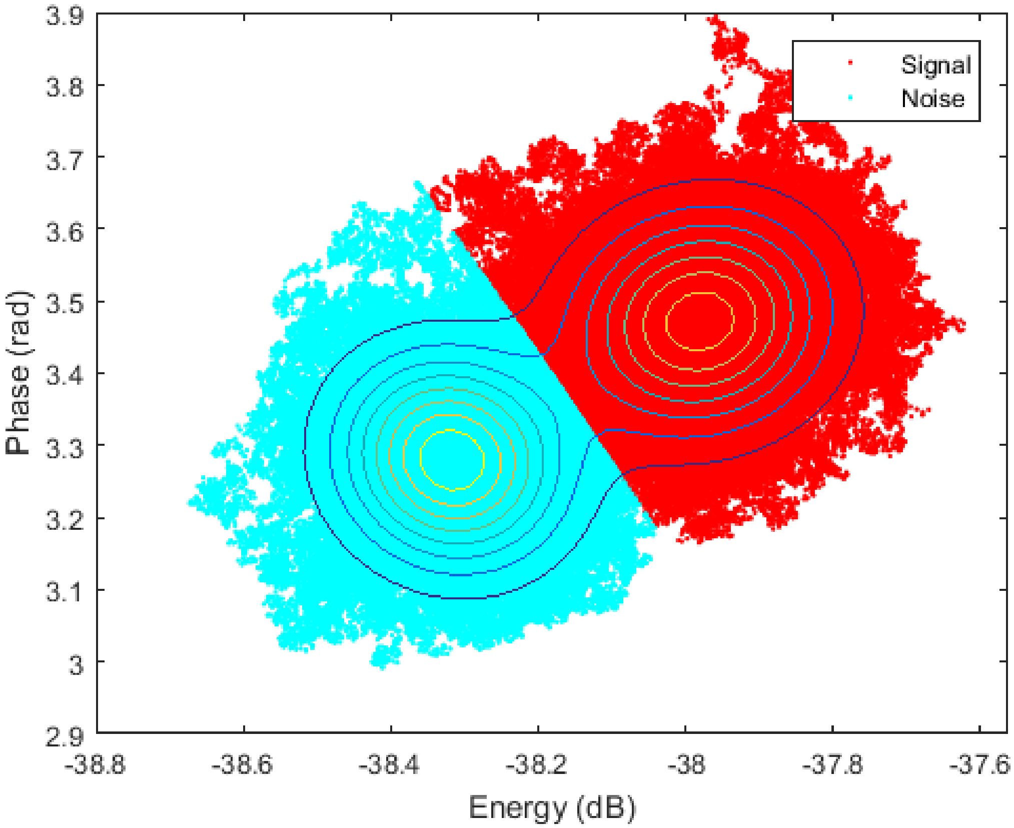

Figure 3.25: Clusters segmentation of the received signal.

The EM algorithm is then able to determine the two centroids, the mean value of both are $\boldsymbol{\mu}_{noise}$ =[-38.3 , 3.28] and $\boldsymbol{\mu}_{signal}$ =[-37.95 , 3.49]. The data classification decision is obtained from the weight of each distribution π_k. The blue points are determined to belong to the noise distribution and the red ones from the detected signal.

3.4.3 Performance evaluation

In order to analyze the performance of the purposed detector, based on the EM method, three ROC curves were calculated using the *a priori* knowledge of the duty cycle of the signal. This allows to exactly know the time slots in which the transmission is active or only noise floor is present. The calculated ROC curve for the classical energy detection uses the T_e test variable where only the combination of the energy of both antennas is used to detect the signal. A phase relationship based detector uses the phase relation test variable T_α to determine the existence of transmission. The purposed method for detection uses both T_e and T_α test variables in a two dimensional space and the 2D GMM is extracted with the EM method to determine when the transmission is present.

From the analysis of each method test variables using a sliding threshold, the ROC curves of each are calculated and plotted at Figure 3.26 for the SNR of $-10\,\text{dB}$.

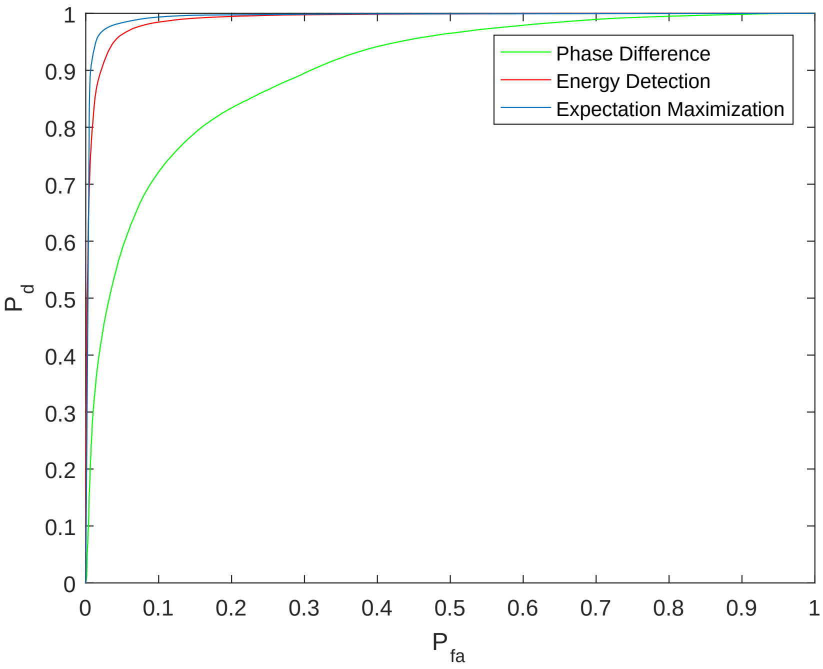

Figure 3.26: Comparison of the ROC curves for a $-10\,\text{dB}$ SNR signal.

The determined ROC curves shows that the worst performance was from the phase difference method where only the phase relationship test variable T_α was used. It is followed in performance by the energy detection method that used the energy test variable T_e . The best ROC curve is then the purposed EM method detection scheme using the two dimensional test variable $\boldsymbol{y}$.

3.4.4 Results discussion

A method for signal detection in a dual-antenna SDR based system using both energy and phase relationship test variables was purposed. This method uses the estimation of both energy and phase relationship and with the EM algorithm classifies the samples in noise and signal. The proposed method was tested in laboratory using as setup a B210 SDR with two receiving elements. The results show that the proposed method was able to detect the RF transmission with a better performance, than the traditional energy detection method.

Chapter 4

Spatial Spectrum Sensing

4.1 Introduction

The 3GPP release 7 [123], MIMO was introduced in mobile networks. Currently, LTE allows up to 8x8 MIMO [124]. The introduction of an even larger number of antennas, as massive MIMO arrays, is currently being discussed [32]. Multiple antenna usage allows beamforming transmissions supporting highly directional communications. Therefore improving radio link performance in comparison with an omnidirectional transmission.

A similar trend happens for Wi-Fi, that from 802.11n standard also allows MIMO communications. Initially only 4x4 MIMO implementations were supported but the current 802.11ac standard supports up to 8x8 [125]. With the expected increase in MIMO utilization and beamforming implementations, the determination of the angle of arrival of these directional RF transmissions will become of key importance.

The main goal of spectrum sensing is to determine the time occupation of the RF spectrum. This knowledge of which frequency channels are currently vacant can then be used by a Cognitive Radio to transmit data. This opportunistic spectrum usage allows a more efficient utilization of the spectrum in comparison with a fixed channel allocation [4]. Due to the progressive usage of highly directional RF communications, additional spectrum opportunities could be identified by determining also the DoA of the detected transmissions. As these transmissions are limited in space by using a very directional beam, it gives arises to the opportunity of reusing the same frequency resources in other directions. The detection of these opportunities is called Spatial Spectrum Sensing and it works by detecting free spectrum resources in three dimensions: frequency, time and space [126]. Compared to traditional spectrum sensing an extra spacial dimension is used to identify additional transmission opportunities by sensing the DoA of the received signals.

In this chapter, we will discuss the implementation of a spatial spectrum sensing system. In the proposed system the frequency occupation analysis is done by calculating the phase relationship between two receiver antennas. The relative phase measurement is estimated for each frequency channel of the received signal's spectrum that is segmented using a digital filter bank. This multiple antenna system allows to determine the frequency occupation without the need of a noise floor estimation, while also calculating the DOA of the received signal. Thus allowing to sense the three different domains needed to implemented a system that allows spatial spectrum sensing.

4.2 DoA estimation

The DoA describes the direction from which an RF signal is received [127]. In a receiver with an antenna array, the DoA is calculated by measuring the phase difference between the signal acquired by the individual antennas. The difference in propagation distances from the transmitted signal to the individual receiving antennas implies differences on the phase between the received signals. Each antenna receives then the same original RF signal but with a different phase shift. Assuming a two antenna receiver array and in a far-field case, where is assumed that the wave propagates in parallel through space [116], we have the same scenario illustrated in Figure 3.21. In this scenario the transmitted RF signal s arrives to two antenna elements with a path length difference l that can be obtained from,

$$l = d \sin\theta \tag{4.1}$$

where d is the distance between the two receiver antennas and θ the DoA of the incoming wave.

The phase difference α between the acquired signal from the two receiving elements can be expressed by,

$$\alpha = \frac{2\pi}{\lambda} l \tag{4.2}$$

where λ is the wavelength of the incoming wave. By replacing the path length difference l, in Equation 4.2, the DoA is then obtained by,

$$\theta = \sin^{-1}\left(\frac{\alpha}{2\pi d/\lambda}\right). \tag{4.3}$$

In a dual-antenna system, the phase difference can be calculated using the inner product of the two antenna received data. Assuming that $x_A(n)$ and $x_B(n)$ are the complex sampled signal from respectively, the first and second antenna and by ignoring reflections and propagation losses we have,

$$\begin{cases} x_A(n) = s(n)e^{j\Phi_A} \\ x_B(n) = s(n)e^{j\Phi_B} \end{cases} \tag{4.4}$$

where Φ_A and Φ_B is the received signal phase. The inner product of both received signal is given by,

$$x_A(n)x_B^*(n) = s^2(n)e^{j(\Phi_A - \Phi_B)} \tag{4.5}$$

Where * indicates the complex conjugate. The angle of this inner product will then give the phase relationship between the two antennas,

$$\begin{aligned} \alpha(n) =& \Phi_A - \Phi_B \\ =& \angle[x_A(n)x_B^*(n)] \end{aligned} \tag{4.6}$$

where $\angle$ denotes the phase angle of the complex value.

4.3 Constant false alarm rate using phase coherence

In a multiple antenna system, it is expected that each one of the antennas will receive the same signal but with different phase delays. These different delays originate due to the different path lengths from the transmitter to the antenna elements. It can then be assumed that in the presence of a transmission, the received signal from each antenna will be correlated. On the other hand, in absence of transmission the signals acquired from each receiver front-end will only contain noise floor. The latter are independent between receivers as they are uniquely generated by each RF chain receiver. A detection methodology based on phase coherence between antennas will then circumvent the need for a dynamic estimation of the noise floor power, as it will based on the distribution analysis of the phase measurements.

Let us assume a dual antenna receiver where each antenna element has its own RF chain and with a phase relationship between antenna elements given by Equation 4.6. The RF spectrum sensed by each antenna is divided in multiple frequency bands, where each may be vacant H_o or occupied H_1. By ignoring propagation loss and assuming a narrow-band transmitted signal (where the bandwidth is much smaller than the carrier frequency), the scenario can be modeled by,

$$\begin{aligned} x_A(n) &= \begin{cases} w_A(n), & H_0 \\ s(n)e^{j\alpha} + w_A(n), & H_1 \end{cases} \\ x_B(n) &= \begin{cases} w_B(n), & H_0 \\ s(n) + w_B(n), & H_1 \end{cases} \end{aligned} \tag{4.7}$$

where $x_A(n)$ and $x_B(n)$ are the discrete received time signals from each antenna. Each element RF chain, has an independent noise floor that is represented by $w_A(n)$ and $w_B(n)$. The transmitted signal is given by $s(n)$ and the path length difference between elements generates a phase shift of α between each antenna.

If a signal is present (H_1), both receivers acquire a correlated signal. In this case, there is information on the phase difference between x_A and x_B. Assuming that the phase measurement is affected by Gaussian noise, the phase relationship will have a normal distribution with a mean value contained in the interval $[-\pi, \pi]$ and a variance that is proportional to the correlation between both signals.

If no signal is present (H_o), then the phase difference between the received signal from each antenna have a random value due to the independently generated noise floors [128]. With the absence of signal, a maximum entropy probability distribution is to be expected [129]. In this case, the phase relationship is modeled by a uniform distribution bounded by $[-\pi, \pi]$ [130]. By the uniform distribution properties, the expected mean value will be zero and the variance [131] is,

$$\sigma_u^2 = \frac{1}{12}(2\pi)^2. \tag{4.8}$$

The variance of the phase difference can then be used as a test variable to determine the presence, or absence, of a transmission in a given frequency band. For this purpose a sliding unbiased estimator, of order N, for the sample variance is proposed. The variance estimator can be described by the following equation,

$$\hat{\sigma}_N^2 = \frac{1}{N-1}\sum_{j=1}^{N}(\alpha_j - \bar{\alpha}_N)^2. \tag{4.9}$$

Where N is the number of samples used for the variance estimation. By using an unbiased estimator the expected value of the estimator will be in fact the data variance. The variance of the sampled variance estimation, $\hat{\sigma}_N^2$, can be given by [99],

$$\mathrm{var}[\hat{\sigma}_N^2] = \frac{1}{N}(\mu_4 - \frac{N-3}{N-1}(\sigma_u^2)^2). \tag{4.10}$$

where μ_4 is the fourth central moment. Assuming that no signal is present, the fourth central moment of the uniform distribution is given by [131],

$$\mu_4 = \frac{1}{80}(2\pi)^4. \tag{4.11}$$

By the Cochran's theorem [132] the variance of sampled variance estimation $\hat{\sigma}_N^2$, follows a scaled chi-squared distribution of $(N-1)$ order. Assuming a high order N, this distribution can be approximated to a Gaussian distribution [117]. For H_o the moving variance output can be modeled by the normal distribution,

$$\hat{\sigma}_N^2 \sim \mathcal{N}(\sigma_u^2, \mathrm{var}[\hat{\sigma}_N^2]). \tag{4.12}$$

Having determined the sampling variance estimator PDF, we can then implement a CFAR detector [75]. This is done by defining a fixed probability of false alarm (P_{fa}) and as the noise expected value and variance are of a know value for a fixed N, the threshold can be determined to obtain a constant P_{fa} as seen in Figure 4.1.

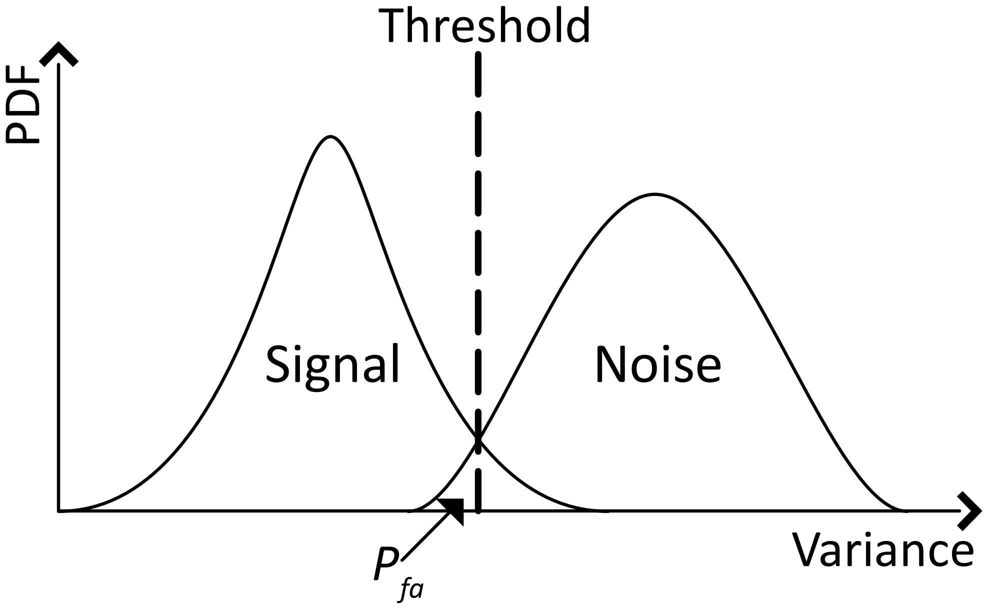

Figure 4.1: Threshold decision effect on the probability of false alarm.

As under noise the variance estimator output is modeled with a Gaussian distribution, under the Neyman-Pearson criterion the threshold γ can be calculated [100] by,

$$P_{fa} = Pr[\hat{\sigma}_N^2 < \gamma] = Q\left(-\frac{\gamma - \sigma_u}{var(\hat{\sigma}_N^2)}\right) \tag{4.13}$$

where Q is the tail probability of the standard normal distribution. The threshold, γ, is then be given by,

$$\gamma = -Q^{-1}(P_{fa})\mathrm{var}[\hat{\sigma}_N^2] + \sigma_u^2. \tag{4.14}$$

The calculated threshold will then be used to differentiate between noise and signal from the output of the unbiased sample variance estimation for each frequency channel.

4.4 Uniform DFT Polyphase Filter Banks

The analysis filter bank is a widely used method to segment a sampled RF signal into frequency channels. An analysis filter bank is an array of band-pass filters that divide the input signal into various components, each one containing a frequency band of the original input. The filter bank prototype FIR filter has the following coefficients $h(n) = [h(0), h(1) \dots h(C-1)]$, with C being the filter order. This prototype filter is then translated in frequency to obtain all the filter bank outputs. As the number of coefficients can be larger than the number of frequency bins, the analysis filter bank will have an extensive freedom to design sharp filters based in, for example, a window function [133].

For an efficient application, the analysis filter bank can be implemented by using a DFT after a polyphase decomposition of both the input data and the prototype filter. Assuming a M channel filter bank, this is achieved by using a decimation by M and by also decomposing the prototype filter in M phases $H_k(z), k = 0, \dots, (M-1)$. Where $H_0(z), H_1(z), \dots H_M(z)$ represent the polyphasic components of the prototype filter.

The M channels analysis filter bank will have a $G_k(z)$ transfer function, where $k = 0, \dots, (M-1)$, correspond to the modulated prototype filter $H(z)$ and is expressed as [133]:

$$G_k(z) = H(ze^{j\frac{2\pi k}{M}}), k = 0, 1, ..., M-1 \tag{4.15}$$

This implementation is based on the the division of the prototype filter in its various channels, $H_k(z)$, and is given by,

$$H_k(z) = \sum_{n=0}^{C/M-1} h(nM+k)z^{-n} \tag{4.16}$$

assuming that C is a multiple of M, the $C/M - 1$ gives the number of coefficients for each phase of the polyphasic filter.

The practical implementation of the filter bank will use a Hann window function to generate the FIR prototype filter. The usage of the Hann function allows good rejection rates outside the band of interest while with a trade-off of a slightly decreased resolution [134].

4.5 Phase Coherency Spectrum Sensing

4.5.1 System overview

The proposed spectrum sensing system is based on the phase coherence between the received data from two synchronous receiver front-ends, each with its own antenna element. The functional block diagram of this system is shown in Figure 4.2.

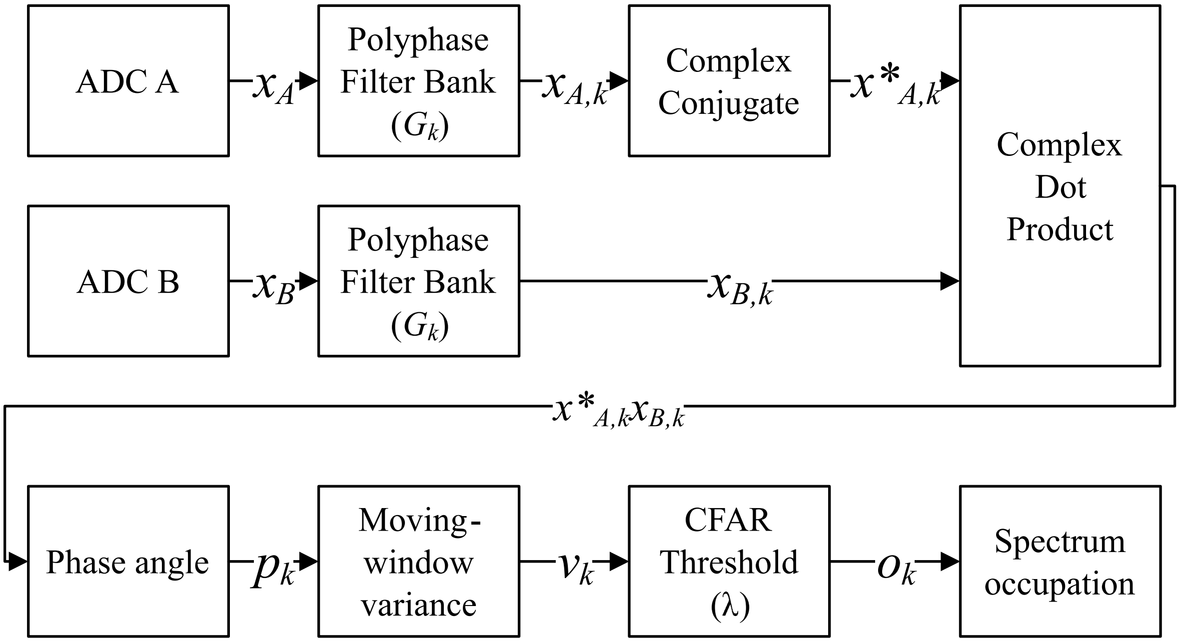

Figure 4.2: Diagram of the phase coherence spectrum sensing system.

The data acquired from the two ADC x_A and x_B is segmented into $k = 1, \ldots, K$ frequency bands using a uniform DFT polyphase filter bank (G_k), while each channel has it own filter bank both have the same coefficients [133]. The filter bank outputs ($x_{A,k}$ and $x_{B,k}$) are used to obtain the phase difference between antennas by obtained with Equation 4.6. To obtain this relationship, the phase angle (p_k) of the complex dot product is calculated using the complex conjugate of the ADC A data ($x^*_{A,k}$) values. To obtain the sample variance (v_k) of the resulting phase relationship, a moving-window sample variance estimation is used as given by Equation 4.9. The threshold (γ) is calculated to obtain a fixed P_{fa} and is then applied to the estimated sample variance. The resulting output (o_k) of the CFAR binary decision gives the instantaneous spectrum occupation.

4.5.2 System practical implementation

The described spectrum sensing unit is implemented to evaluate the 5GHz unlicensed spectrum in the U-NII radio band [121]. In the following experiment a central frequency of $f_c = 5.3\,\text{GHz}$ (part of the U-NII-2A band [121]) was used . The distance between antennas is of 2.5 cm, slightly inferior to half wavelength of the incoming signal ($\lambda/2 = 2.83$cm). Equation 4.3 can be used to obtain the DoA from the phase relationship. In this configuration the DoA can be calculated by,

$$\theta = \sin^{-1}\left(\frac{\alpha}{2\pi\frac{2.5}{5.66}}\right). \tag{4.17}$$

The moving-window sample variance, given by Equation 4.9, is implemented using $N = 100$ samples. For this value, in absence of transmission (H_0) the output distribution can be approximated by,

$$\hat{\sigma}_n^2 \sim \mathcal{N}(3.29, 0.089).$$

By knowing the noise distribution the CFAR threshold can easily be calculated by using Equation 4.14. In this implementation a constant false alarm rate of $P_{fa} = 0.1\%$ was defined and for this value the threshold is,

$$\gamma \cong 2.37\text{rad}$$

For the analysis filter bank, the prototype impulse response $h(n)$, was defined with 5000 coefficients. As the number of channels in this setup is $M = 500$, the number of coefficients for each polyphasic filter channel is of 10. The implemented filter bank frequency response can be saw in Figure 4.3.

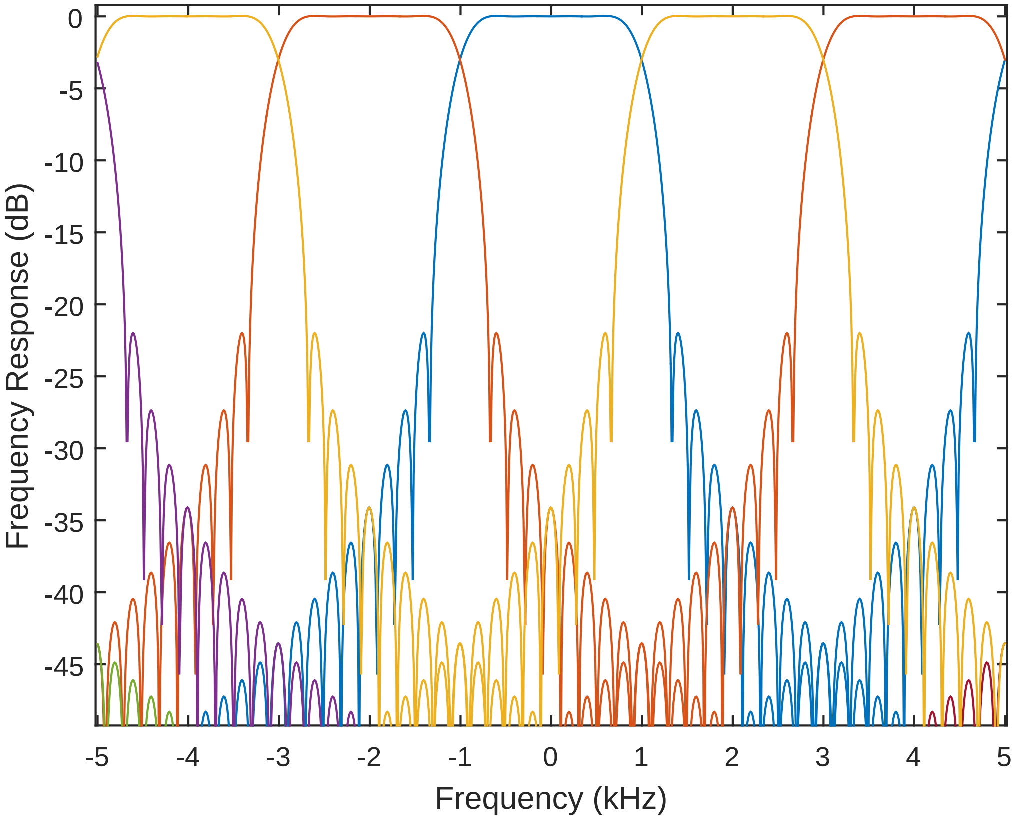

Figure 4.3: Frequency response of the central five filters of the filter bank.

The real-time analysed bandwidth is of $B_W = 1\,\text{MHz}$, as the filter banks are implemented with 500 channels then the original signal bandwidth is segmented in 2 kHz bands.

4.6 Experimental evaluation

The implementation of the purposed method is done using a USRP B210 [119] SDR controlled by a personal computer. The B210 RF front-end transceiver is largely based on the AD9361 RF integrated circuit [120] that allows synchronous acquisition of two RF channels. The two receivers ports used are A:RX2 and B:RX2 that are separated by a distance of 2.5 cm. Both ports are connected to two omni-directional VERT2450 antennas able to operate from 2.4 to 2.48 GHz and 4.9 to 5.9 GHz, ranges that include the selected central frequency for the experiment, of $f_c = 5.3\,\text{GHz}$. Each ADC will be sampling In-phase and Quadrature (I/Q) at 1 Msps.

4.6.1 Phase calibration

A phase calibration scheme is of paramount importance to obtain a accurate phase relationship. To do it, a power splitter, with a known frequency response, is used to feed the receivers with the same reference signal and its frequency response was evaluated using an network analyser. The selected power splitter was a Mini-Circuits ZN2PD-9G-S+ [135] and it frequency response was evaluated using an Agilent N5242A PNA network analyzer [136].

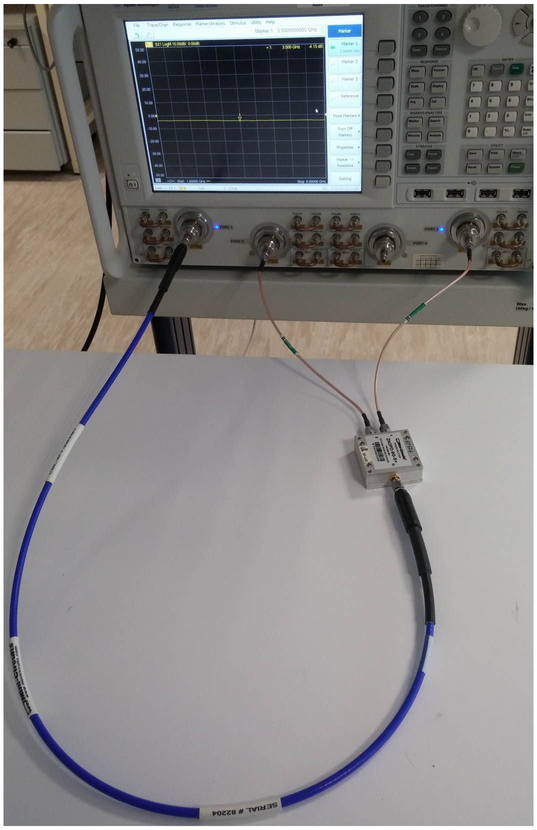

Figure 4.4: Characterization of the power splitter with a Network Analyzer.

This characterization was done in order to obtain the S-parameters of the splitter together with two cables with SubMiniature version A (SMA) connectors that interface with the RF receivers on the SDR. With the acquired frequency response, the phase unbalance of both receivers can be latter digitally compensated. This compensation guarantees that the relative phase between inputs in our SDR will be phase calibrated. The splitter setup was determined to have a relative phase unbalance of 0.99^o, between the power splitter setup outputs, for the selected central frequency as visible in Figure 4.5.

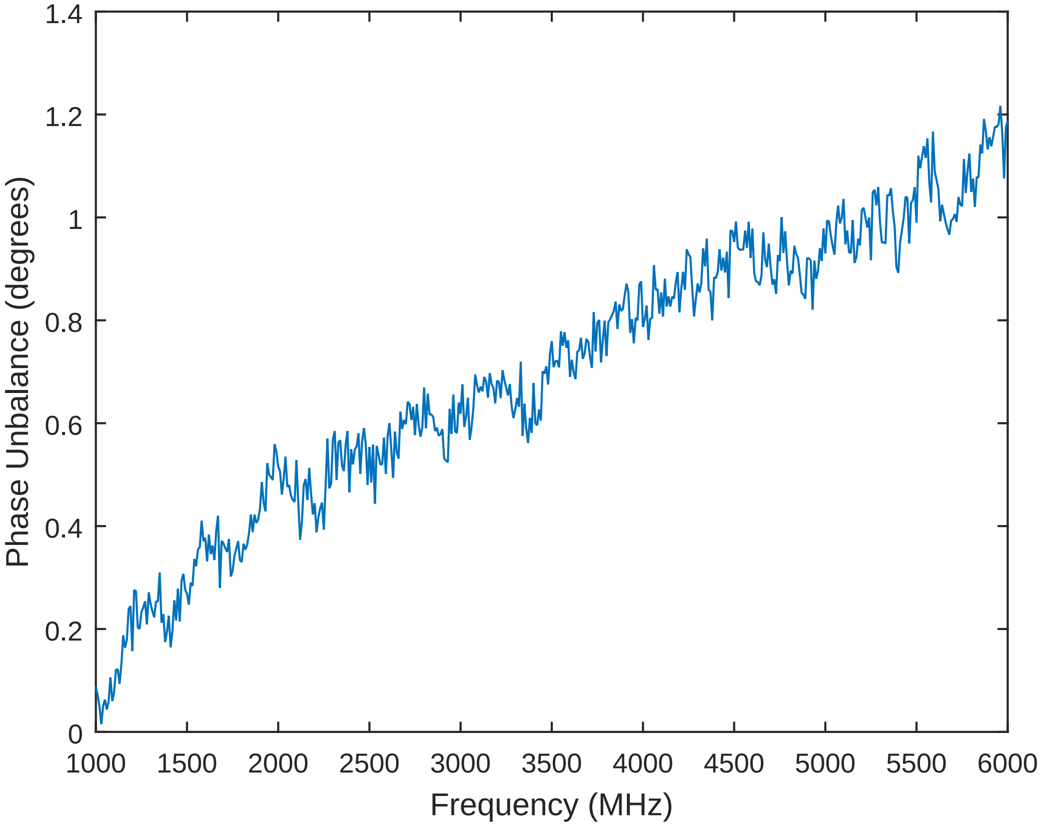

Figure 4.5: Phase unbalance characterization of the power splitter outputs.

After characterization of the power splitter phase imbalance, this setup is used to evaluate the phase relationship between the SDR inputs. For this measurement the USRP is connected to the splitter and is tested with a frequency sweep generated from a R&S SMU200 Vector Signal Generator (VSG) [122].

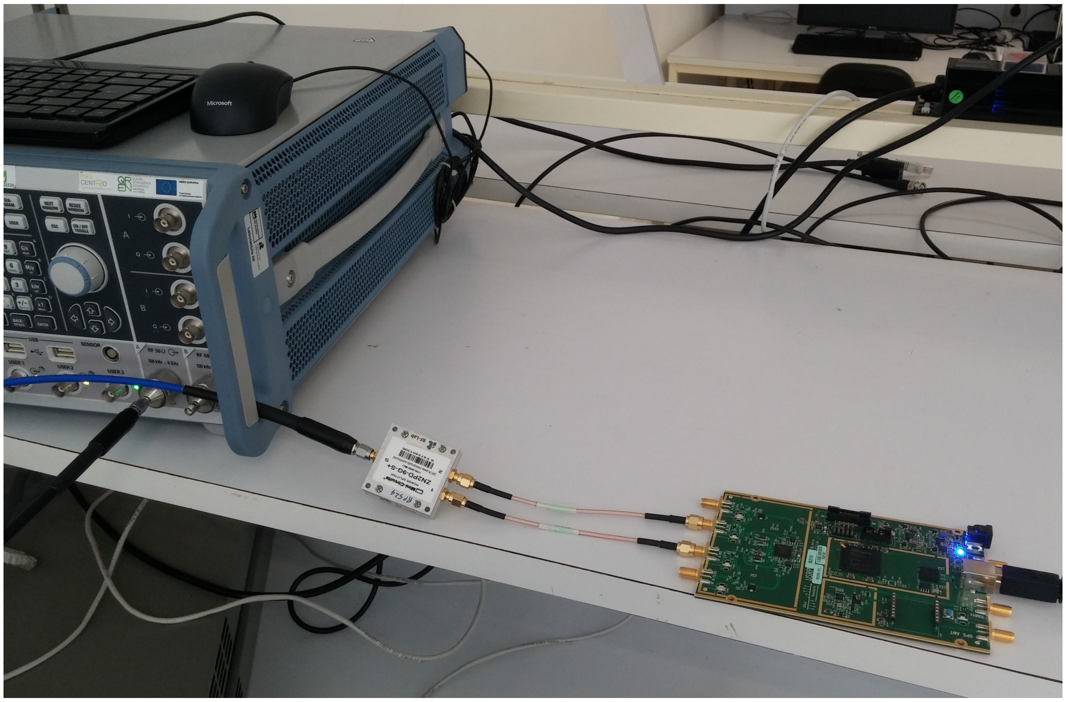

Figure 4.6: Analyzing the phase imbalance of the receiving unit.

The obtained result show a phase imbalance of 7.03^o between both SDR RX channels for a operating frequency of 5.3GHz, this value already takes into account the previous splitter setup calibration results. The obtained value of phase imbalance will then be digitally compensated in the next experiments.

4.6.2 DoA evaluation

In order to evaluate the DoA estimation accuracy of the proposed system, measurements were made at a RF anechoic chamber. The used anechoic chamber positioners have an angular resolution of 0.01^o and the RF probe is at a distance of 4.5m from the system under test. The SDR is deployed with both antennas positioned perpendicularly to the direction of emission as visible in Figure 4.7.

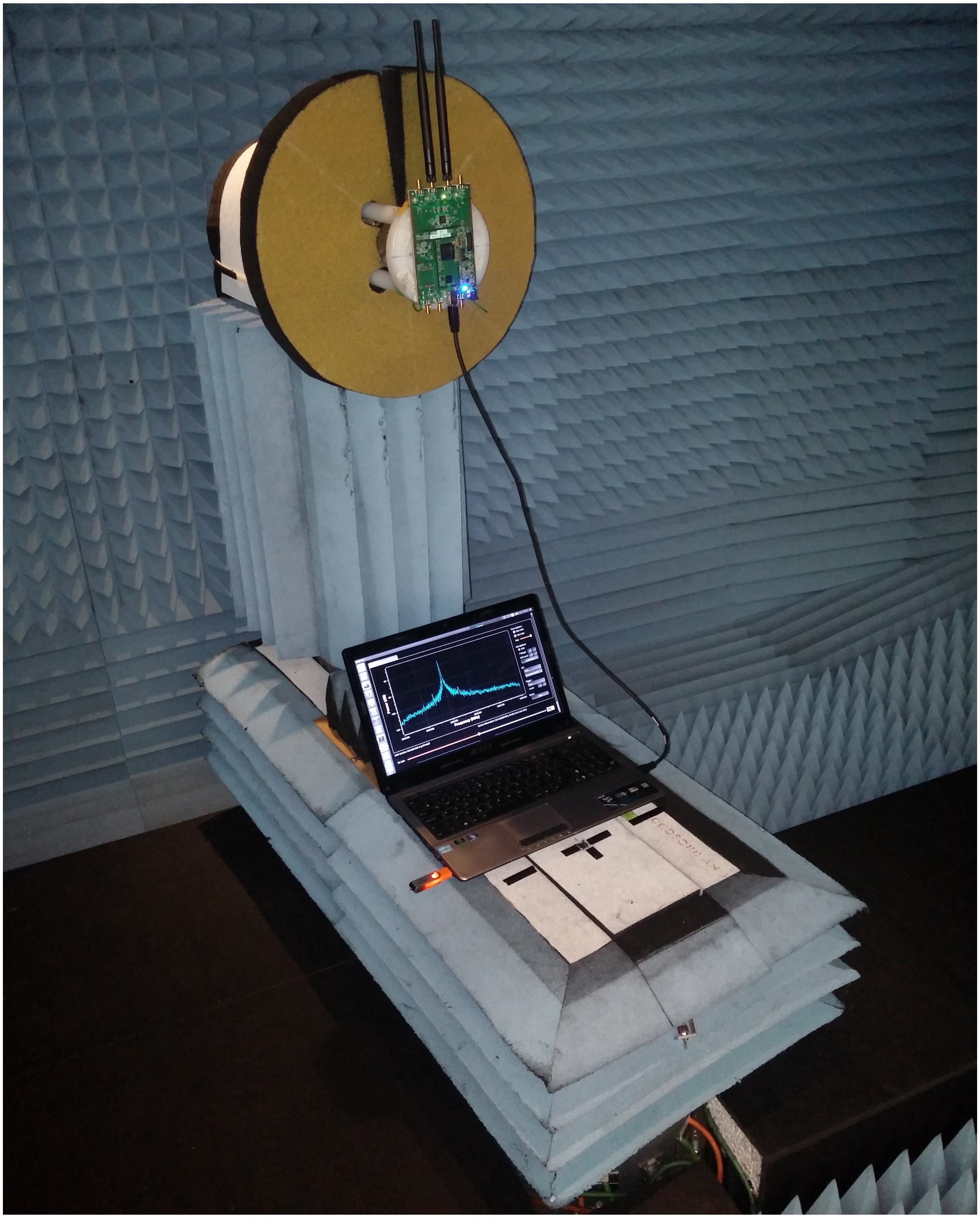

Figure 4.7: DoA evaluation in the anechoic chamber.

During the evaluation, the azimuth positioner sweeps from -90^o to 90^o relatively to the transmitting antenna in 5^o steps. This probe is transmitting a CW consisting in a sinusoidal wave centered at 5.3 GHz+$\triangle$, where $\triangle = 5$kHz is an induced offset to avoid the DC blocking circuitry of the SDR. The acquired data from the USRP is used to estimate the DoA using Equation 4.17, the results are plotted in Figure 4.8.

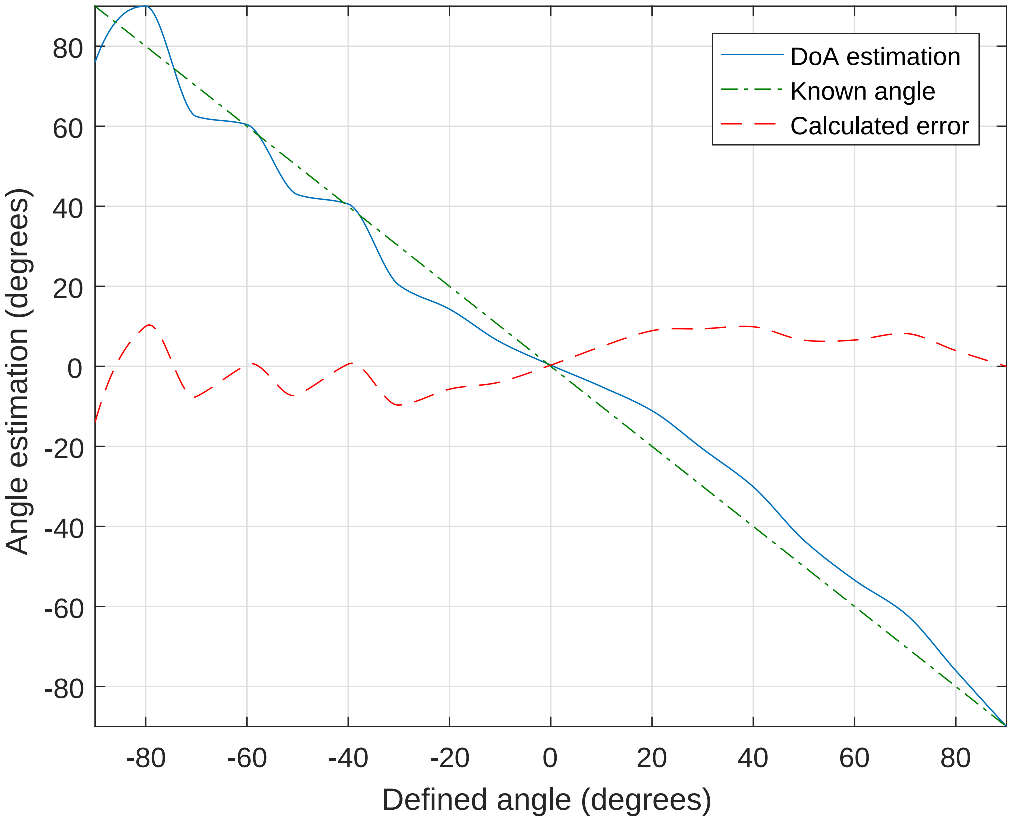

Figure 4.8: Results of the DoA estimation in the anechoic chamber.

These results show the possibility of using the proposed system for DoA estimation of an incoming signal. The calculated estimation mean absolute error is of 6.1^o.

4.6.3 Two transmitters experiment

To evaluate the feasibility of the proposed system to sense simultaneous transmissions, a scenario with two transmitters was implemented. The transmitters used in the setup are two SMU200 VSG connected to two horn antennas as described in Figure 4.9.

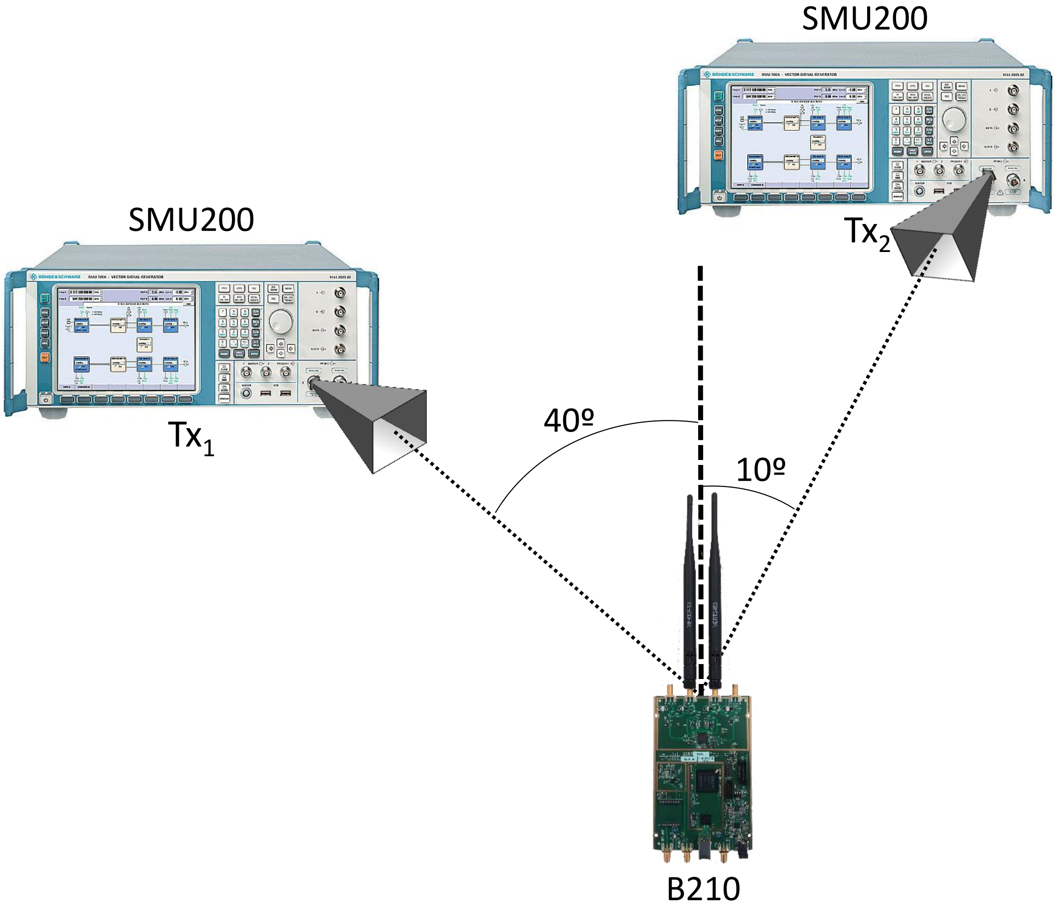

Figure 4.9: Diagram of the experimental setup.

Each generator transmits an independently generated random 16-QAM modulated signal that is filtered with a raised-cosine filter with a roll-off factor of 0.1. The Tx_1 VSG is transmitting from the left with an angle of 40^o, with a 100kHz bandwidth centered at $f_c + \triangle_1$, with $\triangle_1 = -250\text{kHz}$, a duty cycle of 75% and it is received at approximately 10dB in-band SNR. The Tx_2 VSG is transmitting from the right with an angle of 10^o, with 300kHz bandwidth centered at $f_c + \triangle_2$, with $\triangle_2 = 250\text{kHz}$, a duty cycle of 25% and it is received at approximately 15dB in-band SNR. Both transmissions are repeated with a period of 1s. To evaluate simultaneous transmission detection, the Tx_2 signal is only present when the Tx_1 is already transmitting. A spectogram and the mean PSD of the received data, on the B:RX2 receiver, are plotted in Figure 4.10.

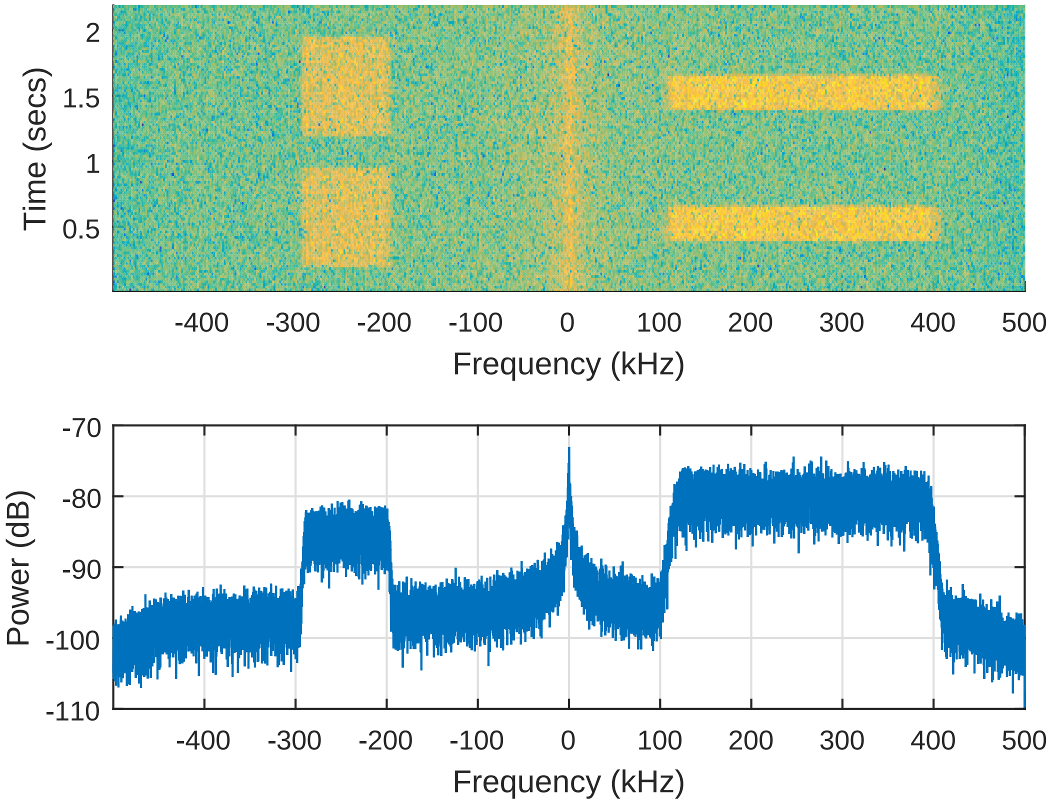

Figure 4.10: On the top the spectogram of the data received on one channel of the B210. On the bottom the instantaneous PSD.

In the spectrogram, both transmitted signals from the SMU200s are visible, as well as the leakage from the LO of the SDR that is DC-centered. The data is then analysed with the proposed phase coherence method described in Figure 4.2 and then compared with a conventional ED. The ED uses $x_{B,k}$, the frequency segmented data from ADC B as it is the one received with the best SNR. The data is multiplied by its complex conjugate and filtered with a moving average that uses the same number of samples as used in the phase coherence algorithm ($N = 100$). To determine the ED threshold we need to have an estimation of the noise floor. For this purpose, the data acquired from a non-occupied band was used, it was selected the $-100\,\text{kHz}$ frequency segment to estimate the noise model. This was done by calculating the channel mean value and variance. With these two parameters the threshold is then obtained by (4.14). The spectrum occupation o_k is then calculated for the two methods and plotted in Figure 4.11.

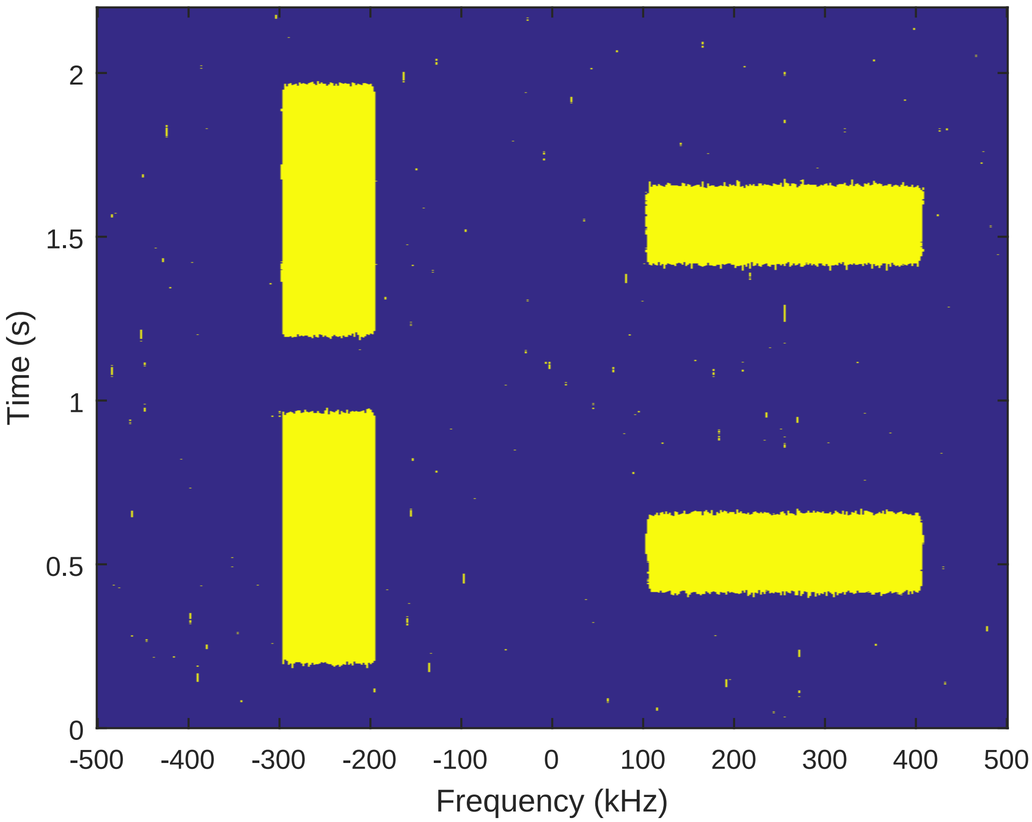

Figure 4.11: Spectrum occupancy results, of the purposed system, through time.

In yellow is plotted the temporal occupation of the spectrum, with is consistent with the generated signals from the VSGs. As expected, the LO leakage and other independent noise sources from the receivers are detected using ED but not detected using the phase coherence method. In addition to the two periodic expected signals, both methods show false alarm, in ED these are focus near DC, due to high power of the LO leakage compared to the received signals. In phase coherence, these are randomly spread in the spectrum occupancy. By calculating the false alarms outside the time-frequency occupation slots, it is obtained a probability of false alarm of 0.12% in the phase coherence, which is consistent with the defined 0.1% CFAR and in the ED 10.38% due to the LO leakage. The analysis of the spectrum occupation, during a period of 1s gives us the results described in Table 4.1.

Signal	$\triangle$ (kHz)	BW (kHz)	Duratio (s)	DoA (degrees)	P_{fa}
Tx_1 (ED)	-242	100	0.297	-	-
Tx_1 (PC)	-243	102	0.253	41.12^o	-
Tx_1 (expected)	-250	100	0.25	40^o	-
Tx_2 (ED)	257	306	0.799	-	-
Tx_2 (PC)	258	304	0.759	-12.06^o	-
Tx_2 (expected)	250	300	0.75	-10^o	-
P_{fa} (ED)	-	-	-	-	10.38%
P_{fa} (PC)	-	-	-	-	0.12%
P_{fa} (expected)	-	-	-	-	0.1%

Table 4.1: Comparison of the expected and practical results of the two detected signals for ED and Phase Coherence (PC).

Even with some error, the system was able to obtain a good DoA estimation. The offset of the calculated bandwidth is explained by the raised-cosine filter roll-off. The error obtained in the central frequency estimation is due to the non-shared clock reference between the VSGs and the SDR LO. The calculated duration of the Tx_1 and Tx_2 signals is lower in the phase coherency method with an error close to 1% and can be attributed to the filter used in energy detection and the order of the used moving variance estimator in PC.

4.7 Discussion of the phase coherence method

The proposed method is capable of detecting spectrum occupation without the need of a noise floor estimation. This method is also capable of determining the bandwidth, duration, central frequency and DoA of multiple incoming signals that are separated in frequency. The full implementation was evaluated with two incumbent signals from different sources that share, at the same time, the RF spectrum. The system was able to estimate the bandwidth, duration, central frequency and DoA of the received signals with good precision. The proposed method was compared with conventional energy detection, showing less P_{fa} by eliminating the LO leakage from the detection, proving the validity and advantages of the phase coherence method.

However, the implementation is done offline. The data is acquired by the SDR and only then the spectrum is sensed for occupation. For a real-time spectrum sensing system the method needs to be implemented directly in a FPGA.

4.8 FPGA implementation of phase coherence detection

4.8.1 Phase coherence hardware design

To achieve a real-time Digital Signal Processing (DSP) unit for spectrum sensing, based on phase coherence detection, a hardware implementation needs to be developed. The most practical solution is to develop the proposed algorithm for a FPGA implementation that will process data from a RF front-end. The sampled data from the ADC, part of the RF front-end, will be processed in a DSP unit that will implement the phase coherence method in the FPGA. This unit contains the necessary hardware to evaluate the variance of the phase difference between the obtained signals from both antenna elements. To obtain this relationship the instantaneous phase angle between the two antennas is to be calculated. Let us assume that $x_A(n)$ and $x_B(n)$ are the complex sampled signal from respectively, the first and second antenna. The argument of the inner product of the antennas will give the phase relationship α,

$$\alpha(n) = \angle[x_A(n) x_B^*(n)]. \tag{4.18}$$

This equation will then be implemented in the FPGA hardware. The conjugate of the signal x_B is calculated by changing the sign of the imaginary part of the data. This can be achieved with a multiplication of the imaginary part by minus one. The product of $x_A(n)$ and $x_B^*(n)$ can be obtained by using a complex multiplier. The argument of a complex number ($\angle$) is given by $\arctan(\frac{imaginary}{real})$ and to obtain it from the previously calculated product a COordinate Rotation DIgital Computer (CORDIC) core can be used to efficiently implement the inverse trigonometric function.

From the obtained phase relationship α , the next step is to implement a sliding unbiased estimator, of order N, for the sample variance. The estimator is described by, the previously given, Equation 4.9 where $\bar{\alpha}_N$ is the sliding mean that uses the last N values of α. This operation is equivalent to [99],

$$\hat{\sigma}_N^2 = \overline{(\alpha_N^2)} - (\bar{\alpha}_N)^2. \tag{4.19}$$

For a FPGA application Equation 4.19 shows a clean visualization of the required hardware implementation of the variance estimator. The implementation can be achieved by using two squaring operations. These squaring operations can be implemented with a multiplier, where the data signal is shared for both inputs of the multiplier block. Equation 4.19 also requires two moving average operations as seen in the complete phase coherence implementation diagram in Figure 4.12.

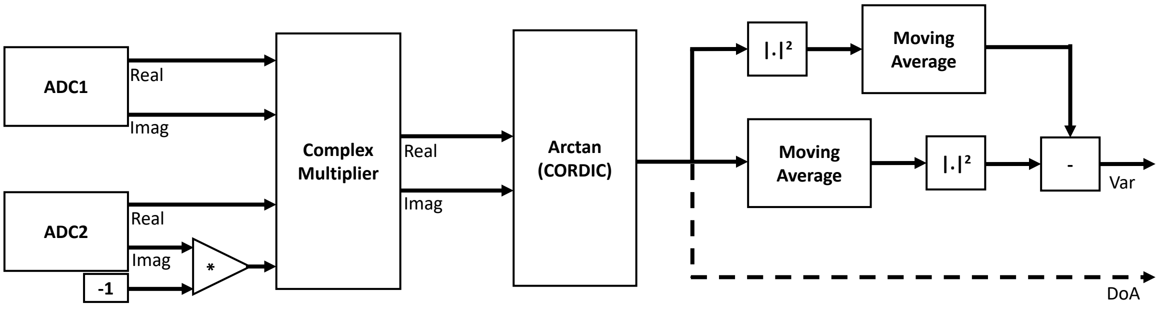

Figure 4.12: Diagram of the phase coherence detection algorithm FPGA implementation.

The moving average is a critical element in this implementation as it needs to be of high order to, by the central-limit theorem, generate a Gaussian distribution output. For this purpose, the moving average can be implemented using a FIR filter that averages a large number of consecutive samples, this leads to a filter with a large number of coefficients. This high order filter, limits a possible implementation in FPGA. In a Xilinx FPGA a typical filter for real-time implementation occupies one DSP slice [137] per filter coefficient.

In this work we will use a XC7Z020 FPGA chip that has available 106400 register cells and 53200 Look Up Table (LUT) but only 220 DSP slices. DSP slices are then a scarce resource when designing the signal processing stage. This makes impratical to implement, for example, two 100-order filters, that would achieve the moving average block, using a FIR IP-Core synthesis. In Xilinx FPGAs these elements are implemented by using a logic core called FIR Compiler. The Xilinx FIR Compiler 7.2 implements the moving average as shown in Figure 4.13.

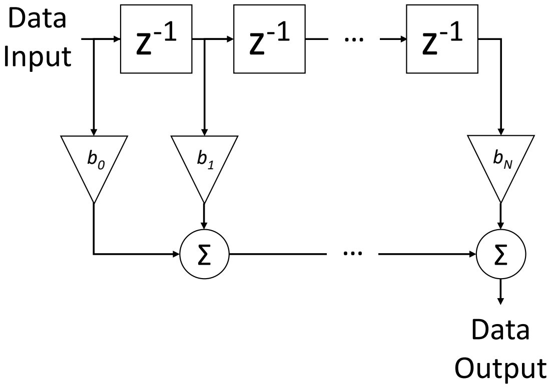

Figure 4.13: Diagram of a FIR filter implementation.

This implementation makes usage of $N+1$ DSP slices that are used as multipliers for the coefficients $b_0, b_{1,}..., b_N$. The filter is used to implement a moving average and each sample will be multiplied with the same coefficient value of $\frac{1}{N}$.

Let us analyse the resource allocation for the phase coherence method from the Figure 4.12 design with the moving averages being implemented using FIR compilers. For this evaluation one hundred order filters are used for the both used moving averages, the resource usage can be seen in Table 4.2 where the elements of the algorithm that use DSP slices are also individually detailed.

	LUTs	Registers	DSP
Resources available in xc7z020	53200	106400	220
2xFIR Compiler	9490	14406	202
2xMultipliers (Square)	2	136	14
Complex Multiplier	2	2	4
Total (With all elements)	13353	18524	220

Table 4.2: FPGA resources of the purposed algorithm by using FIR compilers.

These results are obtained from the synthesis done by Vivado Design Suite 2014.4. Concluding that the implementation of the phase coherence algorithm, using FIR Compiler filters of 100th order, uses all the available DSP on the FPGA. The used filter architecture leaves no DSP resources for the rest of the needed FPGA implementation. Due to that other alternative architectures, instead of using the FIR compiler design for the moving average implementation, were then analysed.

The first evaluated alternative solution was based on a shift register, where the outputs of a delay chain are summed and the result is then divided by the order number of the filter. This parallel sum based implementation does not require the usage of any DSP slices and is detailed in the example from Figure 4.14 for a 128 order moving average.

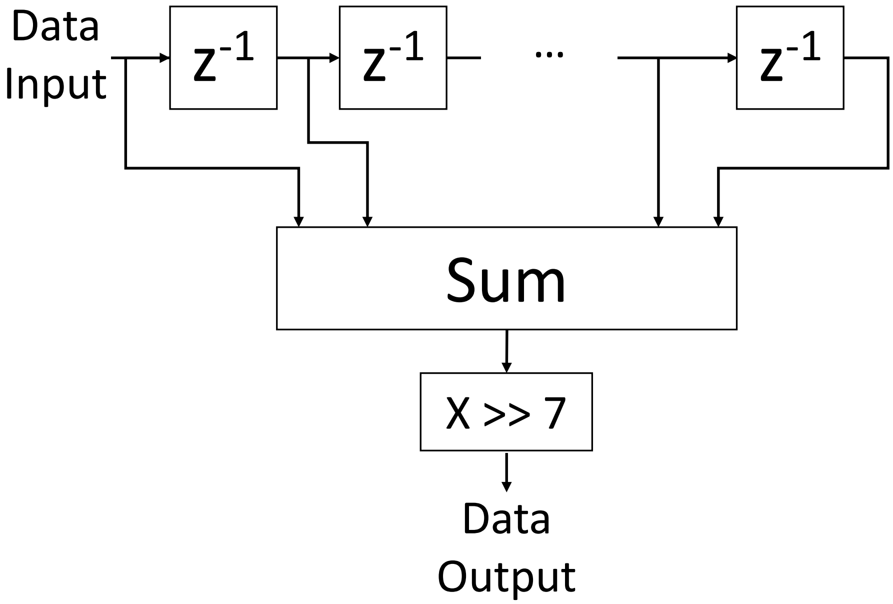

Figure 4.14: First implementation of a moving average of 128-order without usage of DSP slices.

In this implementation 128 delay blocks are used to save the previous values and thus creating a data sliding window. The values stored in the delay elements are then summed and divided by 128. This division can be efficiently implemented with a equivalent 7-bit logical right shift, allowing this design to avoid any DSP slice usage. This moving average implementation was tested in the phase coherence algorithm from Figure 4.12. The timing and resource analysis is detailed in Table 4.3. While this implementation uses no DSP slices it has a serious disadvantage, the sum block has a high fan-in due to the implemented large order of the moving average. This creates a large amount of data signal wiring that will connect the delay outputs to the sum block, thus increasing the holding time for the input gates. This disadvantage makes the implementation unable to met the timing constraints necessary for a real-time implementation.

A second implementation based on the use of a recursive filter to implement the moving average. This implementation also uses no DSP slices and only the last output of a shift register is used. When a new sample enters the moving average, the difference between the last output of the shift register and the current input is calculated. This variation is then added to a register that saves the value of the sum of the last N data values. The output is then divided by N, using for that a $\log_2(N)$ bits left shift. An example for a 128 order moving average is illustrated in Figure 4.15.

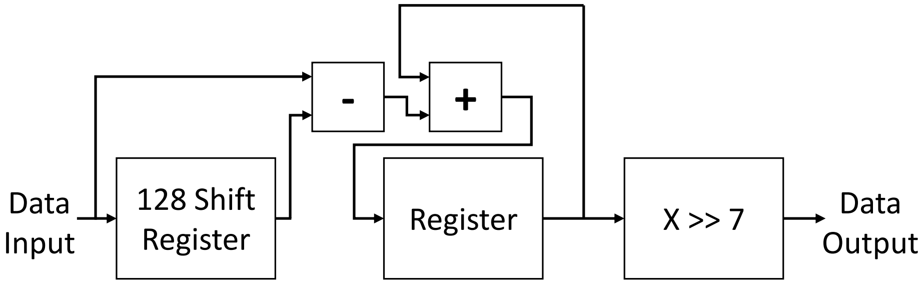

Figure 4.15: Second implementation of a moving average of 128-order without usage of DSP slices.

This accumulator based implementation is able to calculate the moving average while maintaining the timing requirements requested for the design. The only down side of this second implementation is the need to guarantee a zero value initialization sequence in all registers. This is done with a reset before the ADC acquisition. The timing and resource analysis are detailed in Table 4.3.

	LUTs	Registers	DSP	WNS	Max Freq. Operation
Resources in xc7z020	53200	106400	220	4ns	62.5MHz
Parallel sum based algorithm	12482	16565	0	-13.379ns	14.39MHz
Accumulator based algorithm	7455	6853	0	-5.44ns	26.48MHz

Table 4.3: FPGA resources of the purposed phase coherence algorithm by using a shift register.

The values are estimated without any performance or resource optimization from Vivado. Final implementation results can differ in occupation and maximum frequency operation. The selected implementation for the moving average block was then the accumulator based algorithm, as it uses zero DSP slices and also shows the best results for both resources and timing performance.

With the optimal implementation for the moving average block chosen, let us focus in the final hardware implementation of the phase coherence algorithm detailed in the diagram of Figure 4.12. The algorithm was implemented in System Generator 2014.4 [138] and the top level can be seen in Figure 4.16.

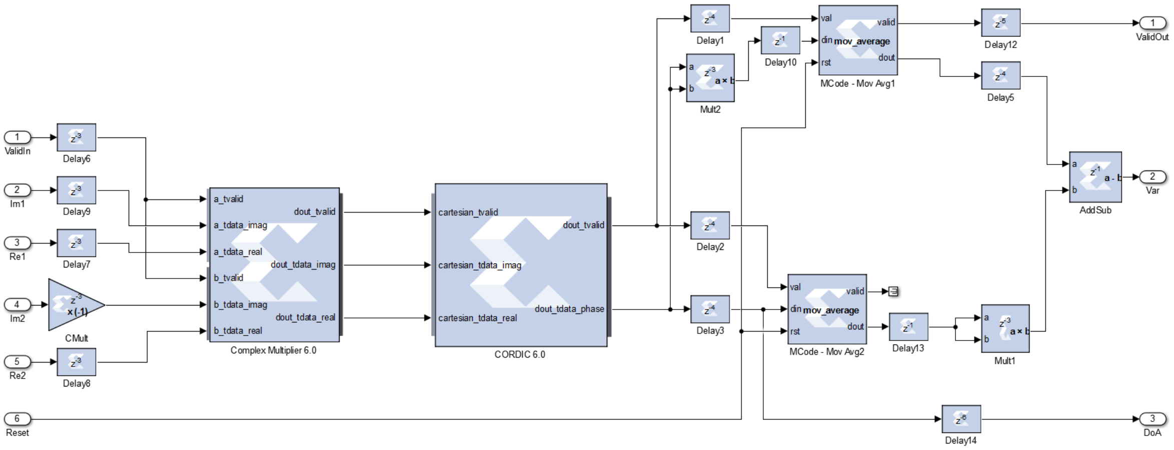

Figure 4.16: Phase coherence algorithm implemented in System Generator.

The algorithm implementation has six inputs, these are: a valid bit that comes from the ADC that signals when the acquired data can be read, two pairs of real and imaginary data signal sampled from both antennas and finally the reset signal. The implemented algorithm block also has three outputs: the propagated valid signal, the variance estimation output and also the DoA estimation. The moving average block is written in MCode [139] and follows the structure from Figure 4.15.

An important detail in the hardware implementation is the use of delay blocks. Every logic operation is synchronous with the same reference clock signal. When a signal is processed by a logic operation it suffers a digital delay. As an example when the second ADC imaginary data (Im2) is multiplied by minus one, it has a delay of three samples (z^{-3}) or three clock periods. In order to all data to be synchronous, every signals should always have the same delay value (i.e. all the inputs of the first Complex Multiplier 6.0 IP-Core need to share the same delay value as Im2). The delay blocks are then used in the hardware design to ensure that all the signals are always synchronous.

4.8.2 Phase coherence with a polyphasic DFT filter bank

Previously the phase coherence algorithm for FPGA implementation was evaluated and developed. This algorithm allows for signal detection, without noise floor estimation, and DoA estimation for a single RF channel. In order to evaluate, multiple channels a solution would be to segment the spectrum using an computational efficient polyphasic DFT filter bank implementation. Each filter bank output frequency channel will then be individually evaluated by a phase coherence block. The FPGA implementation was planned for a 8 contiguous and uniform bands that are obtained using a filter bank of 32th order. These eight channels were chosen as this is the lowest number of outputs possible in the XILINX Fast Fourier Transform 9.0 core. The prototype filter $H(z) = [h(0), h(1), ..., h(31)]$ will be a

32-tap Hann function. As the implementation is polyphasic each band will have 4 coefficients filters.

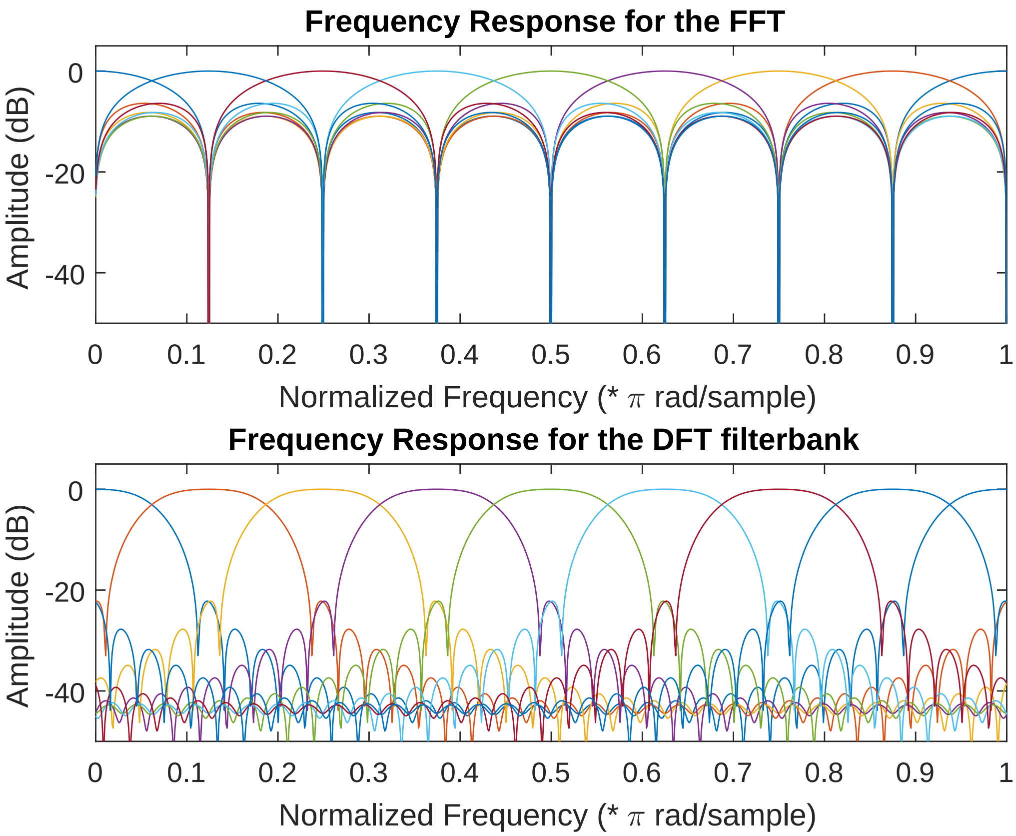

Figure 4.17: On bottom the frequency response of the polyphasic DFT from a 32th order Hann function, on top the frequency response of only the FFT process.

As seen in Figure 4.17 the designed filter bank is based on the Hann function for 8 channels, shows a lower spectral leakage compared to a traditional FFT. This polyphasic DFT filter bank design is then implemented in hardware as seen in Figure 4.18.

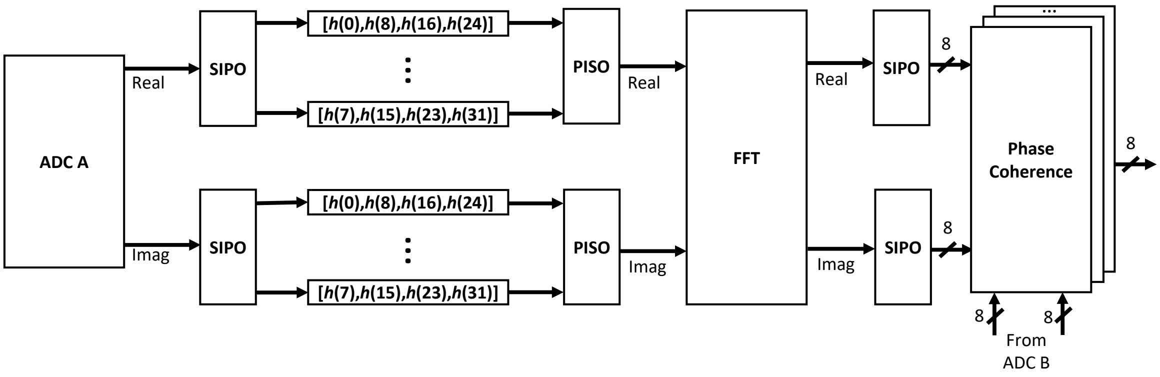

Figure 4.18: FPGA implementation of phase coherence with polyphasic DFT filter bank.

The complex data samples are output in serial from the ADC, due to that, a Serial Input Parallel Output (SIPO) is used to allow polyphasic filtering. The SIPO is implemented with a Time Division Demultiplexer IP Core. Each output is filtered at $\frac{1}{8}$ the ADC sampling frequency, thus allowing a relaxation on the constraint requirements of the filters, compared to a non-polyphasic implementation. Each phase channel is filtered using a FIR Compiler 7.2 block filter implementation that uses 4 coefficients. Both the real and the imaginary component of the data are filtered by the same coefficients, due to this, both components share a single FIR Compiler filter core using two parallel channel paths. After filtering the data goes trough a Parallel Input Serial Output (PISO) block to arrange the data for the FFT block. The core is parameterized to obtain a 8 point DFT of the input data, using for that purpose a 2^3 counter that signals the last data point in each data vector. The FFT complex output is then once again parallelized with a SIPO to be processed by the phase coherence block for signal detection.

This filter bank process is replicated for the data acquired from ADC B as well. The acquired signal from ADC B is also segmented in frequency bands and is then analysed in the phase coherence block. The implementation of the 8 channel phase coherence based on data segmentation with a polyphasic DFT filter bank has the resource usage described in Table 4.4.

	LUTs	Registers	Block RAM	DSP
Resources in xc7z020	53200	106400	140	220
8-channel phase coherence	69063	67747	2	0

Table 4.4: FPGA resources for implementation of 8 channel phase coherence.

The implementation of the phase coherence system, for the minimum number of channels parameterizable in the FFT IP-core, requires more LUT resources than those available in the used FPGA. These values do not include the barebone structure dedicated to communication from the FPGA to the PC and also to control the RF front-end. Thus making it impractical to employ a frequency segmentation architecture based on the analysis of the instantaneous bandwidth of the received ADC data.

4.8.3 Local oscillator sweep testbench design

Due to the impracticability of having multiple phase coherence estimation units for spectrum sensing in the FPGA implementation, a second approach for the frequency analysis was evaluated. This design is based on the same approach taken by spectrum analyzer equipment were the local oscillator sweeps in frequency. Using this type of design on our spectrum sensing unit allows for only one phase coherence block to be used. The RF signal is filtered in frequency channels, in the analog domain at the down conversion block. This local oscillator sweep also allows to increase the analysed frequency span, that was limited by the 56 MHz bandwidth from the used ADCs.

The development board, used in this hardware real-time implementation, is a ZedBoard that features the Xilinx Zynq - XC7Z020 System on Chip (SoC). This SoC has a dual core ARM Cortex-A9 processor and FPGA programmable logic. The ZedBoard is connected to a RF front-end, the AD-FMCOMMS3 that uses as RF transceiver a AD9361 radio frequency integrated circuit [120]. The transceiver has two receiving channels has seen in Figure 4.19.

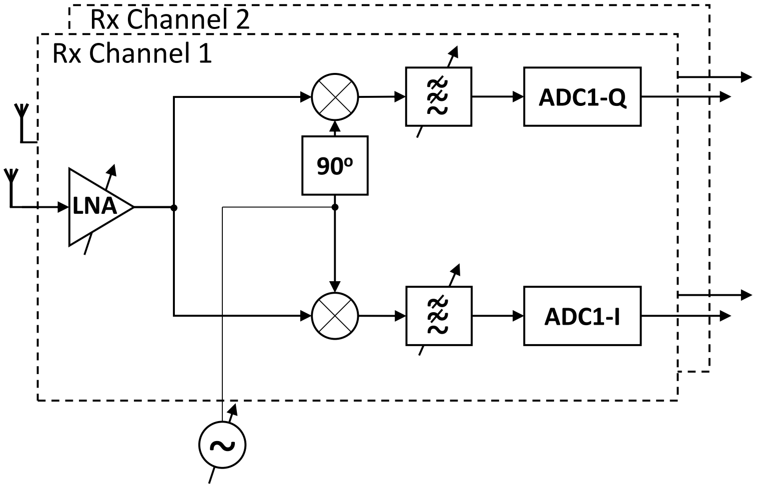

Figure 4.19: Overview of the two receiving channels from AD9361.

Both receiving channels have programmable LNAs for variable gain. The received signal is then downconverted to baseband using two mixers, in order to obtain both I/Q. They also share the same programmable local oscillator, allowing them to sweep synchronously in frequency. The I/Q signal is then filtered in baseband with a programmable low pass filter and is then sampled.

An overview of the developed system, with a design based on the sweep of the local oscillator, is described in Figure 4.20.

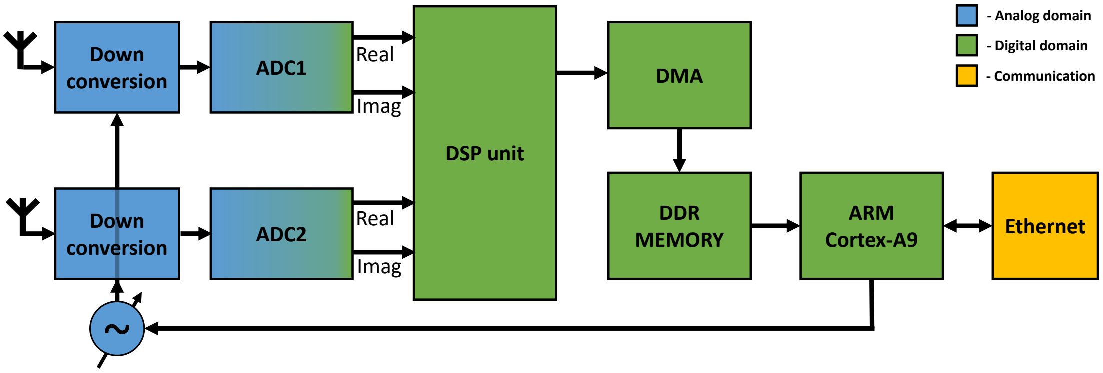

Figure 4.20: Overview of the system used for implementation of the phase coherence detection.

Both antenna elements are connected to the SMA ports of the AD-FMCOMMS3 board and the signal is acquired with the both available analog inputs of the AD9361. The signal is then down-converter to the defined central frequency and sampled in IQ by both ADCs. The data is then sent to the FPGA chip for DSP processing. The processing is done in the DSP unit that will implement the phase coherence method and outputs the data to a Direct Memory Access (DMA) controller that will write in a Double Data Rate (DDR) memory. The memory is then read by the ARM Cortex-A9 processor that will sent the data, using an Ethernet connection, to a personal computer. A protocol was developed for the Ethernet communication that allows the sending of commands to the FPGA and to receive the processed signal detection data. The protocol is built on top of the TCP transport layer of the Internet Protocol (IP). The communication is always initialized by the personal computer, that sends a command to the FPGA board. Every command is defined as a string and has the standard structure seen in Table 4.5.

@	'Number of command'	,	'Payload'	Z

Table 4.5: Implemented protocol command structure.

Each sent command starts with the at sign (@). This char is followed by a string that gives the command number associated with a function that will run on the FPGA. The command number is followed by a comma (,). After the comma there is a payload, that has the command variables. The command string is ended with a Z char. There are a total of five different commands as defined in Table 4.6.

Number	Command
1	Set RX sampling frequency
2	Set RX bandwidth
3	Set RX gain
4	Set frequency sweep step
5	Start a frequency sweep

Table 4.6: Commands implemented for the communication between the PC and the FPGA board.

Command number 1 sets both RX ADCs sampling frequencies to a user defined value, in samples per second, that goes in the payload. This sampling frequency value can go from 200 ksps up to 56 Msps. Command number 2 sets both RX base-band low-pass filters to a specified cut frequency in Hz. In this situation, the filters cut frequency can go from 200 kHz up to 56 MHz. Command 3 sets the gain from both receivers LNA in dB, this value can go from 0 up to 73 dB. Command 4 defines the frequency sweep step value (f_t) in Hz of the local oscillator, this value can be defined from 200 kHz up to 56 MHz. Command 5 defines the initial frequency (f_i) of the sweep and also the end frequency (f_e) in the payload, these values are defined in Hz. These values can be defined from 50 MHz up to 6 GHz.

When the last command is sent by the personal computer for the FPGA to start a frequency sweep, the personal computer will then await for the response of the FPGA board that will sent the results of the implemented DSP algorithm back. When the frequency sweep is started the ARM CPU initializes the DMA operation that will write the ADC data that was processed by the DSP unit, into memory. When the sweep finishes, the processed values are sent from the memory back to the personal computer by Ethernet. The sweep process that runs in the FPGA is described in Figure 4.21.

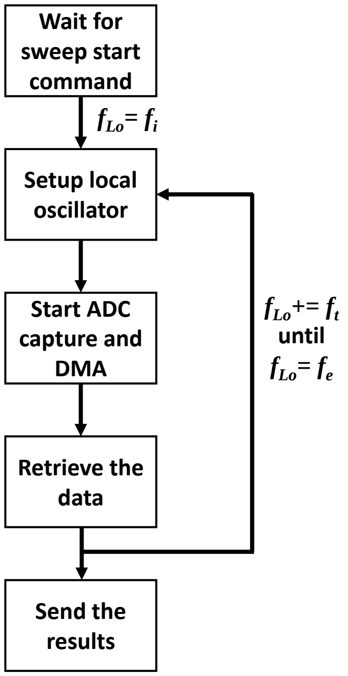

Figure 4.21: State diagram of the spectrum sensing unit frequency sweep process.

After booting, the spectrum sensing unit that runs in the FPGA board initializes the Ethernet connection and waits for the sweep start command. In this state, the system can receive and execute any other command that is sent by the personal computer. When the start sweep command is received, the local oscillator f_{Lo} is defined for the initial frequency f_i. The ADC is then initialized and the acquisition starts, the DMA controller writes the processed data directly into memory. In order to avoid the initial transient response of the filters, that are part of the signal detection algorithm, the transient part of the data is ignored and not saved. The local oscillator f_{Lo} is then updated with a increment of f_t and the ADC sampling is repeated. This iteration ends when the f_{Lo} reaches the defined last frequency of the sweep f_e. The detection result data for each frequency of the sweep is then sent at the same time to the personal computer.

Each IP packet is able to send 1500bytes of payload, it means that for larger sweeps it may be necessary to use more than one packet. Due to that, the protocol allows to send the data sliced in more than one packet. Also a common problem of TCP transmission is that the transmitted packets can be received out of order. In the built protocol this problem was solved by sending in each frame, coming from the FPGA, the packet number. The FPGA sends the result data in a command response that is defined as a string and has a standard structure as seen in Table 4.7.

@	'Number of the packet'	,	'Payload'	Z

Table 4.7: Implemented protocol structure of the command response.

Each command response starts with the at sign (@). This char is followed by a string describing the packet number. The packet number is followed by a comma. After the comma there is the payload, that has the DSP processed values, and the command response ends with a Z char.

The full FPGA design has then the communication between the FPGA and the RF front-end, the Ethernet communication with the personal computer and also the phase coherence DSP algorithm. In Table 4.8 the FPGA resources and timing constraints, as Worst Negative Slack (WNS), of the barebone communications without the DSP algorithm and also the full implementation are described.

	LUTs	Registers	Block RAM	DSP	WNS	Max Freq. Operation
Resources in xc7z020	53200	106400	140	220	4ns	62.5MHz
Barebone communications	14057	22403	8	69	+0.202ns	62.5MHz
Full implementation	19904	26245	8	69	-1.807ns	43.05MHz

Table 4.8: FPGA resources and timing for the full implementation.

4.8.4 Experimental validation with two transmitters

In order to evaluate the feasibility of the proposed system testbed to sense simultaneous transmissions, a scenario with two RF transmissions was analysed. The receiver ports used in the following experiments are the A:RX2 and B:RX2. These are separated by a distance of 2.5 cm. Both ports are connected to two omni-directional VERT2450 antennas. The RF front-end will sweep between 70 MHz and 6 GHz in steps of 1 MHz using a bandwidth of 1 MHz. Each ADC will be sampling I/Q at 1 Msps. The transmissions were generated by a single SMW200A VSG connected to two patch array antennas with 16 elements as can be seen in Figure 4.22.

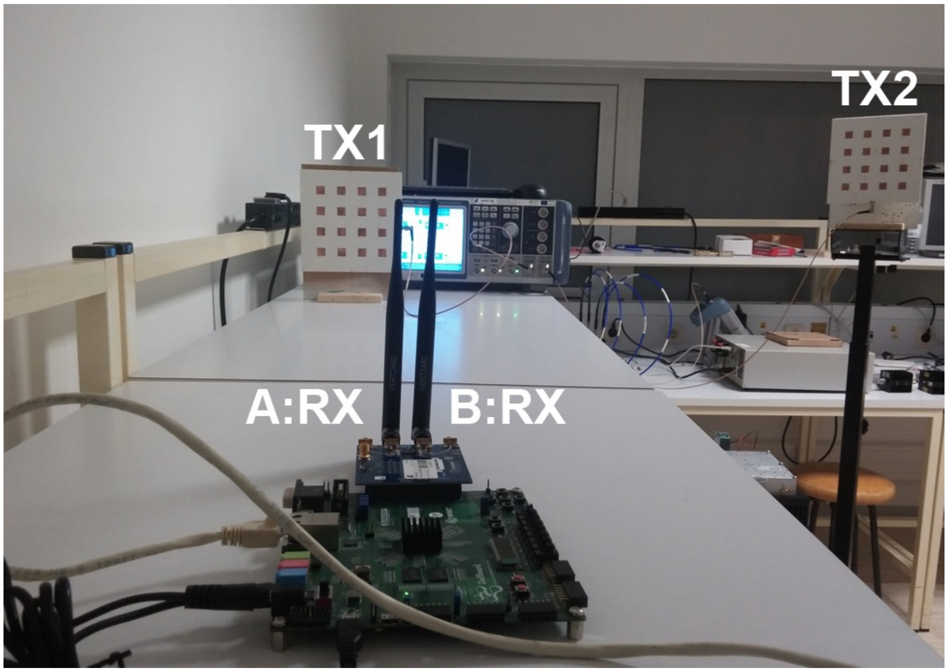

Figure 4.22: Experimental setup for validation of the FPGA implementation.

Each generator transmits an, independently generated, random sequence signal modulated in BPSK that is filtered with a raised-cosine with a roll-off factor of 0.1. The Tx_1 transmission is coming from the left with an angle of 20^o, with a 40 MHz bandwidth, centered at $f_c = 5\,\text{GHz}$ and transmitting at -20 dBm. The Tx_2 transmission is coming from the right with an angle of 50^o, with $20\,\text{MHz}$ bandwidth, centered at $f_c = 5.2\,\text{GHz}$ and also transmitting at -20 dBm. The phase coherency results calculated by the system are plotted in Figure 4.23.

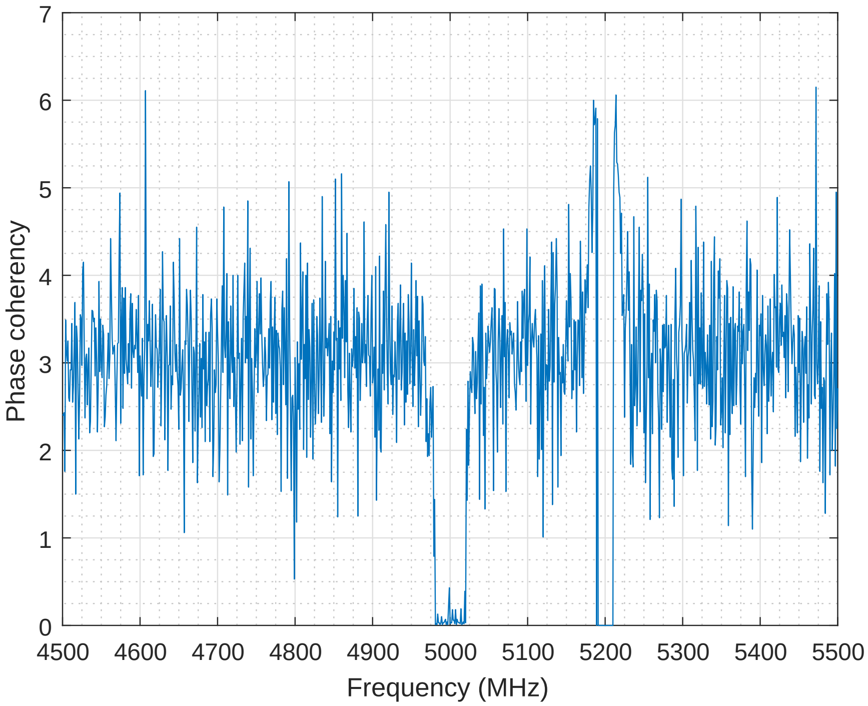

Figure 4.23: FPGA calculated phase coherency data for the frequency sweep.

From the obtained results the implemented phase coherency is then able to detect both transmissions and also determining the bandwidth of each received signal. The DoA can also be obtained from the phase relationship of both antennas adquired signal. The FPGA calculated DoA is plotted in Figure 4.23.

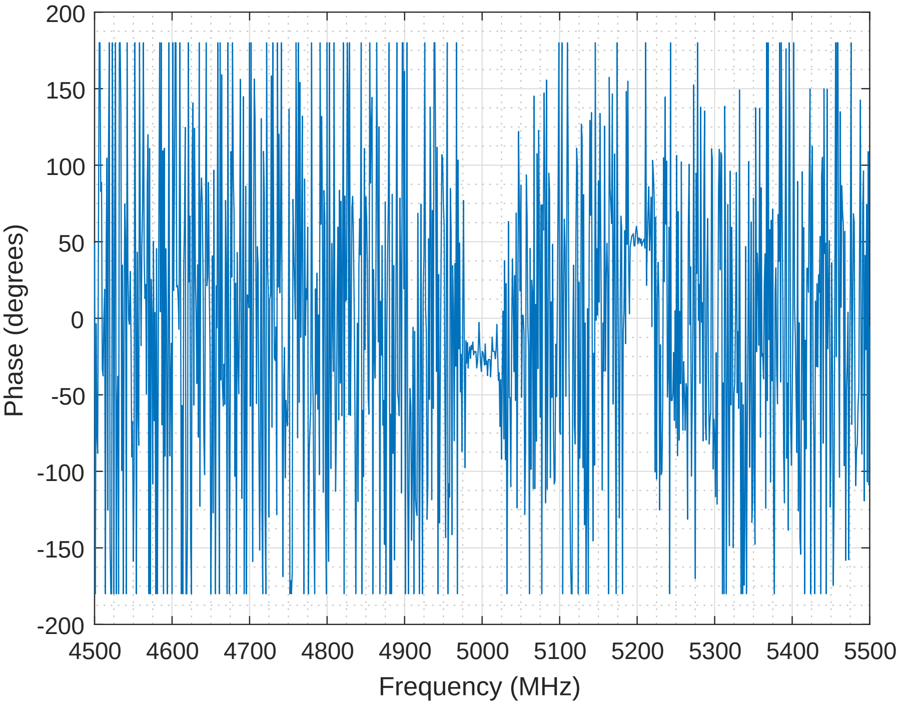

Figure 4.24: FPGA calculated DoA data for the frequency sweep.

It is visible that in the frequency bands of interest where the two signals are being transmitted and signal is present, the phase relationship gives an estimation of the DoA and outside those frequency bands the phase relationship has, as expected, a random uniform distribution.

4.8.5 Discussion of FPGA implementation of the phase coherence method

The phase coherence method was successfully developed on FPGA, using a design that allows a low resource usage of the available hardware while maintaining a good timing performance. For multiple frequency band analysis, a solution based on polyphasic DFT filter bank was evaluated but the resource analysis showed that it would need more resources than those available in the available FPGA. A testbench based on a Zedboard and AD-FMCOMMS3 development boards was created for a real-time implementation of the phase coherence algorithm. A communication protocol using Ethernet and based on TCP communication was implemented allowing for configuration of the system and data transfer. The implemented hardware was evaluated in laboratory and the results obtained in offline processing were also achieve in the FPGA implementation. The system was able to determine both the spectrum occupation based on the phase coherence method as well as the DoA of two simulations transmissions.

Chapter 5

Conclusions

In this thesis various combinations of spectrum sensing elements were explored. In the field of spectrum analysis, methods as the periodogram, eigenvalue, cyclostationarity, polyphasic filter bank and multitaper were studied. In the field of cyclostationarity analysis it is relevant to emphasize the contribution on taking advantage of the leakage from the cyclic spectrum analysis to improve detection, published in EuMW. Implementation of spectrum sensing for bio-radar devices was purposed and published in the Journal of Medical Systems. Signal detection theory was explained, and a system capable of detecting signal for non-continuous LTE-Uplink transmissions was purposed and published in CONFTELE. Noise estimation techniques were also explored and a contribution for estimating the noise floor using a energy estimator and the EM algorithm with a GMM was purposed. This method was published in URSI-Portugal conference and won the best student paper award. The EM was also further explored to determine the number of users and their occupation in time. This contribution was published in the Physical Communication Journal. Other less computational complex methods were also explored to determine the number of users occupying using the medium, as the subtractive histogram method, published in IWINAC. A signal detection method using two receiver antennas was also proposed. This method takes advantage of the phase relationship between both antennas elements, eliminating the need for noise floor estimation, allowing to remove from detection the LO leakage and detect constantly transmitting signals. The usage of two antennas also allows for a estimation of DoA. After validation with experimental results, this method was also successfully implemented in a FPGA for a wideband real-time spectrum sensing. Future research work should focus in improving the phase coherence algorithm and implementing it in multiple channels based on the filterbank approach but for a higher capacity and performance FPGA chip.

Bibliography

[1] M. H. Islam, L. K. Choo, W. O. Ser, Q. Xianming, Y. L. Yoke, W. Cavin, Y. C. Liang, E. T. Bee, C. Francois, L. T. Geok, and T. William "Spectrum survey in Singapore: Occupancy measurements and analyses" *Proceedings of the 3rd International Conference on Cognitive Radio Oriented Wireless Networks and Communications, CrownCom* pp. 1–7 2008.

[2] R. Urban, T. Korinek, and P. Pechac "Broadband spectrum survey measurements for cognitive radio applications" *Radioengineering* vol. 21 no. 4 pp. 1101–1109 2012.

[3] M. Hamid, N. Björsell, W. Van Moer, K. Barbé, and B. S. Slimane "Blind Spectrum Sensing for Cognitive Radios Using Discriminant Analysis: A Novel Approach" *IEEE Transactions on Instrumentation and Measurement* vol. 62 no. 11 pp. 2912–2921 2013.

[4] A. Wyglinski, M. Nekovee, and T. Hou *Cognitive radio communications and networks: principles and practice.* Academic Press, 2009.

[5] J. Mitola "Software radios: Survey, critical evaluation and future directions" *IEEE Aerospace and Electronic Systems Magazine* vol. 8 no. 4 pp. 25–36 apr 1993.

[6] S. Galih, M. Hoffmann, and T. Kaiser "Low Cost Implementation for Synchronization in Distributed Multi Antenna Using USRP/GNU-Radio" *Proceedings of the 1st International Conference on Information Technology, Computer, and Electrical Engineering* pp. 457–460 2014.

[7] M. B. Sruthi, M. Abirami, A. Manikkoth, R. Gandhiraj, and K. P. Soman "Low cost digital transceiver design for Software Defined Radio using RTL-SDR" *2013 International Multi-Conference on Automation, Computing, Communication, Control and Compressed Sensing, 2013 iMac4s* pp. 852–855 2013.

[8] Y.-k. Kwag, J.-s. Jung, I.-s. Woo, and M.-s. Park "Multi-Band Multi-Mode SDR Radar Platform" *Synthetic Aperture Radar (APSAR)* pp. 46–49 2015.

[9] K. Lin, W. Wang, X. Wang, W. Ji, and J. Wan "QoE-driven spectrum assignment for 5G wireless networks using SDR" *IEEE Wireless Communications* vol. 22 no. 6 pp. 48–55 2015.

[10] J. Mitola and G. Q. Maguire "Cognitive radio: making software radios more personal" *IEEE Personal Communications* vol. 6 no. August pp. 13–18 1999.

[11] “Collaborative Spectrum Sharing | Horizon Prizes - Research Innovation - European Commission.” [Online]. Available: http://ec.europa.eu/research/horizonprize/index.cfm?prize=spectrum-sharing

[12] “DARPA’s Spectrum Collaboration Challenge.” [Online]. Available: http://spectrumcollaborationchallenge.com/

[13] Q. Zhao and B. M. Sadler “A Survey of Dynamic Spectrum Access” *Signal Processing Magazine, IEEE* vol. 24 no. May pp. 79–89 2007.

[14] T. Irnich, J. Kronander, Y. Selen, and G. Li “Spectrum sharing scenarios and resulting technical requirements for 5G systems” *IEEE International Symposium on Personal, Indoor and Mobile Radio Communications, PIMRC* pp. 127–132 2013.

[15] J. Khun-Jush, P. Bender, B. Deschamps, and M. Gundlach “Licensed shared access as complementary approach to meet spectrum demands: Benefits for next generation cellular systems” *ETSI workshop on reconfigurable radio systems* no. December pp. 1–7 2012.

[16] A. Kliks, O. Holland, A. Basaure, and M. Matinmikko “Spectrum and License Flexibility for 5G Networks” *IEEE Communications Magazine* no. July pp. 42–49 2015.

[17] H. Wang, G. Noh, D. Kim, S. Kim, and D. Hong “Advanced sensing techniques of energy detection in cognitive radios” *Journal of Communications and Networks* vol. 12 no. 1 pp. 19–29 feb 2010. [Online]. Available: http://ieeexplore.ieee.org/lpdocs/epic03/wrapper.htm?arnumber=6388431

[18] D. Niyato, E. Hossain, and Z. Han “Dynamic spectrum access in IEEE 802.22-based cognitive wireless networks: a game theoretic model for competitive spectrum bidding and pricing” *Wireless Communications, IEEE* vol. 16 no. April pp. 16–23 2009. [Online]. Available: http://ieeexplore.ieee.org/xpls/abs_all.jsp?arnumber=4907555

[19] A. B. Flores, R. E. Guerra, E. W. Knightly, P. Ecclesine, and S. Pandey “IEEE 802.11af: A standard for TV white space spectrum sharing” *IEEE Communications Magazine* vol. 51 no. October pp. 92–100 2013.

[20] C. Stevenson, G. Chouinard, S. Shellhammer, and W. Caldwell “IEEE 802.22: The first cognitive radio wireless regional area network standard” *IEEE Communications Magazine* vol. 47 no. 1 pp. 130–138 jan 2009. [Online]. Available: http://ieeexplore.ieee.org/lpdocs/epic03/wrapper.htm?arnumber=4752688

[21] ITU-R “Radio Regulations, Edition of 2012.” [Online]. Available: http://www.itu.int/dms_pub/itu-s/oth/02/02/S02020000244501PDFE.pdf

[22] J. G. Andrews, S. Buzzi, W. Choi, S. V. Hanly, A. Lozano, A. C. K. Soong, and J. C. Zhang “What will 5G be?” *IEEE Journal on Selected Areas in Communications* vol. 32 no. 6 pp. 1065–1082 2014.

[23] Cisco “Cisco Visual Networking Index : Forecast and Methodology , 2014-2019” Tech. Rep. 2015. [Online]. Available: http://www.cisco.com/c/en/us/solutions/collateral/service-provider/ip-ngn-ip-next-generation-network/white_paper_c11-481360.htmll

[24] S. Talwar, D. Choudhury, K. Dimou, E. Aryafar, B. Bangerter, and K. Stewart "Enabling technologies and architectures for 5G wireless" *IEEE MTT-S International Microwave Symposium Digest* 2014.

[25] COMMISSION OF THE EUROPEAN COMMUNITIES "Decision 2005/513/EC" vol. 5 pp. 22–24 2005.

[26] V. Syrjälä and M. Valkama "Coexistence of LTE and WLAN in Unlicensed Bands : Full-Duplex Spectrum Sensing" in *Cognitive Radio Oriented Wireless Networks: 10th International Conference* 2015.

[27] Qualcomm Incorporated "LTE in Unlicensed Spectrum : Harmonious Coexistence with Wi-Fi" *White Paper* no. June pp. 1–19 2014.

[28] N. The "Toward Spectrum Sharing : Opportunities and Technical Enablers" no. July pp. 26–33 2015.

[29] I. Mitola, J., J. Guerci, J. Reed, Y.-D. Yao, Y. Chen, T. Clancy, J. Dwyer, H. Li, H. Man, R. McGwier, and Y. Guo "Accelerating 5G QoE via public-private spectrum sharing" *IEEE Communications Magazine* vol. 52 no. May pp. 77–85 2014.

[30] Y. Liu, Y. Zhang, R. Yu, and S. Xie "Integrated energy and spectrum harvesting for 5G wireless communications" *IEEE Network* vol. 29 no. 3 pp. 75–81 2015. [Online]. Available: http://ieeexplore.ieee.org/lpdocs/epic03/wrapper.htm?arnumber=7113229

[31] O. Yilmaz, Z. Li, K. Valkealahti, and M. Uusitalo "Smart Mobility Management for D2D Communications in 5G Networks" *Metis2020.Com* pp. 219–223 2014. [Online]. Available: https://www.metis2020.com/wp-content/uploads/publications/IEEE_WCNC_2014_Yilmaz_etal_D2D_Mobility_in_5G_Networks.pdf

[32] S. Mumtaz, K. M. Saidul Huq, and J. Rodriguez "Direct mobile-to-mobile communication: Paradigm for 5G" *IEEE Wireless Communications* vol. 21 no. 5 pp. 14–23 2014.

[33] A. Droitcour "Signal-to-noise ratio in Doppler radar system for heart and respiratory rate measurements" *Microwave Theory and Techniques, IEEE Transactions* 2009. [Online]. Available: http://ieeexplore.ieee.org/xpls/abs_all.jsp?arnumber=5238512

[34] W. Hu, Z. Zhao, and Y. Wang "Noncontact Accurate Measurement of Cardiopulmonary Activity Using a Compact Quadrature Doppler Radar Sensor" *Biomedical Engineering , IEEE Transactions on* 2014. [Online]. Available: http://ieeexplore.ieee.org/xpls/abs_all.jsp?arnumber=6654242

[35] D. Malafaia, J. Vieira, and A. Tomé "Improving Performance of Bio-radars for Remote Heartbeat and Breathing Detection by using Cyclostationary Features" in *Proceedings of the International Conference on Bio-inspired Systems and Signal Processing* 2015 pp. 344–349. [Online]. Available: http://www.scitepress.org/DigitalLibrary/Link.aspx?doi=10.5220/0005287603440349

[36] D. Malafaia, B. Oliveira, P. Ferreira, T. Varum, J. Vieira, and A. Tomé "Cognitive bio-radar: The natural evolution of bio-signals measurement" *Journal*

of Medical Systems vol. 40 no. 10 p. 219 2016. [Online]. Available: http://link.springer.com/10.1007/s10916-016-0572-8

[37] E. Axell and G. Leus “Spectrum sensing for cognitive radio: State-of-the-art and recent advances” *Signal Processing …* no. MAY 2012 pp. 101–116 2012. [Online]. Available: http://ieeexplore.ieee.org/xpls/abs_all.jsp?arnumber=4840525http://ieeexplore.ieee.org/xpls/abs_all.jsp?arnumber=6179814

[38] H. Afzal, M. R. Mufti, M. Nadeem, I. Awan, and U. S. Khan “The Role of Spectrum Manager in IEEE 802 . 22 Standard” *Journal of Basic and Applied Scientific Research* vol. 4 no. 4 pp. 280–289 2014.

[39] G. Yu, C. Long, M. Xiang, and W. Xi “A Novel Energy Detection Scheme Based on Dynamic Threshold in Cognitive Radio Systems” *Journal of Computational Information Systems* vol. 8 no. 6 pp. 2245–2252 2012. [Online]. Available: www.jofcis.com/publishedpapers/2012_8_6_2245_2252.pdf

[40] M. S. Gast *802.11n: A Survival Guide.* "O’Reilly Media, Inc.", 2012. [Online]. Available: https://books.google.com/books?id=RJVMb4ZOMb8C&pgis=1

[41] L. Lu, H. Wu, and S. Iyengar “A novel robust detection algorithm for spectrum sensing” *Selected Areas in Communications, …* vol. 29 no. 2 pp. 1–11 2011. [Online]. Available: http://ieeexplore.ieee.org/xpls/abs_all.jsp?arnumber=5701685

[42] Y. Zeng and Y.-c. Liang “Eigenvalue-based spectrum sensing algorithms for cognitive radio” *IEEE Transactions on Communications* vol. 57 no. 6 pp. 1784–1793 jun 2009. [Online]. Available: http://ieeexplore.ieee.org/lpdocs/epic03/wrapper.htm?arnumber=5089517

[43] S. Maleki, A. Pandharipande, and G. Leus “Two-stage spectrum sensing for cognitive radios” *2010 IEEE International Conference on Acoustics, Speech and Signal Processing* pp. 2946–2949 2010. [Online]. Available: http://ieeexplore.ieee.org/lpdocs/epic03/wrapper.htm?arnumber=5496149

[44] T. Yucek and H. Arslam “A Survey of Spectrum Sensing Algorithms for Congnitive Radio Applications” *IEEE Communications Surveys Tutorials* vol. 97 no. 1 pp. 805–823 2009.

[45] A. M. Tomé, D. Malafaia, J. Vieira, A. R. Teixeira, and E. Lang “Singular Spectrum Analysis for Narrowband Signal Enhancement and Detection” *Digital Signal Processing* pp. 1–18 2016.

[46] J. Antoni “Cyclic spectral analysis in practice” *Mechanical Systems and Signal Processing* vol. 21 no. 2 pp. 597–630 feb 2007. [Online]. Available: http://linkinghub.elsevier.com/retrieve/pii/S0888327006001816

[47] S. Li and Y. Wang “Method of modulation recognition of typical communication satellite signals based on cyclostationary” *2013 ICME International Conference on Complex Medical Engineering* no. 4 pp. 268–273 may 2013. [Online]. Available: http://ieeexplore.ieee.org/lpdocs/epic03/wrapper.htm?arnumber=6548253

[48] S. Dikmese, S. Srinivasan, and M. Renfors "FFT and filter bank based spectrum sensing and spectrum utilization for cogntive radios" *5th International Symposium on Communications Control and Signal Processing, ISCCSP 2012* no. May pp. 2–4 2012.

[49] T. Mehta, N. Kumar, and S. S. Saini "Comparison of Spectrum Sensing Techniques in Cognitive Radio Networks" *InternatIonal Journal of electronIcs communIcatIon technology* vol. 7109 2013.

[50] D. Ariananda, M. Lakshmanan, and H. Nikoo "A survey on spectrum sensing techniques for Cognitive Radio" *2009 Second International Workshop on Cognitive Radio and Advanced Spectrum Management* pp. 74–79 2009.

[51] A. Schuster "On the investigation of hidden periodicities with application to a supposed 26 day period of meteorological phenomena" *Journal of Geophysical Research* vol. 3 no. 1 p. 13 1898. [Online]. Available: http://doi.wiley.com/10.1029/TM003i001p00013

[52] G. a. Prieto, R. L. Parker, D. J. Thomson, F. L. Vernon, and R. L. Graham "Reducing the bias of multitaper spectrum estimates" *Geophysical Journal International* vol. 171 no. 3 pp. 1269–1281 oct 2007. [Online]. Available: http://gji.oxfordjournals.org/cgi/doi/10.1111/j.1365-246X.2007.03592.x

[53] M. J. Alam, P. Kenny, and D. O'Shaughnessy "A Study of Low-variance Multi-taper Features for Distributed Speech Recognition" in *Advances in Nonlinear Speech Processing.* Springer Berlin Heidelberg, 2011 pp. 239–245.

[54] M. Hamid, K. Barbé, N. Björsell, and W. Van Moer "Spectrum sensing through spectrum discriminator and maximum minimum eigenvalue detector: A comparative study" *IEEE I2MTC - International Instrumentation and Measurement Technology Conference, Proceedings* pp. 2252–2256 2012.

[55] N. Golyandina, V. Nekrutkin, and A. A. Zhigljavsky *Analysis of Time Series Structure : SSA and Related Techniques.* CRC Press, 2001.

[56] W. Pan, H. Wang, and L. Shen "Covariance matrix based spectrum sensing for OFDM based cognitive radio" *2012 International Conference on Systems and Informatics (ICSAI2012)* no. Icsai pp. 1426–1430 2012. [Online]. Available: http://ieeexplore.ieee.org/lpdocs/epic03/wrapper.htm?arnumber=6223304

[57] M. Vlachos, P. S. Yu, and V. Castelli "On periodicity detection and structural periodic similarity" *Proc. of the 5th SIAM Int. Conf. on Data Mining* vol. 119 pp. 449–460 2005.

[58] G. Giannakis, E. V. K. Madisetti, and D. B. Williams "Cyclostationary Signal Analysis" in *Statistical Signal Processing Section of Digital Signal Processing Handbook.* CRC Press, 1999 ch. 17.

[59] W. a. Gardner, A. Napolitano, and L. Paura "Cyclostationarity: Half a century of research" *Signal Processing* vol. 86 no. 4 pp. 639–697 apr 2006.

[60] R. Prasad *OFDM for Wireless Communications Systems.* Artech House, 2004.

[61] N. Han, G. Zheng, S. Sohn, and J. Kim “Cyclic Autocorrelation Based Blind OFDM Detection and Identification for Cognitive Radio” *International Conference on Wireless Communications, Networking and Mobile Computing* vol. 0 pp. 1–5 oct 2008. [Online]. Available: http://ieeexplore.ieee.org/lpdocs/epic03/wrapper.htm?arnumber=4678222

[62] M. Castro “Cyclostationary detection for ofdm in cognitive radio systems” 2011. [Online]. Available: http://digitalcommons.unl.edu/elecengtheses/21/

[63] Y. Ou and Y. Wang “Efficient methods for spectrum sensing in cognitive radio” *Wireless Communications and Signal Processing* no. 60872003 2010. [Online]. Available: http://ieeexplore.ieee.org/xpls/abs_all.jsp?arnumber=5630652

[64] W. Yue and B. Zheng “Spectrum sensing algorithms for primary detection based on reliability in cognitive radio systems” *Computers Electrical Engineering* vol. 36 no. 3 pp. 469–479 may 2010. [Online]. Available: http://linkinghub.elsevier.com/retrieve/pii/S0045790609001074

[65] J. Proakis “Digital Signal Processing: Principles, Algorithms, and Applications, 4/e” 2007. [Online]. Available: http://www.ece.uvic.ca/$\sim$mmcguire/teaching/e310/ELEC_310_S_2007.pdfhttp://scholar.google.com/scholar?hl=en&btnG=Search&q=intitle:Digital+signal+processing+principles,+algorithms+and+applications#0

[66] D. Thomson “Spectrum estimation and harmonic analysis” *Proceedings of the IEEE* vol. 70 1982. [Online]. Available: http://ieeexplore.ieee.org/xpls/abs_all.jsp?arnumber=1456701

[67] K. Riedel and a. Sidorenko “Minimum bias multiple taper spectral estimation” *IEEE Transactions on Signal Processing* vol. 43 no. 1 pp. 188–195 1995. [Online]. Available: http://ieeexplore.ieee.org/lpdocs/epic03/wrapper.htm?arnumber=365298

[68] D. Slepian and H. Pollak “Prolate spheroidal wave functions, Fourier analysis and uncertainty” *Bell System Technical Journal* 1961. [Online]. Available: http://onlinelibrary.wiley.com/doi/10.1002/j.1538-7305.1961.tb03976.x/abstract

[69] P. Mitra “Neural Signal Processing: Quantitative Analysis of Neural Activity” *Washington, DC: Society for Neuroscience.* vol. Mitra P, e pp. 1–98 2008. [Online]. Available: http://physics.ucsd.edu/neurophysics/publications/SfN_Short_Course_3.pdf

[70] O. A. Alghamdi, M. A. Abu-rgheff, and M. Z. Ahmed “MTM Parameters Optimization for 64-FFT Cognitive Radio Spectrum Sensing using Monte Carlo Simulation” *Second International Conference on Emerging Network Intelligence* no. c pp. 107–113 2010.

[71] P. S. Reddy and P. Palanisamy “Multitaper Spectrum Sensing Using Sinusoidal Tapers” *2013 2nd International Conference on Advanced Computing, Networking and Security* pp. 47–50 dec 2013. [Online]. Available: http://ieeexplore.ieee.org/lpdocs/epic03/wrapper.htm?arnumber=6714136

[72] D. B. Percival “Spectral Analysis of Time Series - Chapter 7” 1992. [Online]. Available: http://faculty.washington.edu/dbp/s520/PDFs/7-for-printing.pdf

[73] G. A. Prieto, R. L. Parker, D. J. Thomson, F. L. Vernon, and R. L. Graham “Reducing the bias of multitaper spectrum estimates” *Geophysical Journal International* vol. 171 no. 3 pp. 1269–1281 2007. [Online]. Available: http://onlinelibrary.wiley.com/doi/10.1111/j.1365-246X.2007.03592.x/full

[74] J. Pitton “Time-frequency spectrum estimation: an adaptive multitaper method” in *Proceedings of the IEEE-SP International Symposium on Time-Frequency and Time-Scale Analysis (Cat. No.98TH8380).* IEEE, 1998 pp. 665–668. [Online]. Available: http://ieeexplore.ieee.org/document/721512/

[75] S. M. Kay *Fundamentals of statistical signal processing - Detection Theory.* Prentice Hall, 1998.

[76] A. De Maio, A. Farina, and G. Foglia “Design and experimental validation of Knowledge-based CFAR detectors” *IEEE National Radar Conference - Proceedings* no. January pp. 128–135 2006.

[77] V. Amanipour and A. Olfat “CFAR detection for multistatic radar” *Signal Processing* vol. 91 no. 1 pp. 28–37 jan 2011. [Online]. Available: http://linkinghub.elsevier.com/retrieve/pii/S0165168410002392

[78] J. J. LEHTOMÄKI, R. VUOHTONIEMI, K. UMEBAYASHI, and J.-P. MÄKELÄ “Energy Detection Based Estimation of Channel Occupancy Rate with Adaptive Noise Estimation” *IEICE Trans. Commun.* vol. E95-B no. 4 pp. 1076–1084 2012. [Online]. Available: http://joi.jlc.jst.go.jp/JST.JSTAGE/transcom/E95.B.1076?from=CrossRef

[79] R. Tandra and A. Sahai “SNR Walls for Signal Detection” *IEEE Journal of Selected Topics in Signal Processing* vol. 2 no. 1 pp. 4–17 feb 2008. [Online]. Available: http://ieeexplore.ieee.org/lpdocs/epic03/wrapper.htm?arnumber=4453895

[80] S. H. Hwang and M. J. Rim “Adaptive operation scheme for quiet period in IEEE 802.22 system” *2011 International Conference on ICT Convergence, ICTC 2011* pp. 482–484 2011.

[81] N. Mukhopadhyay “Probability and Statistical Inference” p. 665 2000.

[82] A. Mariani, A. Giorgetti, and M. Chiani “SNR Wall for Energy Detection with Noise Power Estimation” *2011 IEEE International Conference on Communications (ICC 2011)* pp. 1–6 2011. [Online]. Available: http://ieeexplore.ieee.org/lpdocs/epic03/wrapper.htm?arnumber=5963367

[83] T. Specification “TS 136 211 - V12.3.0 - LTE; Evolved Universal Terrestrial Radio Access (E-UTRA); Physical channels and modulation (3GPP TS 36.211 version 12.3.0 Release 12)” vol. 0 2014.

[84] A. Duda “Understanding the Performance of 802.11 Networks” *2008 IEEE 19th International Symposium on Personal, Indoor and Mobile Radio Communications* no. 1 pp. 1–6 2008. [Online]. Available: http://clarinet.u-strasbg.fr/$\sim$pansiot/enseignement/MasterRecherche/PIMRC08-80211-DudaA.pdfhttp://ieeexplore.ieee.org/lpdocs/epic03/wrapper.htm?arnumber=4699942

[85] A. Papoulis and S. Pillai *Probability, random variables, and stochastic processes.* McGraw-Hill, 2002.

[86] D. Malafaia, J. Vieira, and A. Tmé “Adaptive threshold Spectrum Sensing based on EM algorithm” *Physical Communication* 2016.

[87] T. K. Moon “The expectation-maximization algorithm” *IEEE Signal Processing Magazine* vol. 13 pp. 47–60 1996.

[88] M. a. T. Figueiredo and R. D. Nowak “An EM algorithm for wavelet-based image restoration.” *IEEE transactions on image processing : a publication of the IEEE Signal Processing Society* vol. 12 no. 8 pp. 906–916 2003.

[89] Y. Zhang, M. Brady, and S. Smith “Segmentation of Brain MR Images Through a Hidden Markov Random Field Model and the Expectation-Maximization Algorithm” vol. 20 no. 1 pp. 45–57 2001.

[90] M. Zheleva, R. Chandra, A. Chowdhery, A. Kapoor, and P. Garnett “TxMiner : Identifying transmitters in real-world spectrum measurements” *Dynamic Spectrum Access Networks (DySPAN)* no. i pp. 99–110 2015.

[91] A. Assra, J. Yang, and B. Champagne “An EM Approach for Cooperative Spectrum Sensing in Multi-Antenna CR Networks” *IEEE Transactions on Vehicular Technology* vol. 9545 no. c pp. 1–1 2015.

[92] C. Bishop and N. Nasrabadi “Pattern recognition and machine learning” *Pattern Recognition* vol. 4 no. 4 p. 738 2006. [Online]. Available: http://www.library.wisc.edu/selectedtocs/bg0137.pdf

[93] A. Etemadi, P. Azmi, and S. Kashef “Robust Spectrum Sensing Method Based on Ranks over Non-Gaussian Channels” no. Icee pp. 1432–1437 2014.

[94] B. Sadler and R. Kozick “Maximum-likelihood array processing in non-Gaussian noise with Gaussian mixtures” *IEEE Transactions on Signal Processing* vol. 48 no. 12 pp. 3520–3535 2000. [Online]. Available: http://ieeexplore.ieee.org/lpdocs/epic03/wrapper.htm?arnumber=887045

[95] A. A. Hammadi, O. Alhussein, S. Muhaidat, M. Al-Qutayri, S. Al-Araji, and G. K. Karagiannidis “Unified Analysis of Cooperative Spectrum Sensing over Composite and Generalized Fading Channels” *IEEE Trans. Vehicul. Technol.* vol. 9545 no. c pp. 1–12 2015. [Online]. Available: http://arxiv.org/abs/1503.01415

[96] J. W. Lindeberg “Eine neue Herleitung des Exponentialgesetzes in der Wahrscheinlichkeitsrechnung” *Mathematische Zeitschrift* vol. 15 no. 1 pp. 211–225 1922. [Online]. Available: http://dx.doi.org/10.1007/BF01494395

[97] M. Hazewinkel *Encyclopaedia of mathematics.* Springer Science, 1990.

[98] D. Williams and V. Madisetti “Digital signal processing Handbook” 1997. [Online]. Available: http://dl.acm.org/citation.cfm?id=550591

[99] A. Garcia *Probability, Statistics, and Random Processes for Electrical Engineering* 2008.

[100] C. Therrien and M. Tummala *Probability and Random Processes for Electrical and Computer Engineers, Second Edition.* CRC Press, 2011.

[101] H. Benaroya, M. H. Seon, and M. Nagurka *Probability Models in Engineering and Science* 2005.

[102] O. Renaud and M. P. Victoria-Feser "A robust coefficient of determination for regression" *Journal of Statistical Planning and Inference* vol. 140 no. 7 pp. 1852–1862 2010.

[103] T. Katayama and S. Sugimoto *Statistical Methods in Control Signal Processing.* CRC Press, 1997.

[104] H. Holma and A. Toskala *LTE for UMTS - OFDMA and SC-FDMA Based Radio Access.* John Wiley Sons, 2009.

[105] M. Zuniga and B. Krishnamachari "Analyzing the transitional region in low power wireless links" *2004 First Annual IEEE Communications Society Conference on Sensor and Ad Hoc Communications and Networks, 2004. IEEE SECON 2004.* vol. 00 no. c pp. 517–526 2004.

[106] Anritsu "LTE Resources Guide" Tech. Rep. 2014.

[107] M. Loève "Fundamental limit theorems of probability theory" *The Annals of Mathematical Statistics* vol. 21 no. 3 pp. 321–338 1950.

[108] T. Specification "LTE; Evolved Universal Terrestrial Radio Access (E-UTRA); Base Station (BS) conformance testing (3GPP TS 36.141 version 10.1.0 Release 10)" Tech. Rep. 2011.

[109] J. V. Candy *Bayesian signal processing : classical, modern, and particle filtering methods.* John Wiley Sons, 2016. [Online]. Available: https://books.google.pt/books?id=dQp5DAAAQBAJ&pg=PA27&dq=maximum+likelihood+estimation+expectation+maximization&hl=pt-PT&sa=X&redir_esc=y#v=onepage&q=maximumlikelihoodestimationexpectationmaximization&f=false

[110] H. Kobayashi, B. L. B. L.-b. Mark, and W. Turin *Probability, random processes, and statistical analysis.* Cambridge University Press, 2012. [Online]. Available: http://www.cambridge.org/catalogue/catalogue.asp?isbn=9780521895446

[111] T. Hastie, J. Friedman, and R. Tibshirani "The Elements of Statistical Learning: Data Mining , Inference and Prediction" *Neural Networks* 2009.

[112] H. Ochiai and H. Imai "On The Distribution of The Peak-to-Average Power Ratio in OFDM Signals" *Communications, IEEE Transactions on* vol. 49 no. 2 pp. 282–289 2001.

[113] D. Ketchen Jr. and C. Shook "The application of cluster analysis in strategic management research: An analysis and critique" *Strategic Management Journal* vol. 17 no. 6 pp. 441–458 1996.

[114] R. Lehmann "Transformation model selection by multiple hypotheses testing" *Journal of Geodesy* vol. 88 no. 12 pp. 1117–1130 2014.

[115] R. Ibrahim, D. Voyer, A. Bréard, J. Huillery, C. Vollaire, B. Allard, S. Member, and Y. Zaatar "Experiments of Time-Reversed Pulse Waves for Wireless Power Transmission in an Indoor Environment" *IEEE Transactions on Microwave Theory and Techniques* vol. 64 no. 7 pp. 2159–2170 2016.

[116] M. M. Hyder and K. Mahata "Direction-of-arrival Estimation Using a Mixed L2,0 Norm Approximation" *IEEE Transactions on Signal Processing* vol. 58 no. 9 pp. 4646–4655 2010.

[117] G. E. P. Box, J. S. Hunter, and W. G. Hunter *Statistics for Experimenters: Design, Innovation, and Discovery.* John Wiley Sons, 2009.

[118] G. Lee and C. Scott "EM algorithms for multivariate Gaussian mixture models with truncated and censored data" *Computational Statistics and Data Analysis* vol. 56 no. 9 pp. 2816–2829 2012.

[119] Ettus Research "USRP B-210" 2015. [Online]. Available: http://www.ettus.com/product/details/UB210-KIT

[120] D. Sheet "AD9361 - RF Agile Transceiver" 2013. [Online]. Available: http://www.analog.com/en/products/rf-microwave/integrated-transceivers-transmitters-receivers/wideband-transceivers-ic/ad9361.html

[121] IEEE *IEEE Standard for Information technology–Telecommunications and information exchange between systems Local and metropolitan area networks–Specific requirements Part 11: Wireless LAN Medium Access Control (MAC) and Physical Layer (PHY) Specifications* 2012 vol. 2012 no. March. [Online]. Available: http://ieeexplore.ieee.org/servlet/opac?punumber=6178209

[122] Rohde Schwarz "RS SMU200A Vector Signal Generator - Overview." [Online]. Available: https://www.rohde-schwarz.com/vn/product/smu200a

[123] 3GPP "Overview of 3GPP Release 7" 2007. [Online]. Available: www.3gpp.org/specifications/releases/73-release-7

[124] K. Werner, H. Asplund, B. Halvarsson, N. Jaldén, D. V. P. Figueiredo, and A. K. Kathrein "LTE-A Field Measurements : 8 x 8 MIMO and Carrier Aggregation" *Vehicular Technology Conference (VTC Spring), 2013 IEEE 77th* 2013.

[125] M. S. Gast *802.11ac: A Survival Guide.* O'Reilly Media, 2013.

[126] E. Tsakalaki, O. Alrabadi, C. Papadias, and R. Prasad "Spatial spectrum sensing for wireless handheld terminals: Design challenges and novel solutions based on tunable parasitic antennas" *IEEE Wireless Communications* vol. 17 no. 4 pp. 33–40 2010.

[127] G. Vinci, F. Barbon, B. Laemmle, R. Weigel, and A. Koelpin "Wide-Range , Dual Six-Port based Direction-Of-Arrival Detector" *7th German Microwave Conference (GeMiC)* pp. 1–4 2012.

[128] A. Abdi, H. Hashemi, and S. Nader-Esfahani "On the PDF of the sum of random vectors" *IEEE Transactions on Communications* vol. 48 no. 1 pp. 7–12 2000.

[129] D. J. C. MacKay *Information Theory, Inference and Learning Algorithms.* Cambridge University Press, 2003.

[130] Karmeshu *Entropy Measure, Maximum Entropy Principle and Emerging Applications.* Springer, 2003.

[131] Veerarajan *Probability, Statistics, and Random Processes.* Tata McGraw-Hill Education, 2008.

[132] H. Scheffé *The Analysis of Variance.* John Wiley Sons, 1999.

[133] A. Mertins *Signal Analysis: Wavelets, Filter Banks, Time-Frequency Transforms and Applications.* John Wiley Sons, 1999.

[134] K. Prabhu *Window Functions and Their Applications in Signal Processing.* CRC Press, 2013.

[135] Mini-Circuits "ZN2PD-9G-S+." [Online]. Available: https://www.minicircuits.com/WebStore/dashboard.html?model=ZN2PD-9G-S+

[136] Keysight "N5242A PNA-X Microwave Network Analyzer, 26.5 GHz." [Online]. Available: http://www.keysight.com/en/pdx-x202277-pn-N5242A

[137] Xilinx "LogiCORE IP FIR Compiler v7.1" Tech. Rep. 2014. [Online]. Available: http://www.xilinx.com/support/documentation/ip_documentation/fir_compiler/v7_1/pg149-fir-compiler.pdf

[138] —— "Model-Based DSP Design using System Generator" Tech. Rep. 2014. [Online]. Available: https://www.xilinx.com/support/documentation/sw_manuals/xilinx2014_4/ug948-vivado-sysgen-tutorial.pdf

[139] S. Hauck and A. DeHon *Reconfigurable Computing: The Theory and Practice of FPGA-Based Computation.* Morgan Kaufmann, 2008. [Online]. Available: https://books.google.pt/books?id=dYKmZy0asrsC&pg=PA196&dq=mcode+xilinx&hl=pt-PT&sa=X&redir_esc=y#v=onepage&q=mcodexilinx&f=false